Physical Combinatorial Deposition and Characterization Methods for Advanced Electrochromic Metal Oxides

A Ph.D. Dissertation submitted in fulfillment of the requirements for the degree of Doctor of Physics and Materials Science

By

NOOR TAHA ISMAEEL

M.Sc. in Physics

Supervisor

Dr. Zoltán Lábadi

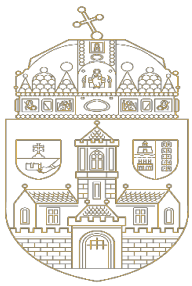

ÓBUDAI EGYETEM
ÓBUDA UNIVERSITY

Óbuda University, Doctoral School of Materials Sciences and Physics Technologies

Photonic department

Budapest, Hungary

2025

Abstract

Energy saving systems have been considered one of the most important components for today's economy. One of their applications is the electrochromic materials system or electrochromic device applied in many field: architectural glazing, high-contrast displays, sunglasses and smart windows, mirrors and automobile sunroofs etc. Electrochromic films have been used as components of smart windows to reduce the extra heat absorption through glass windows. This work focuses on the electrochromic behavior of mixed metal oxide layers deposited by reactive DC magnetron sputtering. Transition metal oxides such as Titanium oxide (TiO_2), Tin oxide (SnO_2), Zinc oxide (ZnO) and Molybdenum Trioxide (MoO_3) have been used in this study as promising electrochromic materials for this purpose since a smart window contains solid electrolyte and electrochromic material layers (commonly metal oxide layers) sandwiched between transparent conductive layers.

Combinatorial sputtering method was applied to study the dependence of electrochromic parameters on the composition in binary oxide systems. Pure metal targets were placed separately from each other, and indium–tin-oxide (ITO)-covered glass samples and Si-probes on a glass holder were moved under the two separated targets (Zn and Sn) in the chamber in a cyclic pattern. By using this combinatorial process the full composition range (from 0 to 100%) was made available for characterization after one sputtering preparation cycle.

The optical parameters and compositions have been determined and mapped by using Spectroscopic Ellipsometry (SE),

Transmission electrochemical cell (1 M lithium perchlorate ($LiClO_4$)/propylene carbonate organic electrolyte), was used to determine Coloration Efficiency (CE). This parameter is the main characteristic value for evaluating electrochromic device performance (change in optical density per unit charge injected, measured in cm^2/C).

Scanning Electron Microscopy. Energy-Dispersive X-ray Spectroscopy (EDS) has been used as an independent method to check the SE results.

First material system: I determined the optimal composition of reactive magnetron-sputtered mixed layers of Titanium oxide and Tin oxide (TiO_2-SnO_2) for electrochromic purposes. Ti and Sn targets were put separately from each other in the sputtering chamber, and the Si-wafers on a glass substrate (30 × 30) cm were moved under the two separated targets (Ti and Sn) in a reactive Argon-Oxygen (Ar-O_2) gas mixture. Different optical models, such as the (Bruggeman

Effective Medium Approximation or the 2-Tauc–Lorentz multiple oscillator) optical models, were used to obtain the thickness and composition maps of the sample. The performance of diverse optical models has been compared. I show that in the case of molecular-level mixed layers, 2-Tauc–Lorentz multiple oscillator optical model is better than Bruggeman Effective Medium Approximation optical model. The electrochromic coloration efficiency (the change of light absorption due to unit electric charge) of mixed metal oxides (TiO_2-SnO_2) was mapped too.

Second material system, Titanium oxide and Molybdenum oxide (TiO_2-MoO_3) mixed graded layers were prepared in the same chamber described above. Since the Ti-rich side was at a much higher temperature during the deposition process, so the Ti-rich oxide is polycrystalline while the Mo-rich side remains amorphous or nanocrystalline. Two separate peaks in the CE were found in the system (one in the Ti rich, on in the Mo rich segment)

Third material system: I performed an electrochromic investigation to optimize the composition of reactive magnetron-sputtered mixed layers of zinc oxide and tin oxide (ZnO-SnO_2).. The Coloration Efficiency data evaluated from the electro-optical measurements plotted against the composition displayed a characteristic maximum at around 29% ZnO. The accuracy of our combinatorial approach was 5%, calculated based on the accuracy of sample positioning in the measuring cell and the spot size of the optical beam. The mixed metal oxides showed at least 3 times better EC properties than the pure oxides.

This work aims to understand and optimize the electrochromic behavior of mixed metal oxides thin films deposited by reactive sputtering and to assess the results of investigations of such materials showing enhanced electrochromic behavior compared to the pure materials. Few publications studied the possible advantages (higher coloration efficiency) of the mixtures of different metal oxides as electrochromic material. My work proves that the electrochromic effectiveness (the change of light absorption for the same electric charge) can be higher in mixed metal-oxide layers.

Acknowledgements

It gives me sincerely great pleasure and grateful to seize this opportunity to express my sincere gratitude and thankfulness to my supervisor, (***Prof. Dr. Zoltán Lábadi***, and the supportive professor for this work, ***Prof. Dr. Miklós Fried)*** for their inspiring, encouragement, motivation, support, tolerance, patience, enthusiasm and great sacrifices during my academic research journey. My experience was greatly influenced and enhanced by the approach, because of their valuable scientific advice. I will forever be grateful for the value that ***Prof. Dr. Zoltán Lábadi*** and ***Prof. Dr. Miklós Fried*** have added to my learning experience and for the professional competence of my supervisors.

I would also like to thank the Director of the PhD School, ***Prof. Dr. Judit Borsa***, and ***Prof. Dr. Réger Mihály*** who provided me with useful tips, advice, motivation and support during my PhD process. I would also like to thank all the professors who giving me the valuable scientific courses: ***Prof. Dr. {Judit Telegdi***, ***Katalin Balázsi***, ***Peter Petrik***, ***Horváth Zsolt József***, ***Erzsébet Takács***, ***Péter Pinke***, ***Csaba Balázsi***, ***Tünde Kovács*** and ***George Kaptay}*** for their valuable experience and calendar my scientific path by many various tasks, exams and experiments related to my work, they made an extension of my professional knowledge during my doctoral training. My thanks to ***Hersics Katalin***, and all the Óbuda University staff. I want to acknowledge the Tempuse Public Foundation of Stipendium Hungaricum scholarship for their support, care and for giving me this wonderful opportunity. I want to thank and acknowledge all the staff of University of Baghdad, Iraq, and all the staff of Institute of Laser for Postgraduate Studies, especially the heads of Institute for their helpful, caring and for giving me the permission to study in Hungary. This work has been funded by NKFIH OTKA K 143216 and 146181 projects. Project TKP2021-EGA-04 acknowledges the support from the Ministry of Innovation and Technology of Hungary financed under the TKP2021 funding scheme. The work with 20FUN02 “POLight” project has received funding from the EMPIR program, co-financed by the Participating States and from the European Union’s Horizon 2020 research and innovation program. I would like to express my profound gratitude to my precious family: my lovely, beautiful Mother for her endless constant encouragement and great endless sacrifices have made this work successful, and my lovely sister and brothers, for their support, good wishes, endless encouragement, and the many sacrifices they have made over the years to bring me to where I am now.

Contents

Abstract II
Acknowledgements IV
1 Introduction 1
1.1 Subject and Aims of the dissertation 1
2 Literature survey 7
2.1 Introduction 7
2.2 Pure metal-oxides 7
2.3 Mixed oxides 9
2.4 Newest materials of interest in EC applications 24
2.5 Conclusions from the literature 26
3 Experimental Methods 28
3.1 Magnetron sputtering (combinatorial sample preparation) 28
3.2 Characterization methods 36
3.2.1 Spectroscopic Ellipsometry (SE) 36
3.2.2 Scanning Electron Microscopy (SEM) 40
3.2.3 Energy-Dispersive X-ray Spectroscopy (EDS) 42
3.2.4 X-ray Diffraction (XRD) 43
3.2.5 Functioning of SEM, EDS and XRD 44
4.1 Experimental Work 47
4.2 TiO_2-SnO_2 48
4.3 TiO_2-MoO_3 59
4.4 SnO_2-ZnO 63
5 Summary and Conclusions 75
6 Thesises and supporting publications 77
7 List of Publications 79
8 Future studies 81
9 Teaching activity during semesters 82
List of Figures 84
List of Tables 88
References 89

Abbreviations

Variable	Description
EC	Electrochromic, phenomenon related to color change caused by applied electric current
ECD, ECD_S	Electrochromic Device, devices changing their optical properties under DC bias
Ta_2O_5	Titanium-dioxide, a type of mixed metal oxides thin film
TCOE	Transparent Conducting Oxide Electrodes
TiO_2	Titanium-dioxide, a type of mixed metal oxides thin film
SnO_2	Tin oxide, a type of mixed metal oxides thin film
ZnO	Zinc oxide, a type of mixed metal oxides thin film
MoO_3	Molybdenum Trioxide, a type of mixed metal oxides thin film
SE	Spectroscopic Ellipsometry, an optical measurement technique used to characterize thin films and surfaces
SEM	Scanning Electron Microscopy, a microscopy technique that uses a focused beam of electrons to scan the surface of a sample
EDS	Energy-Dispersive X-ray Spectroscopy, an analytical technique used to determine the elemental composition of a material.
XRD	X-ray Diffraction, a non-destructive analytical technique used to determine the crystal structure, crystallite size, and other structural properties of materials.
Ar-O_2	Argon-Oxygen gas mixture
BEMA	Bruggeman Effective Medium Approximation optical model
2T–L, T–L	Tauc–Lorentz multiple oscillator optical model
CE	Coloration Efficiency η, change in optical density per unit charge injected
ITO	Indium–Tin-Oxide-covered glass samples
$LiClO_4$	Lithium Perchlorate (propylene carbonate electrolyte), high conductivity electrolyte solution commonly used in lithium-ion batteries
DC	Direct electric Current
UV	Ultraviolet radiation, a type of electromagnetic radiation with wavelengths shorter than visible light, but longer than X-rays.
CrO	Chromium Oxide, a type of mixed metal oxides thin film
Nb_2O_5	Niobium Pentoxide, a type of mixed metal oxides thin film
NiO	Nickel Oxide, a type of mixed metal oxides thin film
IrO_2	Iridium Oxide, a type of mixed metal oxides thin film
WO_3	Tungsten Trioxide, a type of mixed metal oxides thin film
MnO_2	Manganese Dioxide, a type of mixed metal oxides thin film

Co_3O_4	Cobalt Oxide, a type of mixed metal oxides thin film
V_2O_5	Vanadium Oxide, a type of mixed metal oxides thin film
Al_2O_3	Aluminum Oxide, a type of mixed metal oxides thin film
NAO	Nano Aluminum Oxide, a type of mixed metal oxides thin film
PMMA	Polymethyl Methacrylate thin film known as (acrylic)
FTO	Fluorine-doped Tin Oxide coating.
H^+	Positive Hydrogen ion, a hydrogen atom that has lost its single electron, leaving behind only the positively charged proton
Na_2WO_4	Sodium Tungstate dissolving salt
$C_{10}H_{14}O_5Ti$	Titanium (IV) oxide acetylacetonate, or Bis(acetylacetonate) titanium oxide
pH	measure of how acidic/basic water is
CC	Ciclic voltametry, Chronocoulometry detection methods technique
CV	Cyclic voltammetry, Voltammetry detection methods technique
CA	Chronoamperometry detection methods technique
ONT	Oxide nanotube, type of nanomaterial
ECs	Electrochromic materials, type of materials related to Electrochromic phenomenon
Li^+	Positive Lithium-ion battery
α-WO_3	tungsten oxide (amorphous)
Nd	Neodymium chemical element
Mo	Molybdenum chemical element
ATO NPs	Antimony-doped Tin Oxide nanoparticle
NIR	Near Infra-Red region
EIS	Electrochemical Impedance Spectroscopy detection methods
Li-PC	Lithium perchlorate in Propylene Carbonate, high conductivity electrolyte solution commonly used in lithium-ion batteries
AgNW	Flexible silver Nanowires, ultra-thin, elongated structures of silver that are known for their excellent electrical conductivity, optical transparency, and flexibility
PVD	Physical Vapor Deposition, a vacuum-based thin-film deposition technique where a solid material is vaporized and subsequently deposited onto a substrate to form a thin film
PSPT	Pulsed Spray Pyrolysis Technique, a method for synthesizing materials, particularly thin films and powders, by spraying a precursor solution onto a heated substrate or into a furnace
$V_{0.50}Ti_{0.50}O_x$	Vanadium-Titanium Oxide, a type of mixed metal oxides thin film
LiTFSI	Lithium bis (Trifluoromethanesulfonic) imide, Lithium salt
ZAO	Al doped Zinc oxide, a type of mixed metal oxides thin film

PTA	Peroxo tungstic Acid, a chemical compound formed by the reaction of tungsten trioxide with hydrogen peroxide
RFMS	Radio Frequency Magnetron Sputtering, a thin-film deposition technique that utilizes plasma and a magnetic field to eject material from a target and deposit it onto a substrate
CIGS	Copper Indium Gallium diSelenide, a semiconductor material primarily used in thin-film solar cells
OM	Optical Modulation, the process of altering the characteristics of light, such as its amplitude, phase, or polarization, to encode information
TEM	Transmission Electron Microscopy, a microscopy technique that uses a beam of electrons to create images of a sample, allowing for the observation of internal structures at the nanoscale
MOFs	Metal–Organic Frameworks, a class of porous, crystalline materials
MSPs	Metallo-Supramolecular Polymers, a type of polymer where the building blocks are held together by non-covalent interactions
E_g	Band gap energy, the minimum energy required for an electron to jump from a valence band to a conduction band within a material
E	Photon energy, the energy carried by a single photon, which is a quantum of electromagnetic radiation
MSE	Mean Squared Error, a common metric used to evaluate the performance of an optical models
SMU	Source Measurement Unit, a test instrument versatile tool used in semiconductor characterization
Fe_3O_4	Iron (II, III) oxide, Magnetite or Magnetic oxide, a type of mixed metal oxides thin film

Nomenclature

Symbol	Definition
H	Coloration Efficiency: the change of light transmission for the same electric charge.
ΔOD	Optical Density changes at a certain wavelength
Q_d	Charge density inserted into or extracted from the electrochromic material
Q	Charge
T_b	The transmittance of the bleached state
T_c	The transmittance of the colored state
cm^2/C	Square centimeter per Coulomb, the unit of CE
Λ	Wavelength
Nm	Nanometer
Å	Angstrom Å
%	Symbol used to indicate a percentage, a number or ratio as a fraction of 100
~	Approximately
cm^2/s	Square centimeter per Second, the unit of diffusion coefficient
W/m^2	Watt per square meter, the unit of density of heat flow rate
°C	Temperature unit in Celsius
Mm	Micrometer
V/V	Volume/Volume and is used when you mix 2 liquids together, unit in cubic meter (m^3)
ΔT	Optical modulation, the unit is %
V	Potential, unit in volt
wt%	Weight percent
mC/cm^2	Milli coulomb per square centimeter, the unit of charge capacities

Mol KCl	Molar Potassium Chloride solution
Sccm	System Center Configuration Manager, Microsoft Endpoint Configuration Manager
mF/cm^2	Milli Farad per square centimeter, the unit of surface capacitance
Mbar	Milli bar, the unit of vacuum
Ωcm	Ohm-centimeter, the unit of conductance, is the reciprocal of the Ohm, the unit of resistance
cm/s	Centimeter per second, the unit of speed
kW	Kilowatt, the unit of power
Ɛ	Effective complex dielectric function
Fi	Volume fraction
Ɛi	Complex dielectric function
I	Imaginary unit
K	Extinction coefficient
N	Complex refractive index
N	Real part of N
U, A, B, C	Fitted parameters
mV/sec	Millivolt per second, the unit of Cyclic Voltammetry scanning rates
F	Lorentz force
B	Magnetic field
v_x	Velocity
M	Mass
Φ	Psi is the Amplitude
Δ	Delta is the phase difference

r_p	Reflection coefficient for p polarization
r_s	Reflection coefficient for s polarization

1 Introduction

1.1 Subject and Aims of the dissertation

Building energy consumption produces expensive bills, and extra heat absorbed in buildings is found to be one of the major problems in our modern era. Improving the thermal and optical properties of smart windows can reduce a building's energy deficiency by up to 40% [1]. Because the air conditioning, heating, and ventilation in buildings account for 30–40% of the world's energy consumption, therefore, it is important to develop technologies that dynamically control the transparency of windows to reduce energy consumption in buildings. One of the possible solution is the application of electrochromic (EC) devices which exhibit repeated coloration/bleaching cycles of the so called smart windows. The color change is driven by back-and-forth charge transfer due to small DC voltages. Electrochromic film is one of the layers in an EC device which was placed on each side of a liquid (or solid) electrolyte layer. The EC layers have been presented as thin films of amorphous or crystalline oxides deposited on transparent conducting oxide electrodes (TCOE) coated glass. [2]. Under applied DC bias, transition metal oxides can change their color. This reversible color change is known as electrochromism. Potential applications for electrochromic windows include use in sensors, displays, and automotive rear-view mirrors and solar cells. The solid-state electro-chromic device consists of electrochromic metal oxides; charge storage Tantalum oxide (Ta_2O_5) layers and electrolyte layers sandwiched between TCOE. Electrochromic features like coloration efficiency (CE), cyclic durability and kinetics of coloration cycles of metal oxide strongly depend on the structure, morphology, and composition of the EC layer and therefore on the deposition methods and growth parameters.

Electrochromic phenomena are defined as color change caused by applied electric current. Electrochromic windows are among the favorable solutions to this problem, as they change their light-transmitting properties when exposed to DC bias [3-5]. Even in commercial constructions, controlling sunlight transmission can reduce 20-50% of lighting and energy expenses [2,6,7]. The active components of such electrochromic window technologies are metal oxide layers or organic films [3, 8-11] that exhibit electrochromism, a phenomenon where a material changes its optical properties upon charge injection or extraction. There are many types of such as Titanium Dioxide (TiO_2), Chromium Oxide (CrO), Niobium Pentoxide (Nb_2O_5), Tin Oxide (SnO_2), Nickel Oxide (NiO), Iridium Oxide (IrO_2), Zinc oxide (ZnO), Tungsten Trioxide (WO_3), Molybdenum Trioxide

(MoO_3), and Vanadium Oxide (V_2O_5) [12-19]. The color change caused by applied direct electric current bias (DC) is the definition of electrochromic phenomena, see equation (1) below.

The energy-saving windows (smart window), energy storage systems: such as electro-chromic (EC), photochromic and thermochromic have been designed on the same mechanism and both have layered device structures, and it was based on the electrochemical reaction of the electrode materials.

Electrochromic materials have several key parameters that significantly influence their performance and suitability for different applications. The most important ones:

-Coloration Efficiency, which measures the amount of optical change per unit of charge injected into the material. Higher coloration efficiency indicates more efficient use of energy and can lead to lower power consumption in devices.

-Optical Modulation, which refers to the change in optical properties (transmittance, reflectance, absorbance) when the material undergoes a redox reaction. High optical modulation is crucial for achieving significant color changes and achieving desired functionalities like dimming windows or creating displays.

-Response Time, which is the speed at which the material changes color in response to an applied voltage. Faster response times are generally desirable for applications like dynamic displays or rapidly adjusting window tints.

-Cycling Stability, which refers to the ability of the material to maintain its electrochromic properties over repeated cycles of coloration and bleaching. Long-term stability is essential for practical applications to ensure durability and longevity.

-Durability, which encompasses various factors, including resistance to degradation from environmental factors like moisture, temperature, and UV radiation. Durable materials are necessary for long-lasting performance in real-world applications.

-Color Range is the range of colors that the material can achieve and is important for aesthetic and functional considerations. Materials that can achieve a wide range of colors offer greater versatility in applications.

-Transparency in the Bleached State is crucial for applications like smart windows. High transparency is needed in the bleached state to allow maximum light transmission when not in use.

-Operating Voltage is the voltage required to induce color changes. It should be low to minimize power consumption and ensure compatibility with various power sources.

These parameters are interconnected and often influence each other. For example, optimizing fast response times may sometimes come at the expense of cycling stability. Researchers and engineers

must carefully consider these parameters and their tradeoffs when developing and selecting electrochromic materials for specific applications. These parameters depend on the structural, compositional characteristics and morphological, even growth parameters and deposition techniques. Overall performance of an electrochromic device is determined by four major physical characteristics: coloration efficiency (CE), optical contrast, switching time and cycling stability. A high-performance ECDs must have high CE, high contrast, fast switching time, long cyclic stability, and high efficiency to meet the market requirements.

Out of these four requirements the CE is a key parameter in determining the performance of electrochromic devices and the electrochromic process is based on a reversible redox process and characterized by the coloration efficiency (CE). This indicator shows the change in optical absorption per unit charge. It is usually expressed as the change in optical density per unit of charge passed per unit area (cm^2/C). High coloration efficiency means that a relatively small, injected charge can initiate significant color change, directly impacting energy efficiency.

Contrast ratio is defined as the ratio of the visible light transmission in the bleached vs. in the colored state. Higher contrast ratio means more visible change from the darkest to the lightest state, which is especially important for Electrochromic Devices (ECDs).

The switching time of an Electrochromic Device (ECD) refers to the time needed for the device to achieve 90% of its maximum optical change, when transformed from a bleached (transparent) state to a colored state or vice versa. This parameter is also known as the response time or - alternatively - as coloring / bleaching time. Typically, EC materials or devices that exhibit faster response times are preferred. Short response times mean rapid color change, which is critical for devices that require rapid change.

Cyclic stability refers to the ability of a material to maintain its properties through prolonged coloring and bleaching cycles. Lifetime is given by the number of coloring and bleaching cycles a material undergoes before it degrades to a predetermined level. High durability and long life are essential for commercial applications to ensure long-term reliability and cost-effectiveness of products.

The stability of commercialized (ECDs) can vary depending on the materials used and the environmental conditions that they are exposed. Another important parameter is Cycling Stability if CE is maximized. The ability of an ECD to maintain performance over many cycles of switching between states is important. Advancements in materials and encapsulation techniques are improving

the stability of ECDs, making them more viable for long-term applications in smart windows, displays, and wearable technology.

The most important parameter for EC films is the coloration efficiency (CE) which advertises to the Optical Density changes (ΔOD) at a certain wavelength induced when a unit area is injected with charge (Q_d). The CE is calculated using the following equation, and ΔOD is equal with the change of transmittance according to the Beer–Lambert law:

$$\eta(\lambda) = \frac{\Delta OD(\lambda)}{q/A} = \frac{\ln(Tb/Tc)}{Qd} \quad (1)$$

where T_b is the transmittance of the bleached state, T_c is the transmittance of the colored state, and Q_d is the density of the charge inserted into or extracted from the electrochromic material. The unit of CE is cm^2/C, square centimeter per Coulomb). CE has been calculated by specific absorption wavelength (λ) and the transmittances (Tb and Tc) have been dependent on this wavelength. The coloring process evaluated the power requirements by CE, and it was clear about the electronic efficiency of the ECDs. The result of the CE was presented by a plot of optical change vs. charge density which fitted the linear part of the graph, or alternatively, the relative transmission vs. input charge curves were plotted and CE values can be determined from the fitted exponential curves, see Figure 1-1 [20]. Due to possible electron transitions between two sets of electrons, the EC effect can be more pronounced in mixed oxides. Despite this, only a small number of studies can be read about the possible optimization of the EC parameters in mixed oxide-type films. The EC properties of Titanium oxide (TiO_2) were extensively studied prepared by the different methods: spray pyrolysis [21, 22], anodization [23-25], chemical vapor deposition [26], various wet chemical techniques [27, 28], and sputtering [29, 30].

The most widely studied EC oxide is Tungsten oxide (WO_3), and films of this material have been prepared by several different methods. Examples for physical vapor deposition: spray pyrolysis [31] pulsed laser deposition [32, 33], sputtering [34, 35], and thermal evaporation [36-40].

Electrochromic Molybdenum Trioxide (MoO_3) shows similar behavior to W oxide, and widespread studies used films prepared by wet chemical techniques [41, 42], chemical vapor deposition [43] and evaporation [44, 45].

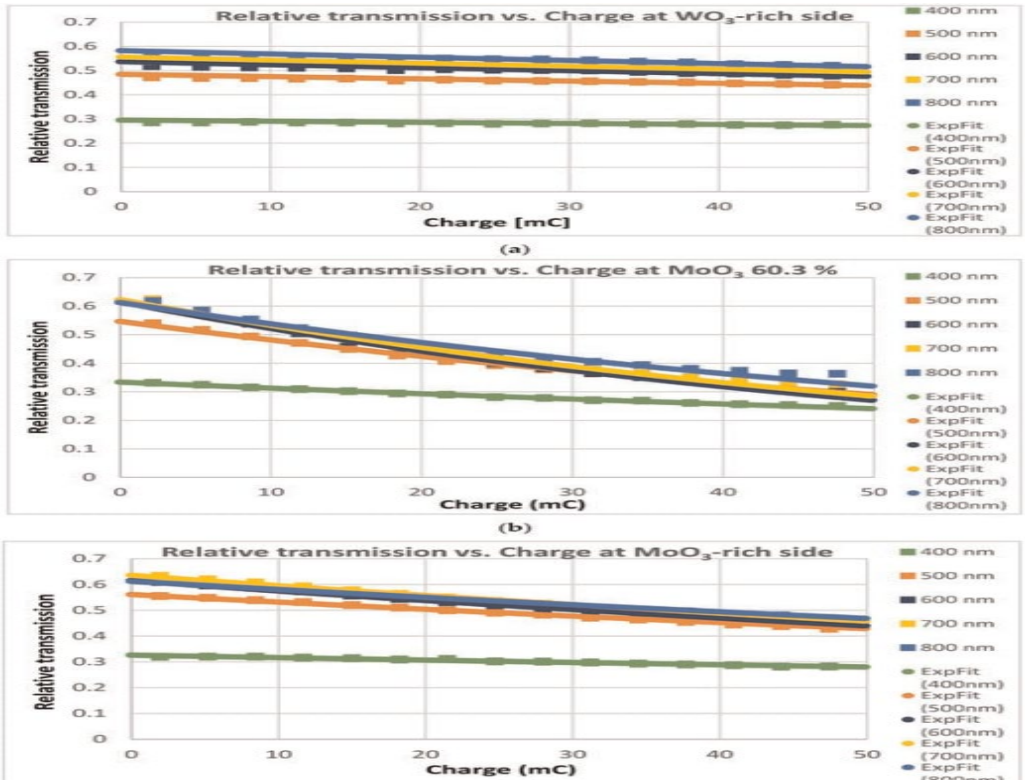

Figure 1-1: Relative transmission vs. input charge curves at five wavelengths for a pure WO_3 sample (a), for a WO_3-MO_3 (Mo-60.3%) mixed sample (b)and for a pure MoO_3 sample(c), CE values were determined from the fitted exponential curves [20].

Vanadium pentoxide-based thin films were also prepared for electrochromic purposes by spray pyrolysis [46], vacuum evaporation [47], inkjet printing [48], sputter deposition [49], electrodeposition [50, 51] and chemical techniques [52-55]. Nickel oxide films (NiO) were considered in hydrous nickel oxide form as EC material [56, 57].

The demand, supply factors, and the pricing depend on the accuracy of preparation methods for material mixes. (Physical deposition methods are promising for the market, because these preparation methods are highly accurate.) These combinatorial methods can help searching identify for more efficient advanced functional materials for different applications, such as micro-, nano-, and optoelectronics, energy converters (solar cells) or optical sensor systems, architectural glazing, high-contrast displays, sunroofs, sunglasses, and smart windows, etc.

Recently a variety of preparation methods of mixed metal oxides have been recognized to provide samples considered more economically and environmentally friendly. To examine the utilization of mixed metal oxides in different commercial products, effort has been put into determining cost-effective and scalable synthesis protocols. For example, reactive sputtering is well-known as a

scalable method; however, it can be relatively expensive to use big vacuum systems. However, it can produce highly accurate samples. To create larger size samples and lower expenses, different preparation methods can be used, such as sol-gel, sacrificing part of the accuracy. We must always consider safety standards when working with metal oxides and not exceed the risk limits of the excessive handling of such materials without adhering to safety conditions. Therefore, one should attempt to avoid toxic materials or excessively deal with carcinogenic oxidizing materials. Metal oxides, ubiquitous in industrial processes and consumer products, are known to leach into water bodies, posing a significant threat to aquatic ecosystems. Additionally, synthetic dyes, extensively used in various industries, can persist in water systems and exhibit complex chemical behavior.

According to the U.S. Department of Energy, replacing old single-paned windows with energy-efficient replacements should save energy 7% to 15% in energy costs, roughly $71 to $501 annually. So, it's worth the effort and the expected challenges in fitting with current window systems. Windows and doors can be made smart without replacing; they only need to fit them with smart sensors, locks or mechanisms that can be connected to your home network, usually via a smart hub. This allows them to be operated by an app on your smartphone or tablet. There are also windows and doors with integrated smart systems.

Earlier, we performed experiments with mixed metal-oxides and found a positive effect in electrochromic behavior [58-60]. Scarcely publications have been initiated and reviewed about the EC properties of (pure and mixed) metal oxides, [20, 58-62].

The present study is considered new since its objective was to investigate the electrochromic effectiveness of mixed metal oxide layers in a wide compositional range by determination of CE as a function of composition. This work aims to assess the results of investigations of such materials showing enhanced electrochromic behavior compared to the pure materials.

2 Literature survey

2.1 Introduction

This chapter focuses on estimating results of investigations and enhancement of electrochromic properties for mixed metal oxides contrast to the pure ones. The electrochromic process is based on a reversible redox process and characterized by coloration efficiency (CE).

Relatively few publications have studied the possible advantages (higher CE) of the mixtures of different metal oxides as electrochromic materials. The change in light absorption for the same electric charge represents the electrochromic effectiveness, and it can be higher in mixed metal oxide layers.

Historically, the first group of materials found to display electrochromic properties were metal oxides. Cathodic coloration EC oxides include WO_3, TiO_2, MoO_3, SnO_2, and Ta_2O_5, while anodic coloration occurs in NiO, CrO, MnO_2, Co_3O_4, and V_2O_5. These inorganic EC materials have high chemical and thermal stability, device durability, and cycling stability. However, these materials have inherent drawbacks as well, i.e., they provide slower response times, have mechanical rigidity, and most importantly their coloration is limited to a narrow spectral range. Rigidity limits their use in flexible devices and roll-to-roll technologies, while their spectral properties limit their application in color displays [12-19].

Today transition metal oxide films (Molybdenum and Tungsten) are considered the most popular and widely used and studied materials in this field. A solid-state electrochromic device consists of electrochromic (WO_3, MoO_3) electrolyte and charge charge storage layers sandwiched between transparent conducting electrodes (TCO).

2.2 Pure metal-oxides

The EC properties of the most widely studied for EC oxide (Titanium oxide (TiO_2), Tungsten oxide (WO_3), Molybdenum Trioxide (MoO_3) and Nickel oxide films (NiO)) have been studied widespread using different films preparation methods [21-57].

Ti oxide (TiO_2) has been investigated for its EC properties prepared by different methods such as: spray pyrolysis [21, 22], anodization [23-25], chemical vapor deposition [26] and sputtering [29]. CE of TiO_2 films that are deposited by reactive DC magnetron sputtering is approximately ~25 cm^2/C.

Tungsten oxide (WO_3) is considered the most widely studied EC oxide and films of this material have been prepared by several different methods. There are traditional thin film preparation methods that includes chemical methods (sol–gel deposition, spin coating, Langmuir–Blodgett technique, chemical bath deposition, etc.), electrochemical methods (anodization, plating), chemical and physical vapor deposition, see ref. [10] and references therein. Examples for physical vapor deposition: pulsed laser deposition [32, 33], thermal sputtering [34, 35] and evaporation [36-40].

Fabricating tungsten oxide films by chemical techniques have been described [63-65], most important is the chemical vapor deposition [66-68] and associated spray pyrolysis [69-73]. In most of the cases CEs of more than 60 cm^2/C have been found in the red wavelength region [10]. Electrodepositions [74-76] and anodic oxidation [77-79] have been described by other investigators. Various wet chemical techniques explained [27,28,80]

Electrochromic behavior of evaporated MoO_3 films have been compared to W oxide, and 34 cm2/C at 630 nm has been measured as CE [31, 44], while other methods such as electrodeposition [41], wet chemical techniques [42, 43] and chemical vapor deposition were also described [45].

Various chemical techniques have been verified that such films can exhibit the same values of CE as those of TiO_2 films [81] Nb oxide films has been prepared chemically and they presents electrochromism results [82-85] The CE of Ta oxide films was (10-15) cm^2/C and this results considered good worth for bleaching/coloration cycles, (79.8%) was the high reversibility and (2.35×10-8 cm^2/s) was the large ion-diffusion coefficient [86]. A technique as radio frequency reactive sputtering has been presented in [30]. Titanium oxide (TiO_2) has been prepared by thermionic vacuum arc method in [87].

Aluminum oxide (Al_2O_3) is used in coatings for surfaces to provide enhanced properties such as corrosion resistance, scratch resistance, and improved adhesion. In the electronics industry, Al nanoparticles are utilized in the fabrication of conductive inks and pastes for printed electronics [88]. The heat transfer has been studied practically to define the appropriate insulation conditions. Their study focuses on finding the amount of heat transfer through a glass substrate that is coated with Nano alumina doped on Polymethyl Methacrylate (PMMA) matrix, PMMA thin film is more popularly known as acrylic, it is a transparent and rigid thermoplastic, and it is produced from the monomer methyl methacrylate. PMMA shows high resistance to UV light and weathering. Due to its transparency, PMMA is used in car windows, smartphone screens and aquariums. The optical and thermal properties were systematically investigated. The density of heat flow rate was calculated in

the range values (240-260) W/m^2 while the optimum values confine between (250-260) W/m^2 at temperature (25-35) °C. The results showed that the thermal insulation of the sample was significantly enhanced at temperature (30-50) °C. The simulated net heat transfer through the window decreased linearly with an increase of both coating thickness concentration. Furthermore, the overall transmittance in the visible region and reflectance in infrared and ultraviolet regions decrease with increasing weight content of the coated film [88].

2.3 Mixed oxides

2.3.1 TiO_2-WO_3

In the nano-array films, notable enhancement of the EC properties has been investigated by Cai et al [89] and the result data of EC purposes of TiO_2 and WO_3 core/shell nanorod arrays have been considered as promising material because of the larger surface area for charge-transfer reactions was obtainable for ion diffusion. They are prepared by electrodeposition methods and a combination of hydrothermal. Sodium Tungstate (Na_2WO_4) dissolving salt in 12.5 mM concentration deionized water has been prepared. Sodium tungstate was mixed with hydrogen peroxide to the solution preserving a concentration ratio of 3. Fluorine-doped Tin Oxide coating (FTO) glass has been coated by a deposition electrode as TiO_2 nanorod array. The enhancement in EC properties has been achieved to the porous space surrounded by the nanorod arrays and the core/shell nanorod array's structure. Significant improvement such as: (2.4 s and 1.6 s) fast switching speed, high CE (67.5 cm^2 C^{-1} at 750 nm), magnificent cycling behavior (65.1% after 10,000 cycles) and wonderful consequences of optical modulation (38.4% at 10 µm, 70.3% at 1800 nm and 57.2% at 750 nm) have been dimensioned.

Spray pyrolysis technique has been investigated by Patil et al [90] at Deposited TiO_2-doped WO_3 thin films at 525 °C on Conducting glass substrates coated by (FTO). The first materials that were used for the deposition of TiO_2-doped WO_3 thin films, were ($C_{10}H_{14}O_5Ti$) titanyl acetylacetonate and (WO_3) Tungsten trioxide. At 80 °C, ammonium tungstate solution has been prepared by WO_3 powder dissolving in liquid ammonia. The powder ($C_{10}H_{14}O_5Ti$) titanyl acetylacetonate has been separately dissolved at room temperature in methanol. To form a homogeneous 100 ml precursor solution at pH = 9, the two solutions have been mixed in contrary volume percentages. Dopant volume percentage of TiO_2 has been diverse between 13% to 38% v/v. Transparent, strongly sticky to the substrates and uniform was the specifications of thin film samples. Pour domination could not be

formed (for percentage of TiO_2 greater than 38% doping in WO_3 homogeneous solution). With help of [chronocoulometry (CC), voltammetry (CV) and chronoamperometry (CA)] techniques and during the studied range for electrochemical properties of TiO_2-doped WO_3 thin films, the researchers have concluded that TiO_2 doping enhances the electrochromic performance of WO_3 and samples reveal a high reversibility increasingly with doping concentrations of TiO_2.

Low temperature preparation of WO_3/TiO_2 films has been investigated by Dhandayuthapani et al [91] by synthesizing (nebulized spray and chemical bath) deposition techniques. The WO_3 layer impacts on the (compositional, structural, electrochemical and morphological) characteristics of TiO_2 films. The current density of the TiO_2 films has been beneficially improved by deposition of WO_3 nanoplates on the TiO_2 layer. Figure 2-1 presented the results of electrochemical investigation of the annealed WO_3/TiO_2 films such as: 77.2% was the reversibility, 128.3 cm^2C^{-1} was the CE and 78% was (ΔT) the optical modulation. A fast response of 6 s for bleaching and coloration has been indicated with magnificent durability for 1000 cycles. The enhancement in EC behavior has been caused by facilitating faster charge transport, the interconnected nanoplate bundles which provide more charges and the complementarity of the WO_3–TiO_2 layers.

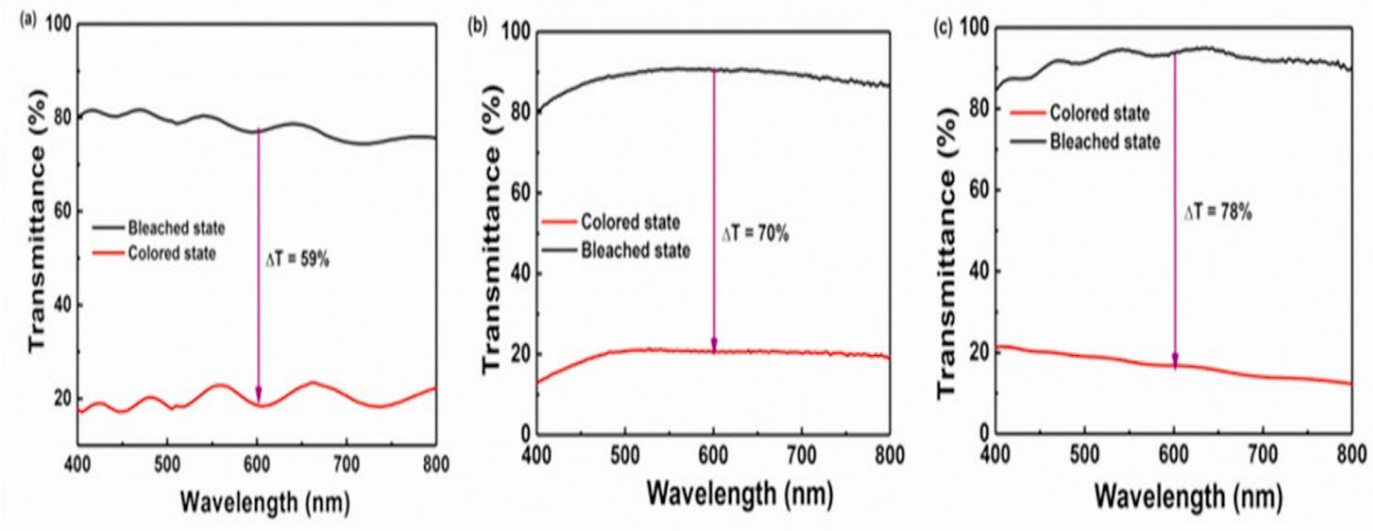

Figure 2-1: Bleached and colored transmittance spectra of (a) TiO_2, (b) (WO_3/TiO_2) deposited, (c) (WO_3/TiO_2) annealed films [91].

The assembly of (TiO_2) Titanium dioxide nanorods/(WO_3) Tungsten oxide hybrid thin films has been investigated by Ashok Reddy et al [92] and the impact of nanostructures on the electrochromic deportment of the films. By sputter deposition method, enhanced WO_3 films have been coated by TiO_2 nanorod film. Under diverse partial pressures of oxygen and at 400 C temperature, WO_3 thin

films have been deposited at fixed substrates. By hydrothermal process, Tungsten nanorods have been grown on glass substrate that is coated by (FTO). UV-Visible spectrometry, Raman, XPS, XRD and Cyclic voltammetry have been used for electro-chemical and material analysis of the films. Figure 2-2 presented the data results as: The TiO_2 nanorods/WO_3 hybrid films reveal impressive electrochemical characteristic that relatively of the diffusion coefficient of 1.8×10^{-7} cm^2/s surpass than those of pure (WO_3 and TiO_2) nanorods and the optimized coloration efficiency of the enhanced WO_3 films was assigned to its large active surface area which preferred H^+ ions insertion in the films.

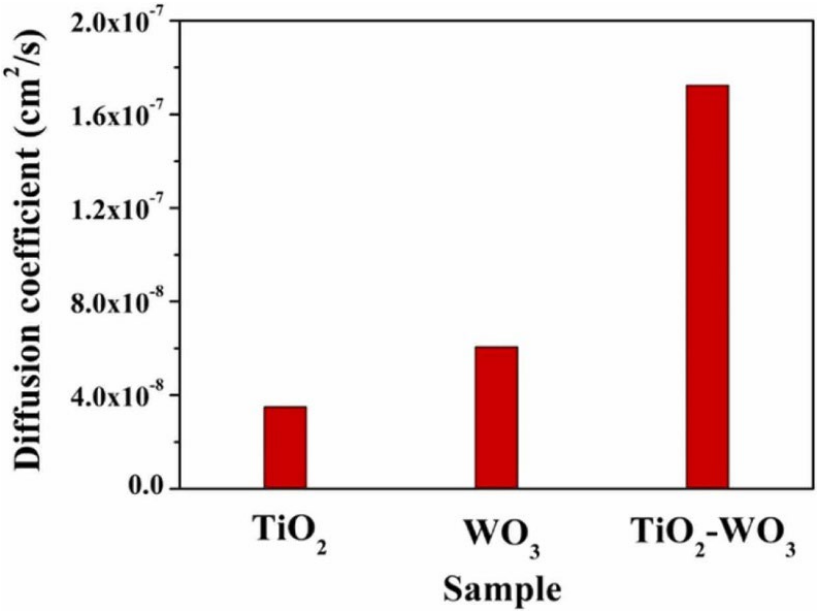

Figure 2-2: Diffusion coefficient contrast of[(TiO_2-WO_3) and (TiO_2, WO_3)] films [92].

Under special electrochemical conditions, regular and homogeneous arrays of TiO_2−WO_3 nanotubes have been investigated by Nah et al [93] and they concluded that it can be layered by anodization of Ti alloys in an ethylene glycol/fluoride-based electrolyte. By anodization at 120 V in a solution of ethylene glycol with 0.2 Mol HF, they sputtered nanotube films on diverse substrates [Ti-9 at% W (Ti-9W) and Ti, Ti-0.2 at% W (Ti-0.2W)]. The growing time has been controlled to perform a comparable thickness of the layers. A thickness of 85−95 nm and 1.1−1.2 μm tube diameter has been achieved of ordered oxide nanotube layers. The improvement of enhanced EC reactions and properties caused by small amounts of WO_3 (such as 0.2 at %) of these mixed oxide nanotube structures and (onset potential, contrast and cycling stability) of nanotube layer-based devices, as in Figure 2-3.

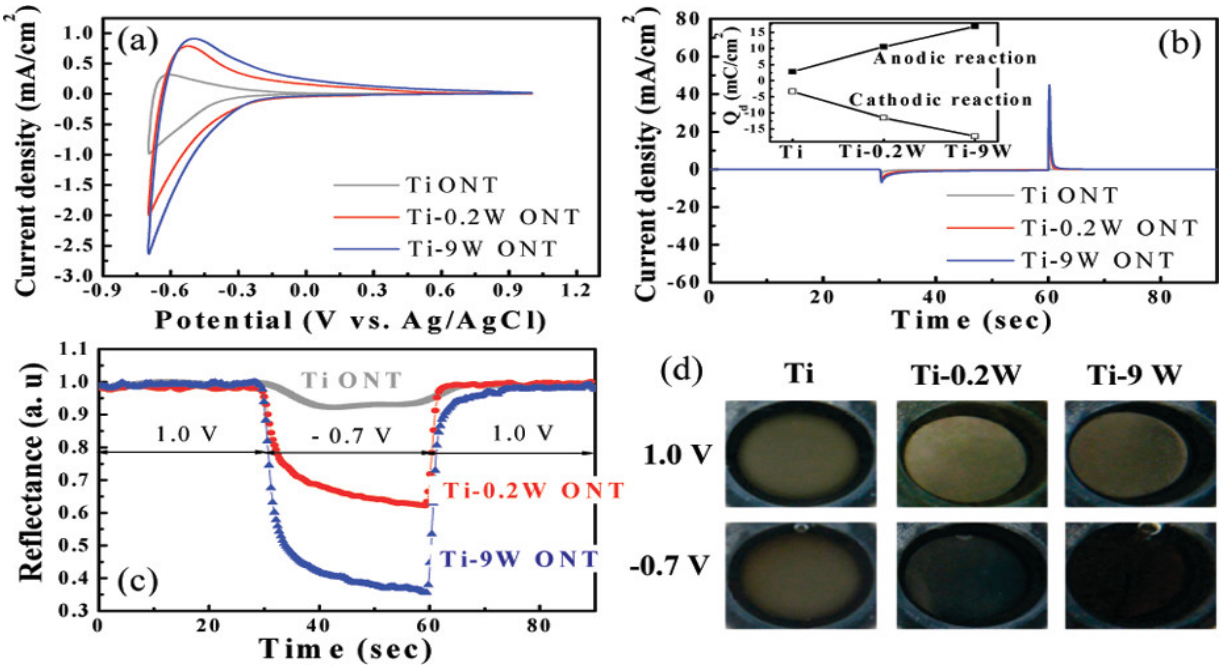

Figure 2-3 (a) Cyclic voltammograms of the oxide nanotube (ONT) layers on Ti, Ti-0.2W, and Ti-9W performed between −0.7 and 1.0 V with a scan rate of 50 mV in 0.1 Mol HClO4 electrolyte; (b) current density−time curves acquired by pulse potential measurement applied between −0.7 and 1.0 V with 30 s duration; (c) in situ reflectance curves of Ti, Ti-0.2W, and Ti-9W ONTs obtained during potential pulsing applied between 1.0 and −0.7 V; and (d) optical images of the electrochromic effect of the different nanotube surfaces during polarization cycling between 1 and −0.7 V. The inset of (b) shows integrated charge density (Qd) for the samples. Reprinted (adapted) with permission [93].

2.3.2 SnO_2–WO_3

Using a dip-coating method, Nd–Mo co-doped SnO_2/α-WO_3 electrochromic materials have been deposited by Goei et al [94]. The Nd–Mo co-doped SnO_2/α-WO_3 ECs reveal up to 90% visible light transparency at λ = 600 nm, estimating to the conventional SnO_2/α-WO_3 ECs and after up to 1000 volatile cyclic trial, 59% electrochromic functionality drop against undoped device after up to 1000 reversible cycle test. Moreover, these doped samples displayed shorter switching time (31% of the undoped) and high coloration efficiency (~200 cm^2/C). The authors claimed that these improved characteristics related to the adding of Nd–Mo co-dopants that restrict the trapping of Li^+ ion within α-WO_3 framework and decrease the extent of crystallization of α-WO_3 layer.

Kim et al [95] added Antimony-doped Tin Oxide nanoparticle (ATO NPs) to WO_3 EC films at three different concentrations: 0, 0.6, 1.2, 2.4 wt%. 1.2 wt% was found to be optimal where the WO_3 EC film with ATO NPs displayed better EC performance regarding both CE value (48.2 cm^2/C) and the switching times (2.4 s for the bleaching time and 5.4 s for the coloration time). The authors concluded

that the large band gap of ATO NPs widens the transmittance modulation band of the EC layer which helped to increase the CE value. A further component of the enhancement of EC performance was identified as the improved electrical conductivity caused by the evolution of preferable electron tracks due to the well-dispersed ATO NPs in the WO_3 film.

In a recent work Wei et al [96] showed an electrochromic window that had adequate characteristics, particularly in the NIR region. The electrochromic layer was set up of hierarchical amorphous WO_3/SnO_2 nanoflake arrays which were prepared by combining hydrothermal and ultraviolet photo deposition processes. The UV–vis-NIR transmittance spectra, the photothermal maps, and the electrochemical tests (CV, CA, and EIS) showed, that the hierarchical film displayed improved electrochromic characteristic including fast response time, proper cycling durability, high coloration efficiency. The hierarchical amorphous WO_3/SnO_2 nanoflake arrays also had adequate transmittance modulation in the NIR region. The NIR contrasts reached 65.7 % and 66.5 % at 1200 and 1600 nm. The visible contrast was 73.5 % at 633 nm, see Fig. 2-4.

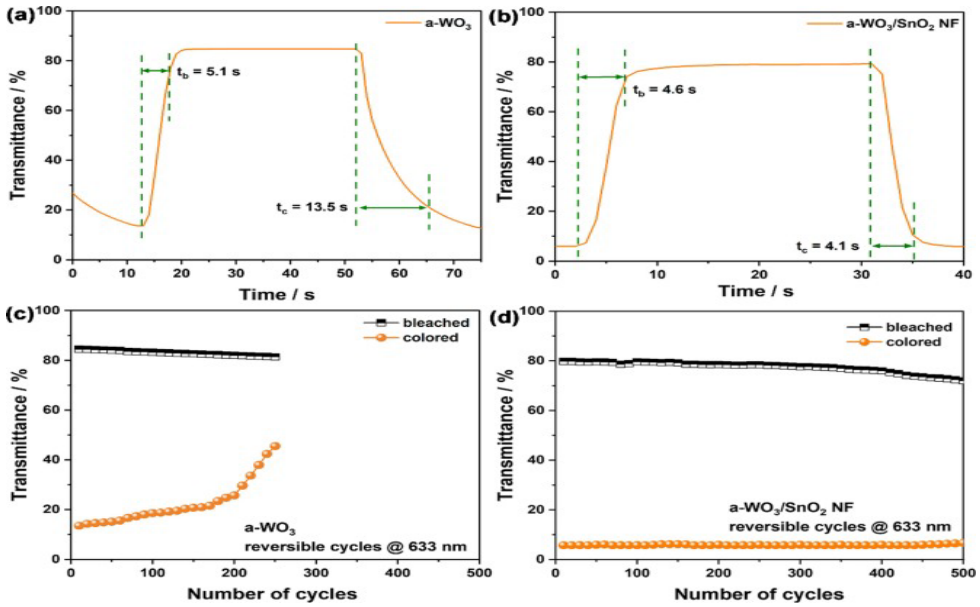

Figure 2-4 Transmittance variation curves at 633 nm when the a-WO_3 (a) and a-WO_3/SnO_2 NF (b) electrochromic windows were switched from bleached to colored state. Response times were indicated. Durability tests of the a-WO_3 (c) and a-WO_3/SnO_2 NF (d) elec-trochromic windows were cycled 500 times at 633 nm [96].

2.3.3 WO_3-NiO

S. V. Green [97] investigated the electrochromic Ni_xW_{1-x} oxide thin film structure, where $0 < x < 1$. Reactive DC magnetron co-sputtering was applied to deposit the thin layers from one Ni and one W metal target. Furthermore Ni oxide was deposited with applying added water vapor in the

sputtering gas. Structural characterization of all layers was accomplished by X-ray diffraction, *X*-ray photoelectron spectroscopy, Raman spectroscopy and Rutherford backscattering spectrometry. The nanostructures of different films were studied by ellipsometry using effective medium approximation. Electrochemical and optical properties have been characterized by cyclic voltammetry and spectrophotometry in 1 M lithium perchlorate in propylene carbonate (Li-PC).

High (over 85 %) Ni content samples were found to be polycrystalline while all other films were amorphous. W-rich samples (Ni content below 50 %) consisted of a blend of W oxide and $NiWO_4$ -phases, while the Ni-rich (over 50 %) samples were made of hydrated Ni oxide and $NiWO_4$ -phases. Samples with $0 < x < 0.3$ exhibited electrochromic properties matching W oxide, and films with $0.7 < x < 1$ functioned as Ni oxide. For $0.4 < x < 0.7$ no optical change was observed. The sample behaved as an optically inert intercalation material at the boundary of cathodic electrochromic and non-electrochromic characteristics, i.e., $x \sim 0.4$. Ni addition to W oxide enhanced the coloration efficiency. Spectral coloration efficiency curves are shown for selected composition W-Ni oxide films in Fig. 2-5 [98]. The transmittance change was 0.45 and 0.15 for the W-rich and Ni-rich samples, respectively.

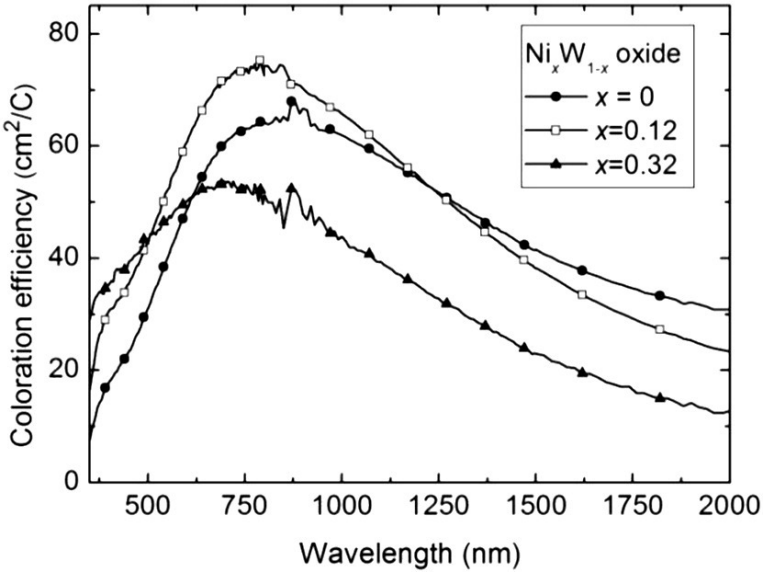

Figure 2-5 Spectral coloration efficiency for W–Ni oxide films with the compositions shown [98].

Rakibuddin et al [99] synthesized NiO by a cost effective sol−gel spin-coating process. The prepared NiO was used as an electrochromic anodic layer and deposited onto a transparent conductive electrode (indium tin oxide, ITO or flexible silver nanowires, AgNW) by a sol–gel spin coating and low temperature annealing. The deposition methods were optimized to achieve better

EC characteristics. NiO/ITO displays high transmittance variance (ΔT = ~84%) at 700 nm with applied potentials of −3.0 and 0 V. The stability and transmittance variance of NiO/ITO are significantly improved in the presence of a WO_3 cathodic electrode at lower applied voltages of 1.5 to 0 V, see Fig. 2-6. The flexible NiO–WO_3 device reaches a transmittance variation of ~38% at 700 nm with applied potential of 2.0 and 0 V respectively, and preserves the EC performance.

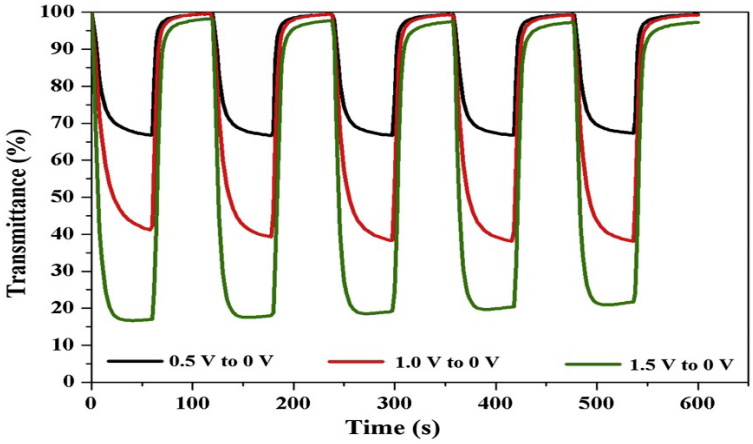

Figure 2-6 ECD performances of the NiO/WO_3 ECD (ITO) show stability at different voltages[99].

2.3.4 WO_3-Ag

Najafi-Ashtiani et al [100] used physical vapor deposition (PVD) to prepare tungsten oxide electrochromic thin films on fluorine doped tin oxide (FTO) coated glass substrates. In order to achieve changes in the surface morphology, they made the PVD preparation at an angle of 0° and of 75°. Combined with the PVD method powdered Ag nanoparticles were used to dope the surface of the WO_3 thin layers. The EC thin layers were annealed to diffuse the Ag nanoparticles into the layer. Indirect transitions have been reported in the band gap of WO_3–Ag thin films. By using cyclic voltammetry and visible transmittance data, EC characteristics of WO_3–Ag thin films were studied to evaluate the effect of surface morphology. Higher surface roughness and clear optical modulation (40.59% at 632.8 nm) and high Coloration Efficiency (90.2 cm^2/C at 632.8 nm) were detected for the second sample which was prepared at an angle of 75°. (See equation 1 and Table 2-1).

Sample	DC voltage steps (V)	T_c (%)	T_b (%)	ΔT (%)	CE ($cm^2\ C^{-1}$)	τ_C (s)	τ_B (s)	Γ(λ) ($cm^2\ C^{-1}\ s^{-1}$)
WAg_{-0}	+1.0 to −1.0	45.15	82.18	37.03	71.9	4.2	11	9.46
WAg_{-75}	+1.0 to −1.0	43.09	83.68	40.59	90.2	3.9	8.9	14.09

Table 2-1: Electrochromic properties of WAg-0 and WAg-75 thin film in 0.5 M solution $LiClO_4$-PC at 632.8 nm [100].

Recently, Park et al [101] reported the structural, optical, and electrochemical properties of Ag nanoparticle containing electrochromic WO_3 thin layers with varied concentrations. Room-temperature-sputtered thin films using composite targets with a low Ag concentration showed an irregular distribution of small nanoparticles, while with a higher Ag concentration, the particles were merged, leading to the formation of a single or polycrystalline phase. They measured surface plasmon resonance peaks in the absorption spectra of the Ag–WO_3 composite layers, indicating the development of metallic nanoparticles. The presence of these nanoparticles was also reaffirmed via high-resolution transmission electron microscopy. The $W_{0.91}Ag_{0.09}O_{3-\delta}$ thin layer had faster switching time with a higher coloration efficiency of 66.52 cm^2/C than those of the $WO_{3-\delta}$ thin layer, which were 58.68 cm^2/C. However, transmittance modulation in $W_{0.91}Ag_{0.09}O_{3-\delta}$ thin film was worse than in the other films, see Fig. 2-7. Furthermore, the $W_{0.91}Ag_{0.09}O_{3-\delta}$ thin films were black in the colored state, whereas the pure $WO_{3-\delta}$ and $W_{0.97}Ag_{0.03}O_{3-\delta}$ thin films were Prussian blue, suggesting the achievement of color neutrality through the incorporation of Ag nanoparticles.

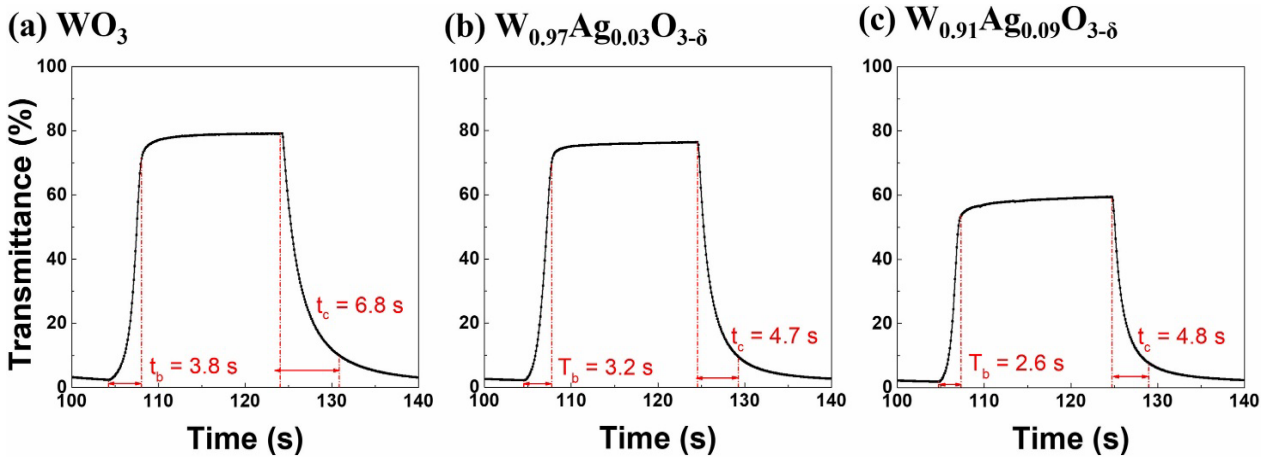

Figure 2-7 Transmittance switching response of (a) $WO_{3-\delta}$, (b) $W_{0.97}Ag_{0.03}O_{3-\delta}$, and (c) $W_{0.91}Ag_{0.09}O_{3-\delta}$ thin films grown at room temperature on ITO-coated glass substrates[101].

2.3.5 V_2O_5–WO_3

Patil et al [46] prepared V_2O_5-WO_3 mixed layers on FTO-coated glass substrates at 400 °C using a novel Pulsed Spray Pyrolysis Technique (PSPT). Aqueous solutions of equimolar vanadium chloride and ammonium tungstate were mixed in 3 different volume proportions (5%, 10% and 15%) for the preparation of V_2O_5–WO_3 thin layers. The optical, morphological, structural, and electrochemical properties of V_2O_5–WO_3 thin films were studied by cyclic voltammetry, XRD, FTIR, SEM, chronocoulometry and chronoamperometry measurements. Their results showed that the electrochemical properties of V_2O_5 were modified by mixing WO_3. All the films showed cathodic electrochromism in lithium containing electrolyte (0.5 M $LiClO_4$ + propylene carbonate (PC)). The electrochemical durability of the samples has been studied, and found to be stable up to 1000 cycles. Maximum coloration efficiency (CE) of about 49 cm^2/C was measured for the V_2O_5 film mixed with 15% WO_3.

Prasad et al [102] applied a one-step electrochemical co-deposition procedure, to deposit a W-V mixed metal oxide composite thin-film structure consisted of WO_3 and V_2O_5. The electrochemical energy storage and electrochromic parameters of the deposited thin films at different amounts of WO_3 and V_2O_5 have been investigated. In the films of the W-V mixed composite WO_3 and V_2O_5 oxides at the ratio of 1:1, electrochromic properties were measured, such as a fast coloration response of 4.9 s, an optimum optical contrast of 60%, and the highest coloration efficiency of 61.5 cm^2/C, see Fig. 2-8. Furthermore for the electrochemical energy storage application, a maximum unit surface capacitance of 38.75 mF/cm^2 at an applied current of 0.5 mA/cm^2 has been reached, and it displayed a capacitive retention of 78.5%, even after 5000 charge/discharge cycles. The enhanced characteristics of both electrochemical energy storage and electrochromic applications was associated with the (a) fast charge transfer kinetics, (b) unique morphology containing more active in both cases of WO_3 and V_2O_5, and (c) redox behavior of both metal ions present in the synthesized W-V mixed metal composite.

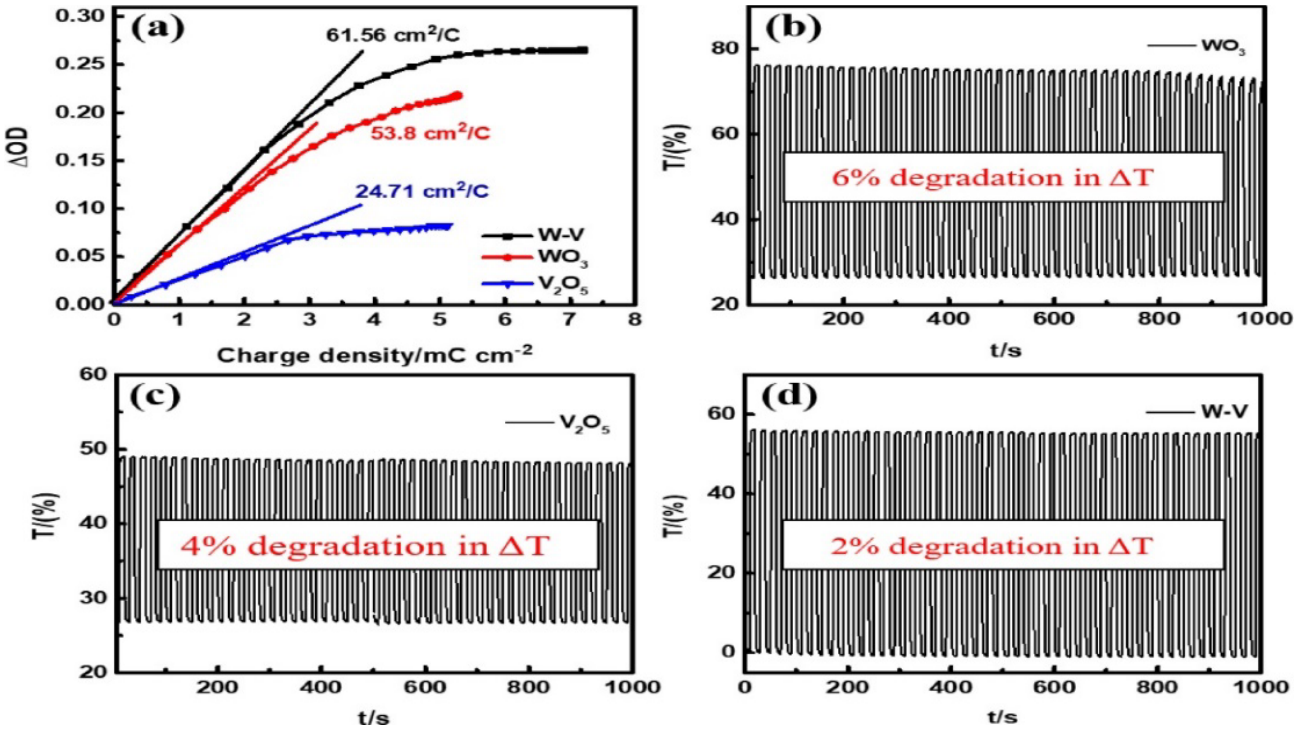

Figure 2-8 Variation of the change in optical density (ΔOD) vs. charge density for WO_3, V_2O_5, and W-V thin films (a), In situ optical responses of WO_3 (b), V_2O_5 (c), and W-V (d) between the colored (−1 V) and bleached (+1 V) states at 700 nm for 1000s, performed in 1.0 M $LiClO_4$/PC [102].

2.3.6 $V_{0.50}Ti_{0.50}O_x$

Burdis et al [103] applied RF sputtering from metallic targets for deposited thin layers of $V_{0.50}Ti_{0.50}O_x$. They used this film as a potential counter electrode in studying electrochromic device characteristics. They found that the film can reversibly store relatively large amounts of charge, and it is slightly yellow looking in transmission, whilst displaying a reasonably low electrochromic coloration efficiency. The possible electrochemical reactions of $V_{0.50}Ti_{0.50}O_x$ were found to be simple, in fact rather the same as that of WO_3, for those reasons they found that this material was considered almost equivalent for use in a variable transmission device. Charge capacities were measured to 60 mC/cm^2 for 300 nm film thickness. The authors planned to study further the electrochromic coloration of these films up to high levels of charge insertion, and to determine the effect of repeated cycles of charging and discharging on the lifetime of such structures.

Marcel et al [104] used the overlaying of two tungsten and vanadium-titanium oxide thin films to decrease the blue absorption of vanadium oxide prepared by roll-to-roll radiofrequency sputtering method. To produce flexible devices adaptable for eyewear purposes, an ITO-coated mylar substrate was used. Tungsten oxide was applied as working electrode, while the counter-electrodes examined

were vanadium-titanium oxide mixtures. The electrolyte used for both electrodes was a polymer gel lithium ionic conductor made of a LiTFSI lithium salt dissolved in PC and incorporated within a photopolymerized acrylate matrix. They studied the electrochromic properties to the counter-electrode at four different atomic ratios of titanium in the (0-100%) range increased at 25% steps. A blue shift effect in the transmittance spectra of as-deposited films was measured as the titanium amount was increased. In situ optical characteristics were investigated by cycling the potential in the range of 1.5-4V, and the sample with equal proportion of vanadium and titanium displayed a notable neutrality of coloration. Complete devices were prepared with different Ti/V ratios of 0, 1:3, 1:1 and 3:1 in the counter-electrode. The film thickness of tungsten oxide has been secured to 300 nm, while the thicknesses of vanadium-titanium oxide films have been set based on their respective electrochemical capacity. The electrochromic characteristics obtained together with their cycling durability and response times were evaluated to find the optimal vanadium-titanium composition.

2.3.7 WO_3–MoO_3

Only in a few cases have the properties of mixed tungsten and molybdenum oxides been studied, despite the fact that they are the most studied material for electrochromic devices. Prameela and coworkers [105] studied these mixtures, but only in a small number of compositions between 0-100 % in 20 % steps.

Chaichana et al. [16] prepared molybdenum/tungsten trioxide (MoO_3/WO_3) electrochromic films from a peroxotungsten acid (PTA) solution on indium-doped tin oxide (ITO) glass substrate by sol-gel and dip coating methods in compositions of 15, 30 and 50 %. The effect of MoO_3 ratios on electrochromatic, optical and microstructural properties of films was studied applying Cyclic Voltammogram (CV), Spectrophotomety, AFM, XPS, XRD, and SEM. The 30% MoO_3 doped WO_3 film showed the best diffusion coefficient, indicating the best electrochemical property. MoO_3/WO_3 composition of 30 % was found to have the largest color difference between bleached and colored states compared to other compositions (44 %). The maximum diffusion coefficient was approximately 3.4 x 10^{-11} cm^2/s.

Faughnan and Crandall [106] have concluded that electrochromic optical absorption of mixed MoO_3/WO_3 amorphous films occurs at shorter wavelengths than in the case of pure oxides. The dependence of wavelength shifts as a function of MoO_3 concentration and optical density was measured, however, only at x -5% MoO_3, -30% MoO_3, -75% MoO_3 compositions. They explained their data using the intervalence charge transfer model, according to which electrons are at 0.7 eV higher level in W6+ ions than electrons trapped at Mo^{6+} ions [107]. WO_3 films are not the best for

screens, as their peak absorption is about 885 nm, while our eyes are most sensitive at 550 nm. The maximum absorption peak of mixed oxides is at 575 nm. That is, less charge needs to be injected into a mixed oxide film to achieve a better contrast ratio, since its absorption peak is more in line with the reaction of the eye.

Hamelmann et al. [108] studied the electrochromic and other properties of pure and 50-50 % WO_3/MoO_3 layers made from sol-gel. Raman spectrometry studies showed that WO_3 and mixed films were generally amorphous, while the pure MoO_3 film proved crystallized. After annealing at 270 C, the films showed good electrochromic behavior. All the films fulfilled the requirements for electrochromic device applications since their Coloration Efficiencies ranged between 60-120 cm^2/C.

Arvizu et al. [109] studied the electrochromicity of mixed W-Mo oxides deposited by DC magnetron co-deposition. They used eight different compositions, ranging from 100-0 % to 70-30%. In particular, the cyclic durability and spectral properties of samples were studied. It has been observed that the injected charge is greater than the charge extracted in the first cycle. The observed effect was increasingly greater with higher Mo content. The change in the injected electric charge was attributed to trapped and accumulating Li ions and increasingly difficult intercalation. Every films acquired a characteristic yellowish color. In cyclic durability measurements, the peak of absorption shifted towards shorter wavelengths compared to pure WO_3, and the layers became greyish in the colored state. The authors found that mixed oxides are better for "smart windows" because they can give a more neutral dark state.

Labadi et al. [20] fabricated a combinatorial Mo_xW_{1-x} oxide thin film sample (where $0 < x < 1$) by reactive magnetron sputtering, see Fig 2-9, onto ITO-coated glass and determined the optimal composition for the best EC efficiency. A continuous composition range was deposited in an experiment on a single substrate using a combinatorial process, the sample realized the entire composition range of the MoO_3-WO_3 system.

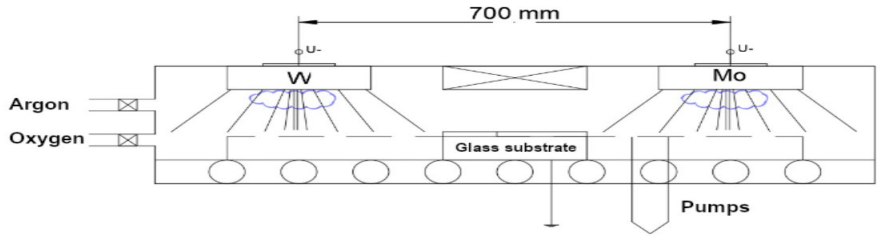

Figure 2-9 Cross-sectional schematic view of the sputtering chamber and the target arrangement [20].

For the same sputtered layers, a non-contact composition determination method was refined by spectroscopic ellipsometry. The layers proved to be amorphous according to the XRD and SEM measurements, 4 Si-probes were examined: One from the "W-side", two from the "mixed-part", and one from the "Mo-side" and found that our layers are highly amorphous. One example (from the mixed part) XRD measurement is shown in Fig. 2-10. Only one significant broad peak in the 20–30° region can be seen as the sign of amor-phous film. Crystalline peaks at higher angles can be identified as peaks of pure cubic (beta) tungsten, which was sputtered under the WO_3 and MoO_3 layers. The broad peak near 70° is from the silicon substrate. The vertical red lines show the calculated positions of beta tungsten, which is a thin (app. 100 nm) layer below the EC film. The vertical lines show the calculated positions of monoclinic, triclinic, and orthorhombic WO_3 and hex-agonal and orthorhombic MoO_3 peaks. No trace of crystalline WO_3 or MoO_3 material in the layers.

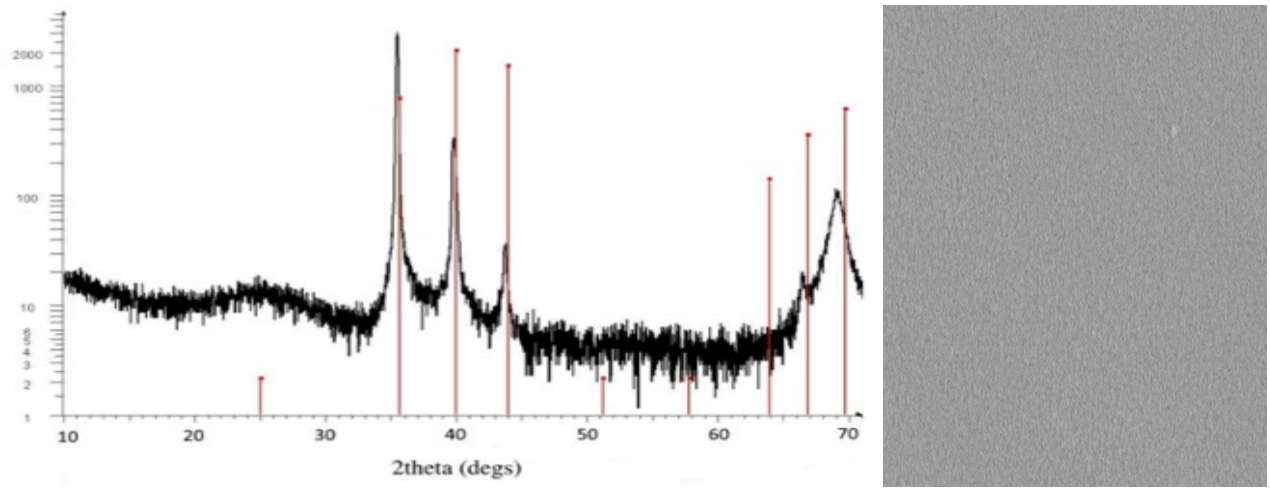

Figure 2-10 One example from the several XRD measurements showing one significant broad peak in the 20–30° region showing only amorhous microstructure in the electrochromic layer (left) 4x4 micron SEM micrograph from the center part of the combinatorial layer (right) [20].

By applied electric current through the layer and simultaneous measurement of layer transmittance, electrochromic properties of the oxide mixtures were determined. Electrochromic redox reactions were investigated in an organopropylene carbonate electrolyte cell in a standard 3-electrode arrangement. The coloration efficiency data were determined by measuring transmission in the spectral range of 400–800 nm. The CE data showed a significant maximum of around 60% MoO_3. It was possible to determine the location of the maximum with an accuracy of 5% due to the combinatorial approach, see Figure 2-11.

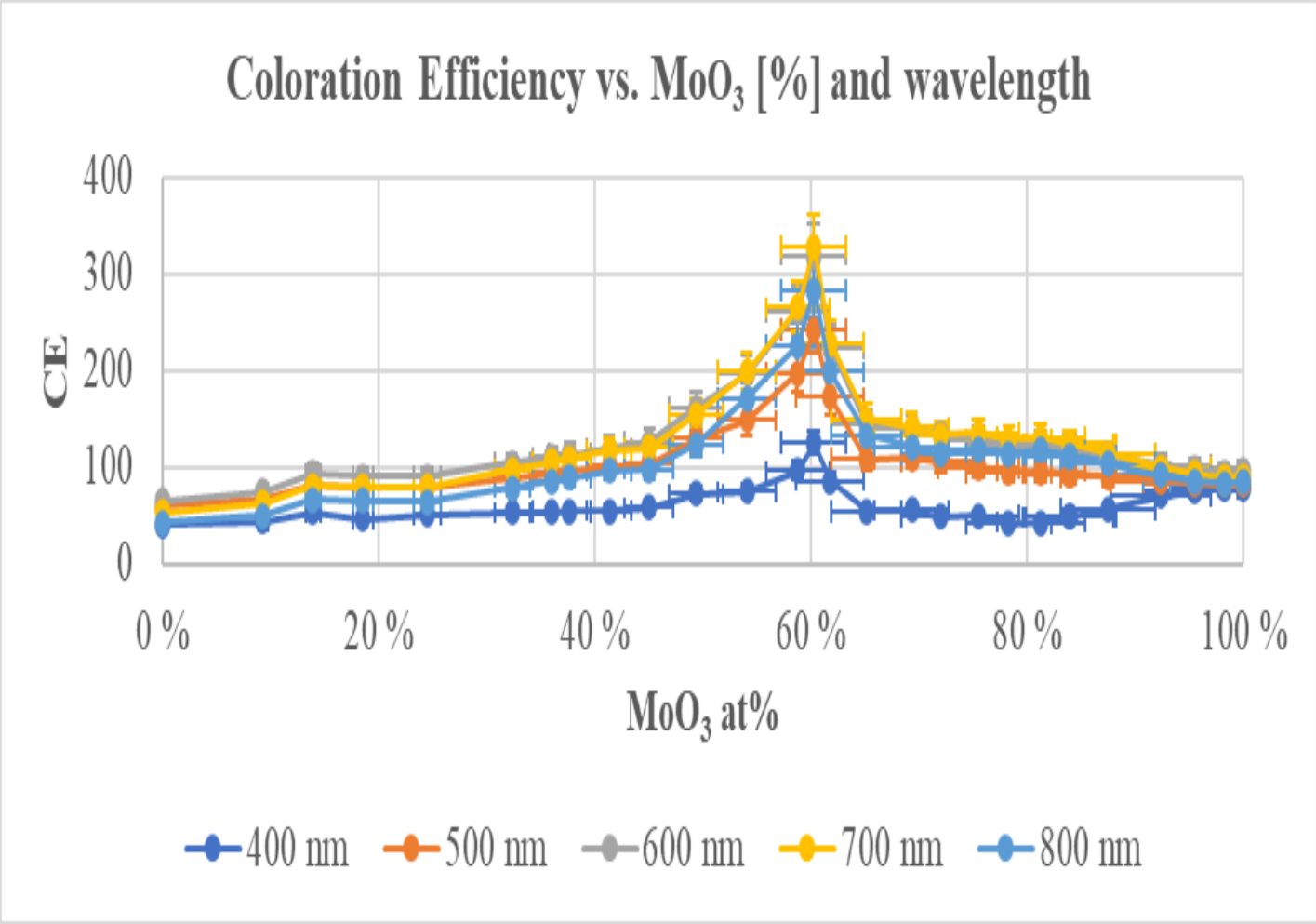

Figure 2-11 shows a significant CE maximum at 60% Mo content. This maximum increases towards the red end of the spectrum in the visible spectral range of 400-800 nm [20].

2.3.8 TiO_2–MoO_3

Shrestha et al. [110] anodized Ti-Mo mixtures to produce TiO_2–MoO_3 composite oxide nanotubes with variable composition. These nanotube layers showed significantly better electrochromic color contrast compared to pure TiO_2 nanotubes. Self-assembling binary oxide nanotube layers were made: Ti-Mo (7 wt%) alloy plate was polished to a mirror-smooth consistency and used as a working electrode in a conventional anodizing cell. It consists of a conventional three-electrode system consisting of an Ag/AgCl (3 Mol KCl) reference electrode and a Pt mesh as counter electrodes. The reflective color contrast of amorphous Ti-Mo nanotubes is 2.5 times higher than that of amorphous titanium oxide nanotubes with equal charge density.

Ezhilmaran and Bhat [111] prepared electrochromic device from a bilayer electrode with nanoparticulate TiO_2 on the substrate and MoO_3 nanograins in the top layer. The TiO_2, MoO_3 and

TiO_2/MoO_3 layers were made using spin coating on conducting Fluorine-doped tin oxide (FTO) substrates. Compared to literature data, the electrode behaved better in relation to higher current density and charge storage capacity, as well as speed. They got 40% color contrast, ~2 s switching response and 72.5 cm^2/C high CE.

The results obtained by Habashyani et al. [112] using radio frequency magnetron sputtering (RFMS) were consistent with those recently published in reference [60]. They made MoS_2 thin films using non-doped and Ti-doped perpendicular nano wall design. Using these production parameters (O_2 gas around 500 sccm, oxidation time of 45 minutes at 380°C) their layers were thermally oxidized to α-MoO_3. The samples have been labelled as follows: undoped MoO_3 -> MBO, Ti:MoO_3 with 20 W RF-power -> MTO20, Ti:MoO_3 with 30 W RF-power -> MTO30, Ti:MoO_3 with 40 W RF-power -> MTO40. Condensed nano-wall has been manufactured by Ti doping. In the visible region, and with increasing Ti concentration inside the range of coloring potential from (-0.2 to -0.45) V, Optical Modulation (OM) has been optimized. This is a proportionally low working voltage that specifies energy-saving electrochromic materials. Samples showed 52.2 % OM was the highest Ti-doped, and 37.6 % OM MoO_3 (MTO40) undoped (MTO) at (47.8 % at λ=700 nm) and (25.7 % at λ=550 nm) respectively, and the applied potential was -0.45 V. Moreover, 4.7, 4.1, 6.2, and 2.9 s were the coloring times for MBO, MTO20, MTO30, and MTO40 samples, respectively, while 3.1, 1.4, 1.1, and 1.2 s were the bleaching durations for the same samples. The MBO sample is the non-doped one, while the Mo/Ti ratio is 80 in the MTO20 sample, 17 in the MTO30 and the lowest Mo/Ti ratio is 7 in the MTO40. At the visible wavelengths, this thin film has been presented with the best OM and the best response time of coloring.

Even though the highest Ti-doped thin film was destroyed by the (MTO40) wall structure, moreover MTO30 and MTO20 samples have been implemented better at longer wavelengths with higher coloration efficiency (CE) and optical modulation (OM). The authors concluded that: The advantages effect of Ti-doping has been achieved for electrochromic parameters as: response times during bleaching and coloring of the MoO_3, OM and CE. These Ti-doped MoO_3 electrochemical attributes reveal the fitness of these materials for this type of equipment application.

2.3.9 WO_3-MoO_3-V_2O_5

Asymmetric and symmetric EC cells have been studied by Sato and Seino [113] that used the vacuum-evaporated amorphous WO_3-MoO_3-V_2O_5 films in (propylene carbonate and lithium perchlorate) solutions. They used the (reflection spectra of symmetric and transmission ones of asymmetric) cells at a certain applied voltage. Compared with pure WO_3 and V_2O_5 films, dark

displays were obtained using WO_3-MoO_3 films when negative voltages were applied, and the contrast ratio was improved. V_2O_5-MoO_3 films gave yellow and bluish displays and reddish displays were obtained with WO_3-MoO_3 films. They found improved EC properties at (60% $W0_3$ - 40% V_2O_5 composition), giving colors between brown and yellow green.

2.3.10 Ir–Ta Oxide

Seong Uk Yun et al, [114] used a reactive co-sputtering system to deposit iridium tantalum oxide thin films. They characterized the prepared IrTaOx thin layers using in situ transmittance measurements, transmission electron microscopy (TEM), X-ray photoelectron Spectroscopy (XPS), chronocoulometry and electrochemical impedance spectroscopy (EIS). By increasing Tantalum composition, they detect an increase of the oxidized iridium in IrTaOx. According to the authors the high transmittance modulation for the IrTaOx thin films was caused by the proton conductivity of tantalum. Their result showed that the $Ir_{33}Ta_{67}$ oxide thin film had 1.4 s response time, 20 cm^2/C of coloration efficiency and $5x10^{-9}$ cm^2/s ion diffusion coefficient. Based on their fast response time, enhanced IrTaOx thin films are expected to be a candidate of electrochromic materials.

2.4 Newest materials of interest in EC applications

Recent state-of-the-art developments in the field of ECDs focus on two main fields: multicolor displays and flexible devices. Chemically modified oxide based electrochromic materials offer the possibility of making color ECDs. For example, phosphonate modified mesoporous TiO_2 films displayed range of visible colors, while ferrocene electron sources blended in ion gel electrolytes made possible preparation of multicolor ECDs with low steady-state power consumption. However, most existing multicolor ECDs still lack a wide color gamut, which is necessary to achieve full-color displays [115]. In the field of flexible ECDs, graphene, silver nanowires and carbon nanotubes are used as flexible electrodes. Roll-to-roll process makes possible deposition of those materials on flexible substrates with substantially increased throughput. However, in flexible ECDs the task of uniformity across large surfaces especially under repeated deformation and mechanical stress is still far from being solved.

Recent development of organic polymers, metal supramolecular polymers and Metal–Organic Frameworks (MOFs) is regarded as the fifth generation of EC materials. These Metallo-Supramolecular Polymers (MSPs) are widely studied for their good electrochemical and optical properties, due to electronic interactions between metals and ligands [116]. The transmittance can be controlled by modifying the optical properties [117]. The protection from heat radiation through the

glass would be obtained by using coatings on glass made by films from semiconductor metal oxide. Typically, nanoscale oxides are considered according to their high thermal conductivity, low thermal expansion coefficient, and insulation. The application of this type of coating gives an advanced surface quality. The heat transfer rate and thermal conductivity are increased due to the increases in the concentration of nanoparticles [118,119].

While pure TiO_2 was investigated as an electrochromic material [87], SnO_2 or TiO_2-SnO_2 [127,128] mixtures were studied only as photocatalytic materials. The T–L model is a combination of the Tauc and Lorentz models [129]. We found only a few publications about the EC behavior of Ti-Mo mixed oxide. Mahajan et al [130] reported the positive effect of doping of Ti (0, 3, 6, 9 at%) in MoO_3 thin films prepared by spray pyrolysis technique. Shrestha et al [110] successfully fabricated self-organized TiO_2-MoO_3 composite oxide nanotubes with tunable dimensions by anodization. These nano-tube layers exhibited a significantly enhanced electrochromic color contrast compared with plain TiO_2 nanotubes. Haiyan Yu et al [131] prepared MoO_3-TiO_2 composite core/shell nanorod films by the combination of hydrothermal and electrodeposition method. They attributed the improved electrochromic properties mainly to the porous space among the nanorods array, which makes the ion diffusion easier. ZnO was investigated for different purposes: Miccoli et al. [132] reported on the DC-sputtering deposition of ZnO:Al thin films as a transparent conductive oxide, and Semong et al. [133] synthesized gold-coated ZnO/Fe_3O_4 nanocomposites as a colorimetric-sensing detector. There are different synthesis technologies for the fabrication of ZnO materials: carbothermal transport growth [134], electron beam evaporation [135] and in-plane surface epitaxy [136].

To the best of our knowledge, Zn has been investigated only as a dopant in other electrochromic metal oxides [137]. Garcia-Canadas and coworkers [138] found a similar CV pattern in the α-WO_3 electrochromic oxide-$LiClO_4$ electrolyte system. Their results show that a simple RC equivalent circuit allows us to explain the principal CV characteristics of lithium intercalation and deintercalation in amorphous films.

2.5 Conclusions from the literature

Many binary oxides were studied as potentially promising EC materials. However, most of the studies have investigated only a few compositions. Some of them studied only the role of adding a single percentage of a secondary material. Only a few examples can be found where a comprehensive investigation spanning the full compositional range between the component oxides were made. Note that in most cases the mixed metal oxides showed better EC properties than the pure oxides:

-The TiO_2 nanorods/WO_3 hybrid films reveal impressive electrochemical characteristic: the diffusion coefficient of 1.8×10^{-7} cm^2/s surpasses those of pure (WO_3 and TiO_2) nanorods.

-The Nd–Mo co-doped SnO_2/α-WO_3 ECs reveal up to 90% visible light transparency at $\lambda = 600$ nm, estimating to the conventional SnO_2/α-WO_3 ECs and after up to 1000 volatile cyclic trial, 59% electrochromic functionality drop against undoped device after up to 1000 reversible cycle test. Moreover, these doped samples displayed shorter switching time (31% of the undoped) and high coloration efficiency (~200 cm^2/C).

-The EC performance of the 1.2 wt% Antimony-doped Tin Oxide nanoparticles in WO_3 EC film was better regarding CE value (48 cm^2/C) and the switching times (2.4 s for the bleaching time and 5.4 s for the coloration time).

-40 % Ni addition to W-oxide enhanced the coloration efficiency with 80 cm^2/C.

-Higher surface roughness and clear optical modulation (41%) and high Coloration Efficiency (90 cm^2/C in red) were detected in WO_3–Ag thin films. In another experiment, the $W_{0.91}Ag_{0.09}O_{3-\delta}$ thin layer had faster switching time with a higher coloration efficiency of 67 cm^2/C than those of the $WO_{3-\delta}$ thin layer, which were 59 cm^2/C. However, transmittance modulation in the $W_{0.91}Ag_{0.09}O_{3-\delta}$ thin film was worse than in the other films.

-In V_2O_5 (85%)-WO_3 (15%) film, the electrochemical durability of the samples has been found to be stable up to 1000 cycles with 49 cm^2/C. In the films of the W-V mixed at the ratio of 1:1, electrochromic properties were measured, such as a fast coloration response of 4.9 s, an optimum optical contrast of 60%, and the highest coloration efficiency of 62 cm^2/C. Furthermore, for the electrochemical energy storage application, a maximum unit surface capacitance of 39 mF/cm^2 at an applied current of 0.5 mA/cm^2 has been reached, and it displayed a capacitive retention of 78.5%, even after 5000 charge/discharge cycles.

-The CE data showed a significant maximum magnetron sputtered WO_3 (40%)- MoO_3 (60%) composition with 200-300 cm^2/C values in the visible range.

-Magnetron sputtered SnO_2 (71%)-ZnO (29%) revealed CE values 30-40 cm^2/C as a maximum in the case of SnO_2-ZnO mixtures.

From these experiments, I found most promising the WO_3 and MoO_3 based mixtures, especially the magnetron sputtered, amorphous WO_3 (40%)-MoO_3 (60%) composition with 200-300 cm^2/C CE.

According to the U.S. Department of Energy, replacing old single-paned windows with energy-efficient replacements should save energy 7% to 15% in energy costs, roughly $71 to $501 annually. So, it's worth the effort and the expected challenges in fitting with current window systems. Windows

and doors can be made smart without replacing; they only need to fit them with smart sensors, locks or mechanisms that can be connected to your home network, usually via a smart hub. This allows them to be operated by an app on your smartphone or tablet. There are also windows and doors with integrated smart systems.

3 Experimental Methods

3.1 Magnetron sputtering (combinatorial sample preparation) apparatus

Reactive sputtering can be defined as the sputtering of elemental targets in the presence of chemically reactive gases that react with both the sputtered target material and the target surface. It has become a very popular technique in today's search for new material properties, for the deposition of a very wide range of compound and alloy thin films including oxides, nitrides, carbides, fluorides or arsenide's [139].

Metal ion source is shown according to self-sputtering plasma in a magnetron discharge. Metals revealing high self-sputtering produced such as Ag can be used in a high-power impulse magnetron sputtering discharge such that the plasma almost exclusively contains singly charged metal ions of the target material. The extracted ion beam and the plasma are tranquil. The ion beams consist mostly of an extraction voltage of 45 kV, first gap spacing of 12 mm and 10mA/cm^2 current density [140].

3.1.1 Description of our sputtering apparatus

Figure 3-1 shows the DC magnetron sputtering systems, and its parameters, Figure [(3-2a) shows the chamber for DC magnetron sputtering device and the reactive plasma while (3-2b) presents its control screen]. which is considered one of the important preparation devices in the Institute of Technical Physics and Materials Science, Centre for Energy Research (MFA).

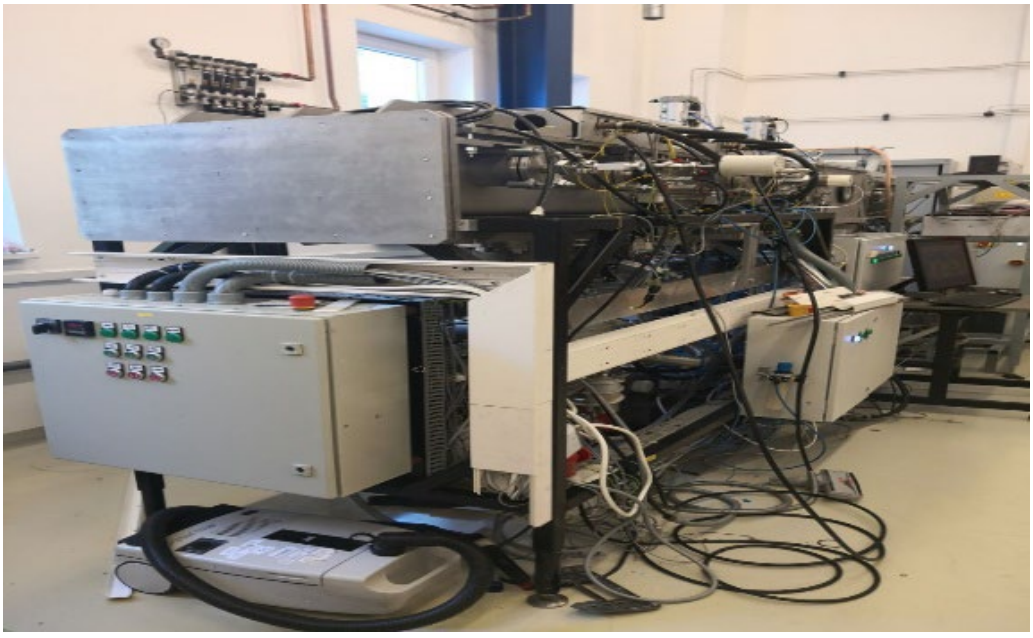

Figure 3-1 DC magnetron sputtering systems

Figure 2-9 shows the mechanism of schematic cross-section for sputtering chamber. The arrangement of the targets provides a non-uniform flux of sputtered material along the horizontal axis. Since the substrate performs a uniaxial forward and back movement, the proper choice of the left and right movement limits can result in a horizontal composition gradient on the substrate. and the movement speed was 5 cm/s (back and forth). According to the measurements, the two sputtered material fluxes overlapped around the center by using this combinatorial process, all the compositions (from 0 to 100%) were achieved in the same sputtering chamber after one sputtering experiment. Around 50–50% composition can be expected in the middle of the specimen. The Si-wafers and control Si-stripes were placed on a 30 cm × 30 cm glass sheet, the changing composition area is around the center between the two targets, and the Si samples were placed there. In the magnetron sputtering chamber (as demonstrated in figure 3-2a) the layers were deposited in a reactive ($Ar + O_2$) gas mixture, the end vacuum was ~2×10^{-6} mbar high vacuum, while the pressure of the process was ~10^{-3} mbar. Around 30 sccm/s Ar and 30 sccm/s O_2 volumetric flow rate was applied inside the chamber. For the different experiments, the substrates were ITO covered 100 mm long glasses (for transparency measurements), 4-inch diameter IC-grade and 3-inch diameter, highly conductive (0.001 Ω cm) Si-wafers (for in-situ liquid cell ellipsometry measurements) and 100 mm long Si-probes (for control measurements). The power of the plasma was in the range of 0.75–1.5 kW for the two targets and was independently controlled. About 300 walking cycles were applied with 5 cm/s movement speed. The Metal/Oxygen atomic ratio in the layers was 1:2 at the applied oxygen partial pressure.

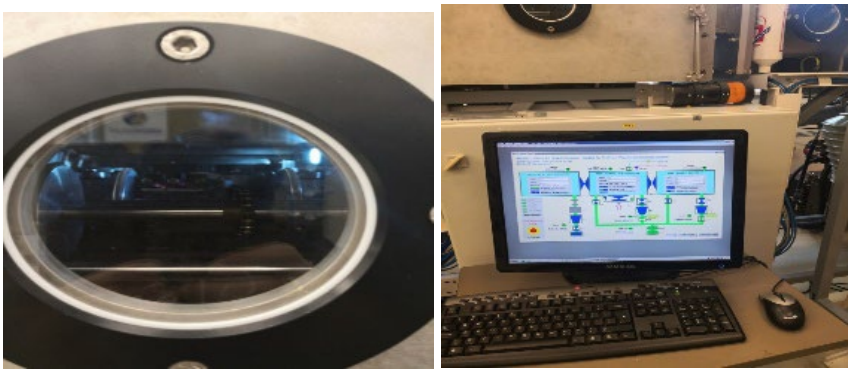

a *b*

Figure 3-2 (a) the chamber for DC magnetron sputtering. Blue light is from the Ar-O_2 plasma, (b) DC magnetron sputtering control screen.

The basis of cathode sputtering is the creation of a self-sustaining electric discharge, i.e. plasma, created in a sparse space between two electrodes. In this low pressure space, the electrons accelerate under the influence of an electric field and collide with atoms – typically noble gas ones – from which additional electrons are torn off. The positive ions thus generated hit the cathode due to the accelerating effect of the electric field, and if their energy is greater than the energy of a bond, they can eject atoms from it. The ejected atoms thus hit the surface of the substrate on the anode opposite the cathode, creating a thin film there. In the case of direct voltage (DC) sputtering, an insulating cathode would be charged in a short time, which would prevent further sputtering. Radio frequency (RF) sputtering is therefore used for the sputtering of insulators. In this case, the poles are excited with a high frequency (13.56 MHz) to avoid charging, so that in one of the half-periods the electrodes are subjected to electron bombardment, which neutralizes the positive charge. Due to the alternation of poles, the already sputtered material is also sputtered back. The extent of this is negligible, because the surface area of the cathode is much smaller than that of the anode, so the power density at the cathode is significantly higher, so the sputtering of the target is significantly faster than that of the carrier (the cathode is automatically placed on a high negative voltage due to self-charging). The disadvantage of RF sputtering is the slowness of layer building, which makes simple RF sputtering not a common method of deposition.

Magnetron sputtering was developed to increase the speed of sputtering, a process that is gaining more and more importance among the currently used technologies. However, the process of sputtering is significantly more complicated than the simple principle outlined above. Even in the case of the simplest DC sputtering, it is not clear that the ionized felt gas atoms of the plasma will sputter the target. There are several types of processes, in many cases harmful, that can take place:

•Ions may be neutralized and scattered back.

•As a result of the impact, secondary electrons can escape from the material of the target, which can also reach the carrier, thus adversely affecting the structure of the formed layer.

•The ion may be incorporated into the target.

• The crystal structure and composition of the target may change because of the impact. Interstitial defect sites and holes can be created, and in the case of a compound target, the stoichiometry of the target can change.

•Finally, which is the only interaction that is directly beneficial for sputtering, ions can eject atoms from the target surface. These atoms can then build up the thin film on the substrate on the anode in a favorable case.

The properties of the thin film formed during sputtering are also influenced by several parameters, the effects of which cannot always be formulated in general terms. The most important of these parameters are:

•Substrate temperature. By increasing the temperature of the substrate, a more stable and better structured layer can be created. However, above a certain temperature (different depending on the material), the quality of the formed layer may occasionally begin to deteriorate.

• Gas pressure of the vacuum. If the pressure is too low, plasma will not be able to form or will become inhomogeneous. In the case of separations around such pressure, the detached thin film becomes unreproducible due to the uncertainty of the plasma. At too high pressure, enough ions are produced to maintain the plasma and ensure a sufficient yield of sputtering, but the free path of the particles is greatly reduced by the pressure. As a result, the ions are scattered and do not reach the surface of the target with little or no energy.

•The power density of the target. If the power density is too high, electron bombardment on the substrate will degrade the layer quality.

•The target substrate distance (working distance). If the value is too high, the rate of layer construction will be lower due to scatterings, and the long distance assumes a larger and more expensive system. At a short distance, the layer will be more inhomogeneous. The optimal distance is influenced by the parameters of the separation and the energy of the atoms arriving from the target to the carrier.

•The position on the sample holder. When designing the equipment, efforts are made to ensure the greatest possible uniformity on the surface of the sample holder, but usually there are inhomogeneities near the edges [141].

3.1.2 Reactive sputtering

Reactive sputtering differs from the simple sputtering process outlined above in that not only noble gas atoms are introduced into the gas space, but also the gas to be reacted with atoms sputtered from the target material. Gas thus entering the reaction field - similarly to the atoms of a noble gas - is ionized. The ionized atoms form a compound on the surface of the carrier with the atoms of the target

and their ions brought into the gas phase. In the case of reactive sputtering, it is important to note that the molecules that make up the material of the thin film do not form in the gas space, the reaction can only take place on the surface of the carrier or the target. Reactive sputtering has three very important advantages over non-reactive separation from a compound target.

1. Allows the separation of compounds from metal targets. This is of great importance because the use of a metal target allows for faster sputtering. Furthermore, there is no need to fear that the stoichiometric composition of the target will change because of the impact of ions. Another significant advantage is that metal targets are significantly cheaper than compound (ceramic) targets.

2. Insulating thin films can be deposited by DC sputtering. The material of the thin film is formed only on the surface. Thanks to this, the material of the target can be metal. In the case of a metal target, a DC source can also be used for ion bombardment, which could not be done in the case of an insulating target, because the insulator would be charged quickly, making further sputtering impossible.

3. The composition of the layers can be controlled. Since the composition of the forming layer depends on the parameters of the sputtering, by changing these we can influence the properties of the forming layer in a wide range. Of course, just like the ions of noble gas, the ions of the reaction gas can interact with the atoms of the target in several ways, as already listed above.

3.1.3 Magnetron sputtering

Another common design principle in sputtering equipment is the so-called planar magnetron. Its essence is that there is a strong magnet behind the target (typically a permanent magnet due to its simpler structure, but it can also be an electromagnet). The advantages of this arrangement include the fact that it can be used for both DC and RF excitation, and that it allows for good layer building rates.

During conventional sputtering (i.e. without the use of a magnetic field), the secondary electrons emitted from the target are accelerated by the electric field in a straight line towards the anode. The energy of these electrons is typically converted into heat and causes heating of the carrier or one of the machine elements, or radiation damage. However, from the point of view of equipment construction, this can be seen as a loss, since these charges exit the plasma volume without suffering an ionizing collision. This problem is solved by applying the magnetic field by increasing the number of ionizing collisions. The magnets are fixed behind the flat cathode surface in such a way that the closed lines of force of the resulting magnetic field (B) on the other side of the target, ideally leaving

and returning perpendicular to the cathode surface, run parallel to the surface of the target, which also means that they are perpendicular to the electric field force vector. In the force field thus formed, the motion of a particle with a charge q of mass m and an initial velocity v_0 perpendicular to the magnetic field B can be described as follows: The charged particle is subject to the Lorentz force:

$$F=qv_xB \quad (2)$$

Where F is the Lorentz force, B is the magnetic field, q is the charge and v_x is the velocity.

Substituting the characteristic values of the Ar^+ ion and the electron into this relationship, we get that the radius of the circular orbit of the Ar^+ ion is about 300 times the radius of the circular orbit run by the electron. This can be interpreted with a good approximation that if an ion passes through this part of space, its direction is only negligibly influenced by the Lorentz force, it continues its journey in an almost straight line, while the electrons are significantly deflected by the same force.

The accelerating effect of the electric field force acting simultaneously and the Lorentz forces deflected the electron into a cycloid orbit. If the magnetic field is strong enough, a component of the electron's velocity is formed pointing towards the target, and the electron leaves the magnetic field. Then, when it approaches the surface of the cathode, the negative electric field exerts a restraining effect on it, causing the electron to become a dead center for a moment. Then it starts to accelerate again, and the cyclical process starts again.

The movement of secondary electrons in a cycloid orbit typically lasts until a collision with an Ar atom. Although not all collisions lead to ionization, the ionization efficiency is significantly increased by the installation of the magnetron. Due to the electrons trapped in this way, the discharge current density of the target can increase to 10-100 mA/cm^2 compared to $1mA/cm^2$ for sputtering systems without a magnetron.

3.1.4 DC reactive magnetron sputtering and its inference

The instability in the reactive gas pressure and hysteresis effect, differential poisoning of the magnetron cathode. We can control the procedure by:

1- Raising the distance between the target-to-substrate, will need large vacuum chambers consequences, more costly and minimizing the deposition rates.

2- If we want to raise the pumping speed, that will be more costly.

3- Pulsed reactive gas flow will need a huge amount of procedure enhancement and sustained monitoring and adapting the parameters of the process.

4- The reduction of deposition rate caused by obstructing reactive gas flow to the cathode and that will require more complex procedures.

5- In real time without disquieting the discharge voltage control, which is cheap and has proved to be powerful techniques for monitoring and controlling the reactive sputtering procedures.

6- Observing the plasma emission [139].

3.1.4 Specific properties of the MTA MFA home-built sputtering chamber

We present here the largest facilities of the solar cell research and development in Hungary-the Solar Cell Technology Innovation Center. The R&D equipment is an integrated vacuum system designed and built for the preparation of thin film Copper Indium Gallium diSelenide (CIGS) solar cell layer structures. The facility was built on the premises of the Hungarian Academy of Sciences by the Energosolar Co. in the frame of a main project funded by the Hungarian National Office for Research and Technology. The layout of the solar cell structure and the equipment for its preparation introduces the main materials science issues raised in the CIGS system and presents challenges for research [142]. The system was designed and built by Energosolar Co. Figure 3-3 shows the schematic layout of the equipment.

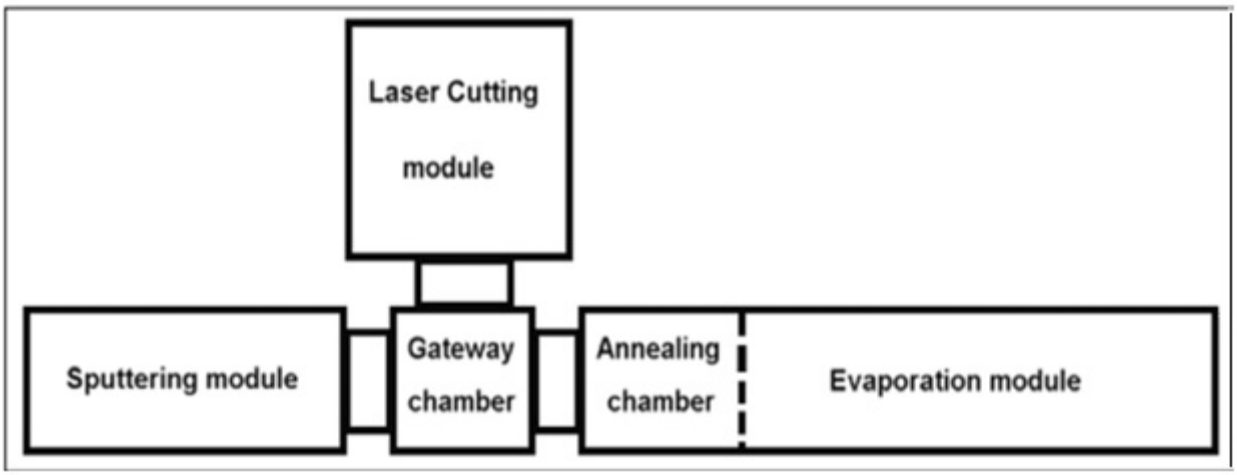

Figure 3-3 Schematic layout of the integrated vacuum system [142].

Al doped ZnO (ZAO) thin films (with Al-doping levels 2 at.%) were deposited at different deposition parameters on silicon substrate by reactive magnetron sputtering for solar cell contacts, the results show correlation between specific resistance and band gap energy and direct exciton strength parameter. The sputter deposition chamber (manufactured by Energosolar, Hungary)

forms an integral part of a more complex vacuum system containing evaporation, structuring and gateway chambers, see table 3-1 [143].

Table 3-1: Deposition parameters and specific resistances [143]

Sample	Vacuum [mBar]	Ar [sccm]	O_2 [sccm]	Pressure [mBar]	Power (W)	Voltage (V)	Thickness [nm]	Specific resistance [Ω cm]
A5	1.5 E-06	35	15	6.4 E-03	500	292	620	4.32 E-02
A6	2.0 E-06	35	15	6.4 E-03	625	320	442	1.04 E-01
A7	3.0 E-06	35	15	6.5 E-03	650	330	433	1.02 E-00
A8	4.5 E-06	35	15	6.7 E-03	725	340	605	6.66 E-02
A16	9.2 E-06	35	15	6.5 E-03	725	334	365	3.47 E-03
A25	5.9 E-06	35	15	6.5 E-03	725	332	260	1.85 E-04
A27	3.7 E-06	35	15	6.0 E-03	750	332	540	1.94 E-02
C1	1.33 E-06	35	15	1.03 E-02	725	314	198	2.76 E-01
C14	3.19 E-06	35	15	9.45 E-03	955	332	305	5.45 E-01
C15	1.03 E-06	35	15	1.16 E-02	975	359	300	5.55 E-01
C17	1.80 E-06	35	15	5.75 E-03	650	339	330	5.28 E-01
C18	4.00 E-06	35	15	5.00 E-03	700	330	290	5.79 E-01
C19	1.80 E-06	35	15	5.01 E-3	675	340	320	4.86 E-03
C21	6.70 E-07	40	10	5.20 E-03	500	324	350	1.02 E-04
C22	2.60 E-06	37	13	4.90 E-03	550	327	250	2.90 E-02
C23	1.16 E-06	30	20	4.80 E-03	970	344	407	7.15 E-01

Properties of the reactive plasma were monitored. Our results show two characteristic behaviors (hysteresis and oscillation). A qualitative physical explanation for spontaneous and stable plasma oscillations is provided. Necessary conditions for the formation of the oscillation phenomena are studied as a function of oxygen mass flow and power. Apart from the well known hysteresis phenomena, stable and reproducible plasma oscillations were also found during ZnO reactive sputtering. A qualitative explanation was given based on the concurrent sputtering and oxidation rate. Mechanical movement, gas pressure and composition, DC electric supply and additional pulse parameters were monitored and fully computer controlled. The target characteristics were taken from the computer log. [144].

3.2 Characterization methods

There is a variety method of thin-film characterization either non-destructive fast ones with limited depth information [146] or whole-depth time-consuming destructive ones when depth profiling is achieved [145].

3.2.1 Spectroscopic Ellipsometry (SE)

One of the Methods of thin film characterization nondestructive techniques is Spectroscopic Ellipsometry. Many researchers have used SE for pure or combinatorial material investigation [120-125]. The combinatorial approach used to analyze mixed metal oxides has several advantages. Fried et al. [126] have used SE (which is a fast, cost-effective, and non-destructive method) for the investigation and mapping of WO_3-MoO_3 mixed layers after sputtering. Different optical models, such as EMA and 2T–L, have been used to achieve the composition map and thickness map of the sample layers. The T–L model is a combination of the Tauc and Lorentz models [129].

One of the important characterization devices in the Institute of Technical Physics and Materials Science, Centre for Energy Research (MFA) is the SE Woollam M-2000DI rotating compensator spectroscopic ellipsometer presented Figure 3-3.

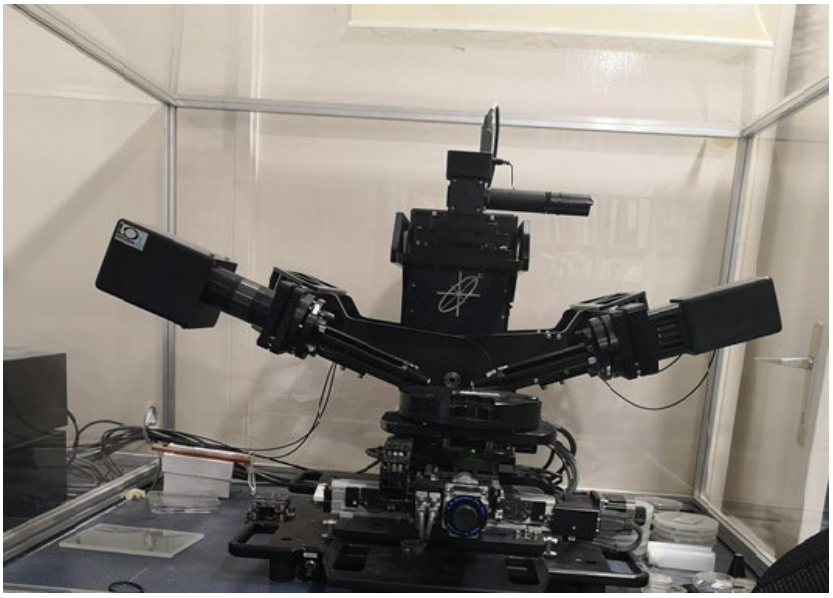

Figure 3-4 Spectroscopic Ellipsometry devices, Woollam M-2000DI.

Main characteristics of the equipment are:

Available wavelength range is 191-1690 nm (photon energies of 0.7-6.5 eV)

Automatic scan with a micro-focused (ca. 0.2 mm) spot.

Angle of incidence: 45-75 degrees.

Measurement time 1 sec per spot.

High-resolution, high-accuracy map over 15x15 cm area within a reasonable time.

Figure 3-4 shows SE Data analysis parameters from the computer connected, which presents data acquisition and analysis software CompleteEase,

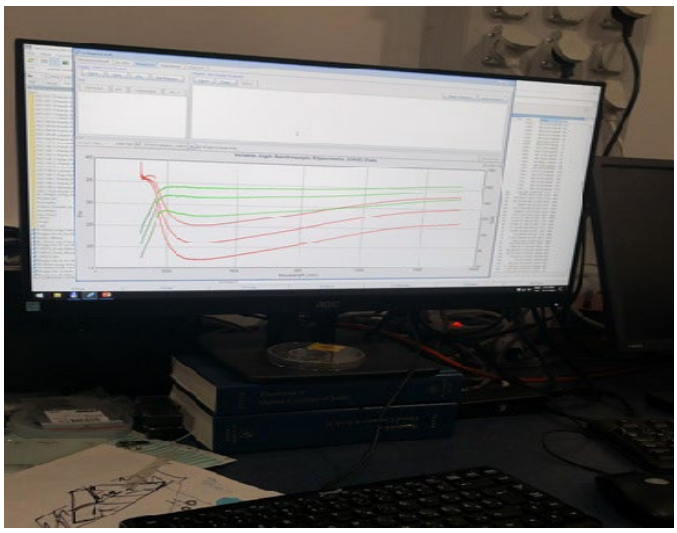

Figure 3-5 a sample for data analysis parameters for Spectroscopic Ellipsometry device.

3.2.1.1 Principles of SE

Ellipsometry determines angle-of-incidence-dependent relative amplitude ratios and phase difference shifts of orthogonal electric field components typically defined as parallel and perpendicular to the plane of incidence upon specular reflection of light from a planar surface [147].

Figure 3-6 shows the principles of Spectroscopic Ellipsometry device [148].

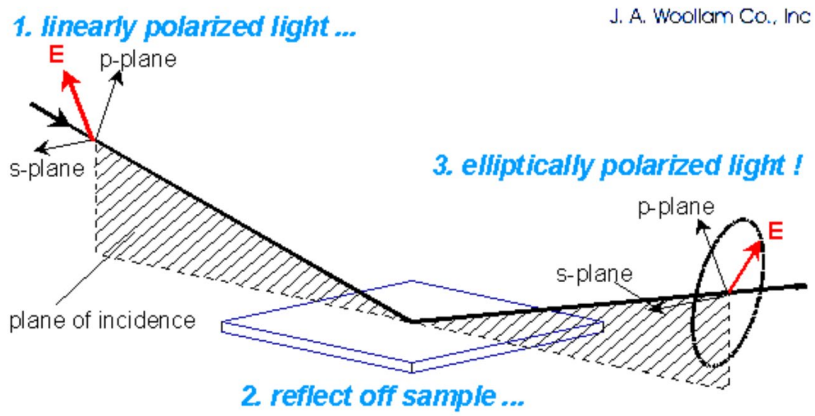

Figure 3-6 the principles of Spectroscopic Ellipsometry device [148].

3.2.1.2 The advantages of SE

High precision (thickness sensitivity: ~0.1 Å), fast measurement, nondestructive measurement, wide application area, various characterizations including optical constants and film thicknesses are possible and Real-time monitoring (feedback control) is possible [147].

3.2.1.3 The disadvantages of SE

Necessity of an optical model in data analysis (indirect characterization), data analysis tends to be complicated, low spatial resolution (spot size: several mm) and difficulty in the characterization of low absorption coefficients < 100 cm^{-1} [147].

3.2.1.4 SE Compositional mapping (Comparison of the Optical Models)

Mapping means that a spot of individual measurements has been moved corresponding to the surface [149]. If we consider it as a mixture of clear phases, then we should use the Bruggeman Effective Medium Approximation (BEMA) optical model [150]. Equation (3) shows BEMA, where the constituents are considered coequal

$$0 = \sum f_i(\varepsilon_i - \varepsilon)/(\varepsilon_i + 2\varepsilon) \quad (3)$$

where ε is the effective complex dielectric function of the composite layer; f_i and ε_i denote the volume fraction and the complex dielectric function of the component. In the case of two components, the equation formula is a complex quadratic, where the unknown is the effective dielectric function (ε), and we can select the good solution, as the wrong solution is physically meaningless. Dielectric functions of the two constituents were determined from the extreme edges of the Si-stripes where the TiO_2 and SnO_2 are in a pure format.

If we consider the mixture as an atomic-scale mixture, the Tauc–Lorentz (T–L) oscillator model is more appropriate [129]. The Tauc–Lorentz (T–L) oscillator model contains four parameters: transition amplitude (oscillator strength), broadening coefficient of the Lorentz oscillator, peak position for the Lorentz oscillator, and band gap energy (E_g), which is taken to be the photon energy where $\varepsilon_2(E)$ reaches zero. When the E photon energy is less than the band gap energy, Eg, $\varepsilon_2(E)$ is zero. The real part of the dielectric function $\varepsilon_1(E)$ can be obtained from $\varepsilon_2(E)$ through the Kramers–Kronig relation. In the mixed layers, five fitting parameters were used: two amplitudes for each material (oscillator strengths), interface and surface roughness thickness, and the main layer thickness.

For the electrochromic measurements, where the light absorption was measured in the visible wavelength region over 400 nm, I used the simple Cauchy formula to describe the complex refractive index as in Equations (4)– (6):

$$N = n + ik \tag{4}$$

where i is the imaginary unit, k is the imaginary part (extinction), N is the complex refractive index, and n is the real part of N.

$$n(\lambda) = A + B/\lambda^2 + C/\lambda^4 \tag{5}$$

$$k(\lambda) = ke^{U(1239.84/\lambda - Eb)} \tag{6}$$

where U, A, B, C, and k are the fitted parameters. The complex dielectric function (ε) and the complex refractive index (N) are coequal, as in the Equations (7)–(9):

$$(\varepsilon) = \varepsilon_1 + i\,\varepsilon_2 = N^2 \tag{7}$$

$$\varepsilon_1 = n^2 - k^2 \tag{8}$$

$$\varepsilon_2 = 2nk \tag{9}$$

To evaluate the real-time measurement, I used a 2-layer optical model with the Cauchy dispersion. To estimate the change after the colorization process, I used a simple 1-layer optical model with the Cauchy dispersion. The Mean Squared Error (MSE), is used to quantify the difference between curves, the model is better if the MSE values are significantly lower, because the lower MSE

indicates a better fit and better optical model [147]. Figure 3-7 presents the mechanism of SE measurements and evaluation [148].

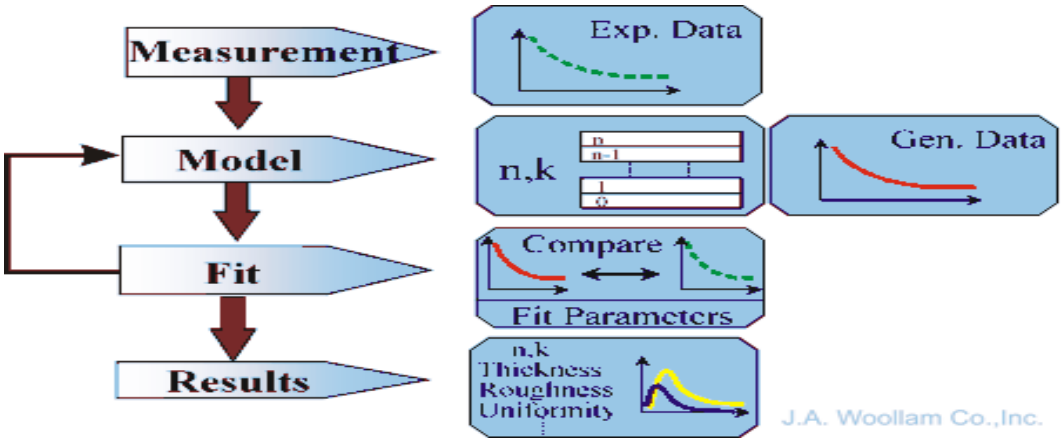

Figure 3-7 Mechanism of SE measurements and evaluation [148].

Figure 3-8 presents a schematic for SE measurements [147].

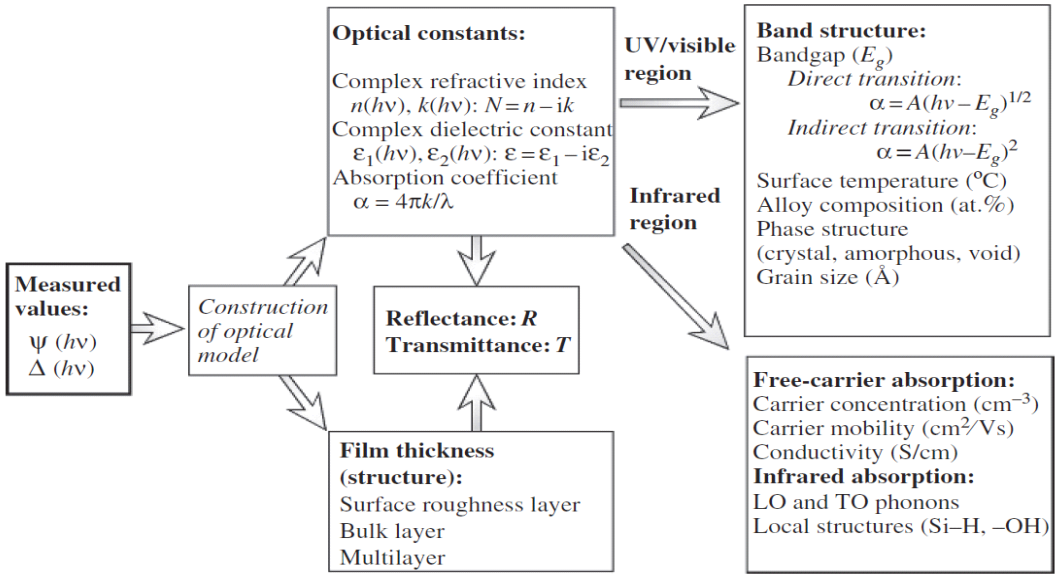

Figure 3-8 Schematic for SE measurements [147].

$$\rho = \tan(\varphi)e^{i\Delta} \tag{10}$$

$$\rho = r_p / r_s \tag{11}$$

Where φ is the amplitude in degree unit (Psi), Δ is the phase difference in degree unit (Delta), r_p is the reflection coefficient for p polarization r_s is the reflection coefficient for s polarization.

3.2.2 Scanning Electron Microscopy (SEM) with Energy-Dispersive X-ray Spectroscopy (EDS)

Spectroscopy has been identified as the important and essential instrument for structure establishment and analysis. Spectroscopy was defined as the study of the quantitative interaction between matter and electromagnetic radiation [151].

3.2.2.1 Scanning electron microscopy (SEM)

SEM is an important electron microscopy instrument that can provide detailed visual image of a particle with high-quality and spatial resolution. The specimen is exposed in SEM to the high-energy electron beam and by using the accessory methods with SEM, can give details about composition, chemistry orientation of grains, morphology, crystallographic information, topography etc. of a material, so the SEM has been considered an important instrument to be applied for materials characterization [152]. Table 3-2: presented a description of SEM specifications.

Table 3-2: Description of SEM specifications.

Specifications	**Results**
Type of electrons	Scattered, scanning electrons
High tension	~1–30 kV
Specimen thickness	Any thickness
Type of info	3D image of surface
Max. magnification	Up to ~1–2 million times
Max. FOV	Large
Optimal spatial resolution	~0.5 nm
Image formation	Electrons are captured and counted by detectors, image on PC screen
Operation	Little or no sample preparation, easy to use

The first SEM patent was in 1935 by Max Knoll in Berlin. Manfred von Ardenne in Berlin had been given a contract by Siemens to develop an SEM [153]. Figure 3-9 presents all SEM components and Schematic of scanning electron microscope (SEM) [154].

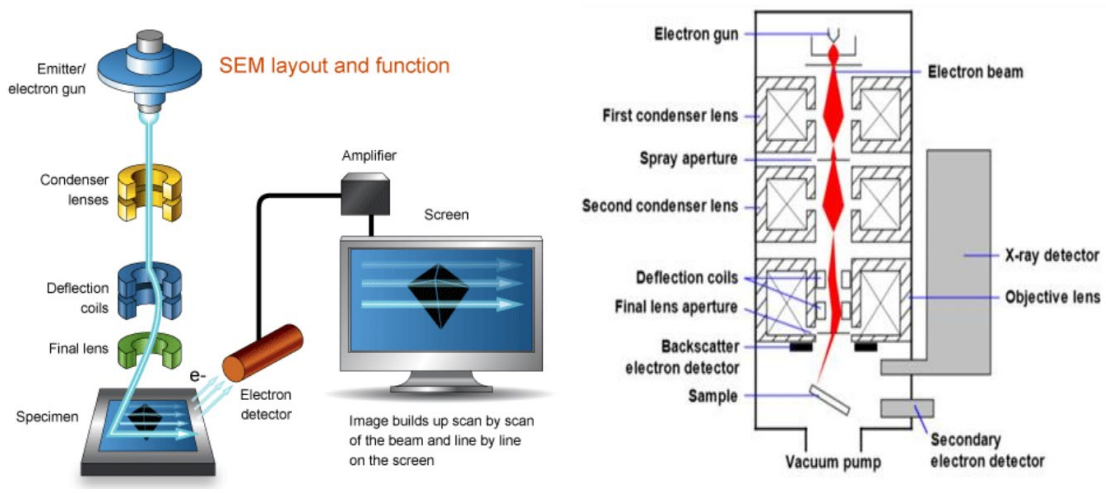

a *b*

Figure 3-9 a) All SEM components; b) Schematic of scanning electron microscope (SEM) [154].

SEM is the solution for invisible worlds of nano space and micro space that could be observed. Aspects and intricacies that are secluded by light microscopy can be discovered by SEM. The existence of EDS capability with SEM instruments is essential for qualitative and quantitative analysis for any specimen. In the absence of EDS only information on the surface topography of the specimen can be produced through SEM [154].

3.2.2.2 Energy-Dispersive X-ray Spectroscopy (EDS)

Energy-Dispersive X-Ray Spectroscopy (EDS) is a tool applied with (Transmission and Scanning) Electron Microscopes to investigate the elemental structure of a specimen. High energy electrons of the incident electron beam could ionize an electron from an inner shell. Since each element has a set of X-ray peaks characteristic to the inner shell excitations , we can detect the elemental composition of the sample by the detection of the X-ray spectra from the excited specimen. Emission of a specific X-ray photon caused by decay of this excited state. Then the X-ray photon has been captured by an EDS detector and calculates its energy. Figure 3-10 presents the schematic of EDS, an electron beam (energy between 0 and 15 keV) impinges on the sample (orange, left). X-rays and electrons leave the sample. Some of these are directed at the EDS detector (blue, right). A collimator ensures that only the sample is visible to the detector, and a compact electrostatic deflector removes electrons, so that only X-rays reach the EDS detector. A center ring is used to accurately align the line-of-sight from sample to detector. While surface sensitivity can be enhanced by reducing electron energy, there are also fewer X-ray lines available at lower electron energy, so that a careful choice must be made

between surface sensitivity and elemental sensitivity [155]. Figure 3-11 presents SEM equipped with EDS [154].

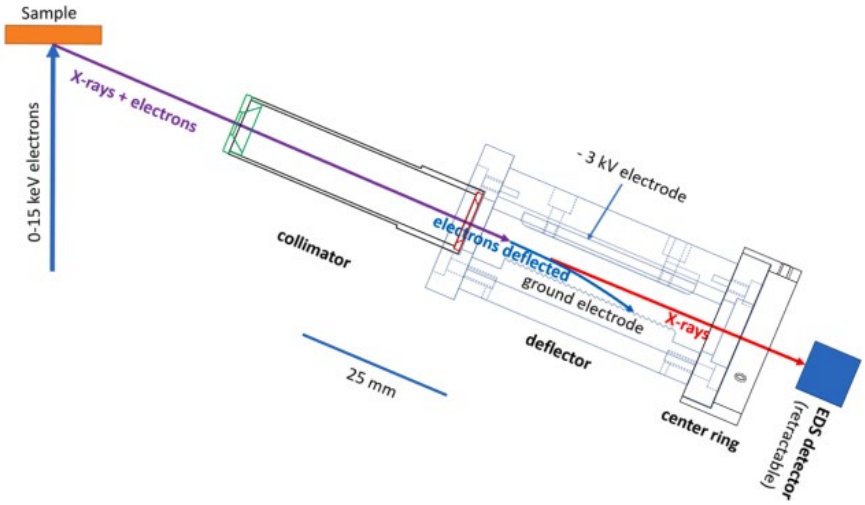

Figure 3-10 schematic view of the experimental setup of EDS [155].

Figure 3-11 SEM equipped with EDS [154].

3.2.4 X-ray Diffraction (XRD)

X-ray diffraction (XRD) is a useful measuring technique which can determine bulk or thin film sample's crystalline structure. It can determine sample crystallinity and phase purity.

Monochromic X-ray beams are good for XRD purposes because their wavelength is similar to the spacing between atoms in the sample which makes diffraction possible (pattern of longer wavelength photons is not altered by the spacing between solid state lattice points). The x-rays are going through and interact with the sample which plays the role of a grating and changing the direction of the beam

at some different angle, theta, from the original beam. This is the angle of diffraction. Most of these diffracted beams cancel each other out, but some of them will be in phase and then constructive interference occurs. In this case, the x-ray beams that are whole number integers of the same wavelength add together to create a new beam with a higher amplitude. Then a greater signal for this specific angle of diffraction will be detected. This angle of diffraction can then be used to determine the distance between atomic planes using Bragg's law:

$\sin\Theta=n\lambda/2d$

where λ is the wavelength of X-ray, Θ is the diffraction angle, and d is the distance between atomic planes. This distance between atomic planes can then be used to determine crystalline structure or phase composition.

XRD analysis has been used to determine the morphology of small crystalline samples (crystalline phases and their proportions). [156,157].

Our measurements were performed by X-ray Diffraction (XRD), Bruker AXS D8 Discover device (Billerica, MA, USA) to investigate the microstructure of the sample layers.

3.2.4.1 XRD Applications

XRD Bruker AXS D8 has been used composition determination, stress, texture measurements phase analysis layer thicknesses (in sub-micron range, depending on composition), roughness, densities and Knife-edges can be used to restrict the measured area [158]. See Figures (3-12 a and b).

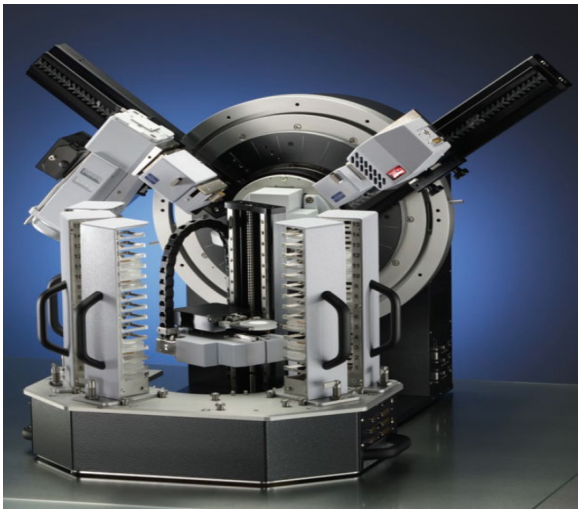

Figure 3-12 XRD Bruker AXS D8 instrument[158].

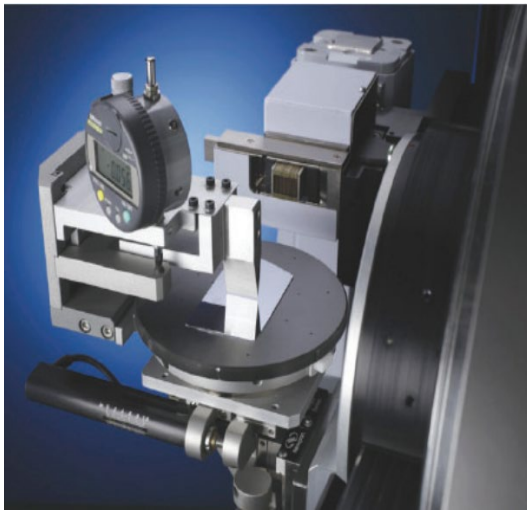

Figure 3-13 The sample area of a reflectometry setup for XRD Bruker AXS D8 instrument [158].

3.2.5 Functioning of SEM, EDS and XRD

SEM, EDS and XRD are instruments that are used to aspect materials, each one has been contingent to provide different kinds of details. SEM supplies high-resolution images of a material's surface, exhibitionist its structure and morphology. EDS, has been paired with SEM, provides the elemental composition of the material. XRD investigates the phase composition and the crystal structure of a material [151-158].

We checked the resulting compositional map for the Si-probes using an SCIOS2 Scanning Electron Microscope (SEM) (Thermo Fisher Scientific, Waltham, MA, USA) with Energy-Dispersive X-ray Spectroscopy (EDS), X-ray Diffraction (XRD) measurements were performed on a Bruker AXS D8 Discover device (Billerica, MA, USA) to investigate the microstructure of the layers. Experimental details of our XRD measurements will be given in chapter 4.3.2.

Scanning Electron Microscopy (SEM) and Energy-Dispersive X-ray Spectroscopy (EDS) measurements were carried out to check the SE results, for our samples. For istance, we examined the Si-probes of our samples and show three characteristic diffractograms, one from the “right side”, one from the “mixed-part” and one from the “left-side” and found that the “right side” and the “mixed-part” layers are amorphous, but the “left-side” is a mixture of amorphous and nanocrystalline (with crystallites of less than 10 nm in size).

SEM utilizes a focused beam of electrons to scan the surface of a specimen. The interaction between the sample and electron beam has produced diverse signals, comprehensive backscattered electrons,

secondary electrons and X-rays. These signals are revealed and utilized to produce an image of the specimen's surface.

EDS reveal the characteristic X-rays released when the electron beam in SEM interacts with the specimen. When an electron beam stimulates atoms in the specimen, inner-shell electrons are emitted, creating empty space, then the electrons from higher energy levels fill these spaces, emitting energy as X-rays.

XRD inspected the diffraction pattern fabricated when X-rays penetrated a crystalline material. The X-rays are diffracted by the orderly diverged atomic planes inside the crystal lattice. The intensities and diffraction angles of the diffracted X-rays have been measured and utilized to induce the phase composition and crystal structure of the material [151-158].

4 Experimental Work

4.1 Introduction

During this work, I developed a new method for preparing combinatorial binary oxide samples in the full composition range. I prepared combinatorial samples by moving the pure samples under sputtering targets in a reactive Argon-Oxygen (Ar-O_2) gas mixture.

By using this combinatorial process, all the compositions (from 0 to 100%) were achieved in the same sputtering chamber after one sputtering. The work of this instrument has been demonstrated before in figure 3-2a where the layers were deposited in a reactive (Ar + O_2) gas mixture (end vacuum ~2 × 10^{-6} mbar) where the pressure of the process was ~10^{-3} mbar. Around 30 sccm/s Ar and 30 sccm/s O_2 volumetric flow rate was applied inside the chamber. The substrates were 4-inch diameter IC-grade and 3-inch diameter, highly conductive (0.001 Ω cm) Si-wafers. Around 50–50% composition can be expected in the middle of the specimen. A single sample preparation took 4 h in the vacuum chamber, including the vacuum preparation time.

The deposited films were characterized, mapped (composition and thickness maps) using spectroscopic ellipsometry (SE) which is a rapid, cost-effective, and contactless (non-destructive) method, Scanning Electron Microscopy (SEM) with Energy Dispersive X-ray Spectroscopy (EDS), and XRD coloration efficiency (CE) measurements. Our aim is to assess the results of investigations of these types of materials showing enhanced electrochromic behavior compared to pure materials.

In order to determine the Coloration Efficiency chronoamperometric experiments in $LiClO_4$-propylene carbonate solutions were carried out with simultaneous transmittance spectra measurements Optical properties of our thin films in coloured and bleached state were compared .

The objective of this work was to investigate the electrochromic effectiveness (the change of light absorption for the same electric charge) of our samples.

We expected that using metal atoms with different sizes in diameters in the layers would have a positive effect for enhancing the CE. This work aims to assess the results of investigations of such materials showing enhanced electrochromic behavior compared to pure materials and to enhance Coloration Efficiency.

- For the **first sample:**

TiO_2-SnO_2 mixed layers were deposited in a full compositional range onto silicon wafers [58].and the electrochromic properties were determined by Spectroscopic Ellipsometry. There is no such publication where pure SnO_2 or TiO_2-SnO_2 mixtures are studied as electrochromic material.

- For the **second sample:**

TiO_2-MoO_3 mixed layers were deposited in a full compositional range onto ITO covered glass substrates and Si. CE of mixed metal oxides (TiO_2-MoO_3) was studied in an electrochemical cell [59]. A combinatorial material synthesis approach has been applied for the binary TiO_2-MoO_3 system. By using organic propylene carbonate electrolyte cells in a conventional three-electrode configuration, electrochromic redox reactions have been made. The electrochemical redox reactions were simultaneously followed by transparency measurements. Coloration efficiency data has been evaluated from the primary data plotted against the composition displayed a characteristic maximum at around 60% MoO_3. The localization of the maximum at 5% accuracy has been allowed in that combinatorial approach [20]. The electrochromic effectiveness of TiO_2-MoO_3 mixed layers in a wide compositional range by determination of CE as a function of composition.

- For the **third sample:**

I performed an electrochromic investigation to optimize the composition of tin oxide and zinc oxide (SnO_2-ZnO). A positive effect was achieved by using metal atoms with different diameters in the layers [60]. I determine the CE and investigate the electrochromic effectiveness of SnO_2-ZnO mixed layers in a wide compositional range. There are no publications where pure SnO_2 or ZnO-SnO_2 mixtures are studied as electrochromic materials.

4.2 TiO_2-SnO_2

4.2.1 Materials and Methods

The mechanism of the DC magnetron sputtering device as in the geometry has been presented in Figure 4-1a which shows that the sputtering targets were placed 35 cm from each other, and the movement speed was 5 cm/s (back and forth). The Si-wafers and control Si-stripes were placed on a 30 cm × 30 cm glass, as shown in Figure 4-1a. The changing composition area is around the center between the two targets, and the Si samples were placed there. The power of the plasma was in the range of 0.75–1.5 kW for the two targets and was independently controlled. About 300 walking

cycles were applied with 5 cm/s movement speed. The Metal/Oxygen atomic ratio in the layers was 1:2 at the applied oxygen partial pressure according to the SEM–EDS analysis technique. Figure 4-1b presents a photograph of (30x30) cm substrate with composition gradient layers, the colored bands show thickness and composition gradient.

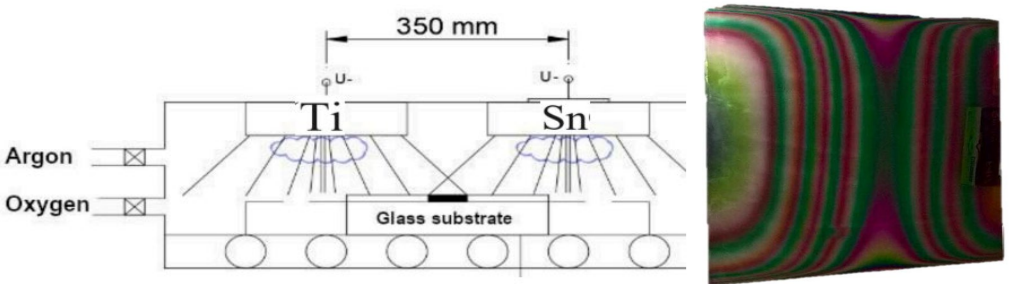

a *b*

Figure 4-1 (a) arrangements of the two targets in a closer position (35 cm from each other); (b) photograph of 30x30 cm substrate with composition-gradient layers. Colored bands show thickness and composition gradient.

The optical mapping [149] was performed using Woollam M2000 SE, and the measurements were evaluated with the CompleteEASE v. 5.15 software [148]. To obtain the mapping parameters, oscillator functions and compact optical models were used. The applicability of the optical model can be judged from the value of the Mean Squared Error (MSE), so a lower MSE indicates a better fit because of the difference between the curves [147]. The silicon wafers and Si-stripes (Figure 4-2a) were used for SEM and Dual-beam SEM + FIB Thermo Scientific Scios2, with EDS measurements as well (Figure 4-2b). The Ti/Sn ratio was calculated point-by-point to compare and validate the results of the SE evaluation.

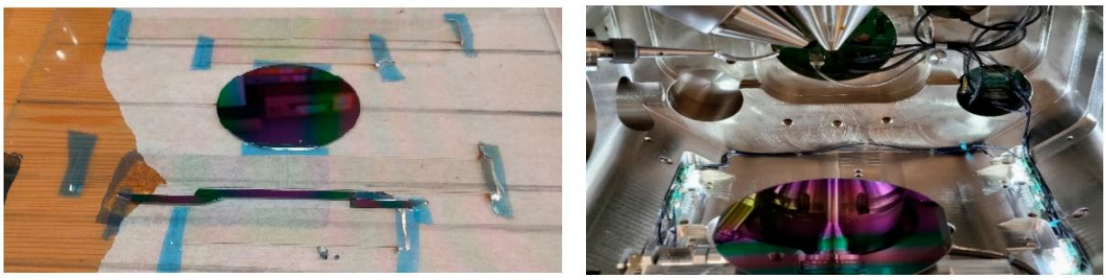

a *b*

Figure 4-2 (a) Graded TiO_2–SnO_2 layer on 3-inch Si (circular sample, upper) and the Si-stripe samples, lower; (b) Combinatorial TiO_2-SnO_2 layer on a 4-inch Si-wafer in the SEM-chamber (Dual-beam SEM+ FIB Thermo Scientific Scios2).

The coloration process was followed in real-time at the central point of the 3-inch diameter highly conductive (0.001 Ωcm) Si-wafer. Electrochemical measurements were performed in a liquid cell filled with a 1 M lithium perchlorate ($LiClO_4$)/propylene carbonate electrolyte, and a Pt wire counter electrode was placed into the electrolyte alongside a reference electrode. A controlled current was applied through the cell during a 4 min coloration. After the coloration process, the whole sample (in the dry state) was mapped by SE. The edges were under the Teflon cover (during the coloration process) so that only the central 6 cm diameter part was measured, as demonstrated in Figure 4-3.

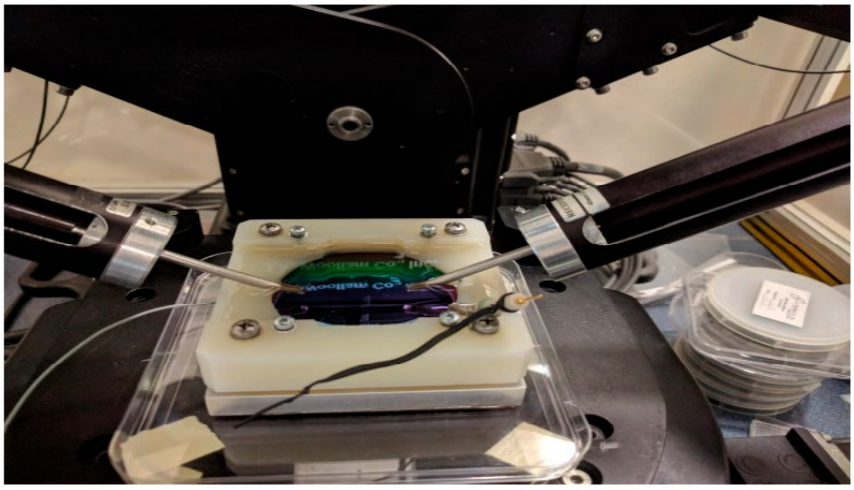

Figure 4-3 Combinatorial TiO_2-SnO_2 layer on highly conductive 3-inch Si-wafer in an electrochemical fluid cell during in situ, real-time SE measurements.

4.2.2 Results

The physical combination of the TiO_2 and SnO_2 in the mixed layers can be considered as a mixture of distinct phases or as an atomic-scale mixture. Our aim was to determine (point-by-point) the volume fraction of each constituent. If we consider it as a mixture of clear phases, then we should use the Bruggeman Effective Medium Approximation (BEMA) optical model [150]. The Lorentz model is a classical model where an electron is bound to an ionic core with a spring. If the light is shone, it will induce dielectric polarization. The Lorentz model assumes that the electron oscillates in a viscous fluid. As the mass of the electron is far less, the position of the ionic core is fixed. So, the Lorentz model (and its modified version, the Tauc–Lorentz oscillator model) considers each "molecule" as an individual damped oscillator [129]. The dielectric function of the mixed material can be considered as a summation of the elementary oscillators of the TiO_2 and SnO_2 "molecules". The Amplitude-ratio of the two elementary oscillators can be considered as the atomic ratio of the Ti and Sn atoms.

The optical model for the dry samples consisted of 3 layers: interface layer, TiO_2 + SnO_2 mixed layer, and surface roughness layer. The interface layer (between the Si-substrate and the mixed layer) proved less than 15 nm, while the surface roughness layer proved less than 5 nm. I used the measurements near the edges of the samples (pure component materials) to determine the fundamental parameters (band gap energies, the broadenings and the peak positions) for the two materials.

4.2.2.1 Comparison of the Optical Models

I applied the 2T–L and the BEMA optical model to evaluate the mapping measurements on the Si-stripes (shown in Table 4-1 and Figure 4-4) and the 4-inch Si-wafer (shown in Figure 4-5). Both modeling processes gave good results, as shown in Figure 4-4 where the measured Psi and Delta spectra are in good agreement with the Model calculations. The Mean Squared Error (MSE), is used to quantify the difference between curves, the model is better if the MSE values are significantly lower, because the lower MSE indicates a better fit and better optical model and it is significantly lower for the 2T–L model, especially around the 50–50% composition, as demonstrated in Figures (4-4c and 4-5) in the lower row. The calculated thickness values are not significantly different, as

evident in Table 4-1, Figures (4-4d and 4-5) in the middle row. The difference (less than 2%) in thickness values can be explained by the different optical models and does not change the conclusion.

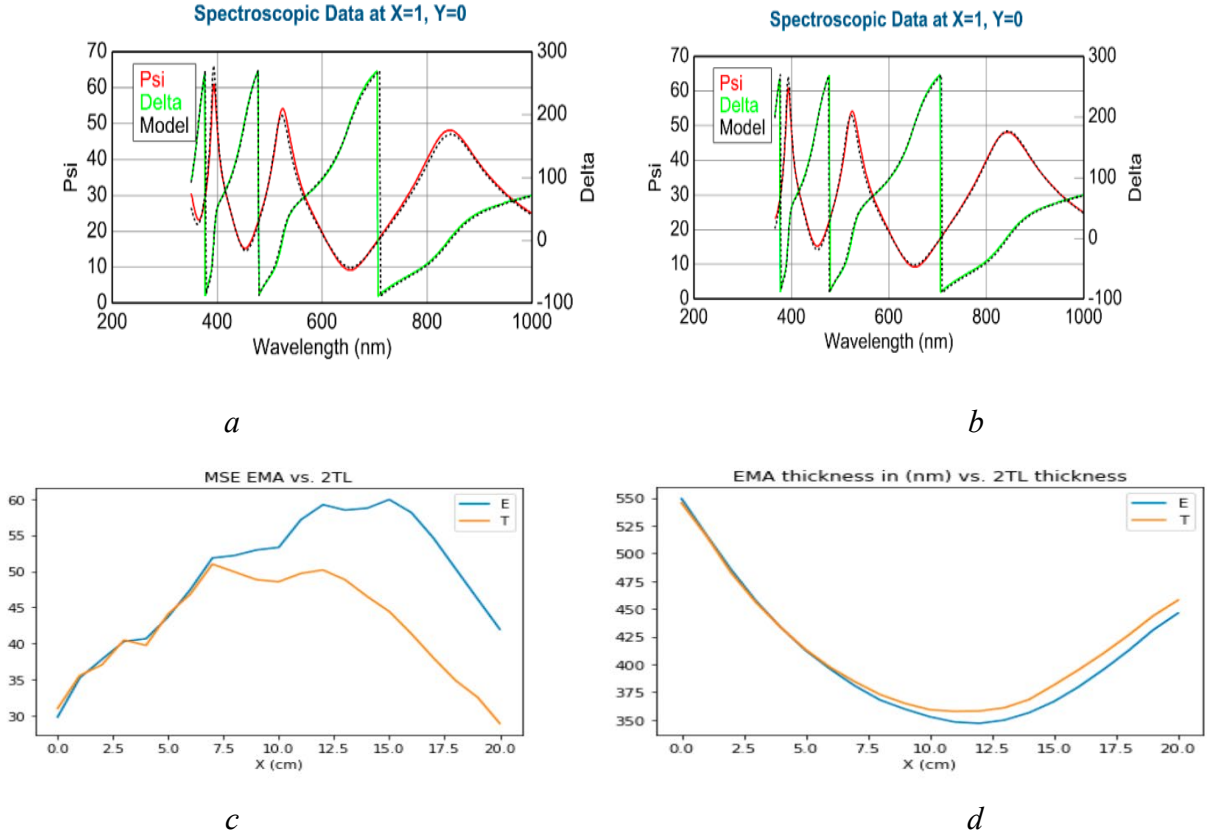

Figure 4-4 Comparison of (a) EMA; (b) 2T–L modelling (TiO_2-SnO_2); (c) MSE for EMA (the blue curve) vs. 2T–L (the orange curve), (d) is the thickness (EMA (the blue curve) vs. 2T–L (the orange curve) by home-made software version 1.0 coded in Python version 3.11 language.

Table 4-1: Mean Squared Error (MSE) and Thickness values from EMA and 2T–L modelling.

X (cm)	MSE from EMA	MSE from 2-TL	Thickness [nm] from EMA	Thickness [nm] from 2-TL
0	29.8	31.0	549.2	545.3
1	35.2	35.6	516.7	515.7
2	37.8	37.0	485.2	482.5
3	40.3	40.5	457.1	455.7
4	40.7	39.8	433.3	433.2
5	43.7	44.1	412.5	413.4
6	47.4	46.8	395.6	397.1
7	51.8	510	380.4	384.2
8	52.2	49.9	367.8	372.7
9	52.9	48.8	359.7	364.8
10	53.3	48.5	352.8	359.1
11	57.1	49.7	348.1	357.6
12	59.2	50.2	346.8	357.9
13	58.5	48.8	349.8	360.9
14	58.7	46.5	356.5	368.3
15	59.9	44.4	366.5	381.4
16	58.1	41.3	379.8	395.2
17	54.6	38.0	395.4	410.1
18	50.3	34.9	412.3	426.2
19	46.1	32.5	431.1	443.7
20	42.0	28.9	446.1	457.9

Figure 4-5 shows the mapping results of the 4-inch wafer, which shows similar results to the results on the Si-stripes. The values change only in the X-direction (where the samples were moved during the sputtering process, as shown in Figure 4-1), while the values do not change in the Y-direction. The EMA % (Figure 4-5 upper row left) shows the calculated volume fraction of the TiO_2 from the BEMA model, while Amp1 and Amp2 show the oscillator strengths of the TiO_2 and SnO_2 from the 2T–L calculations. One can see that the normalized amplitude values can be used as a good approximation for the composition at a given point of the sample.

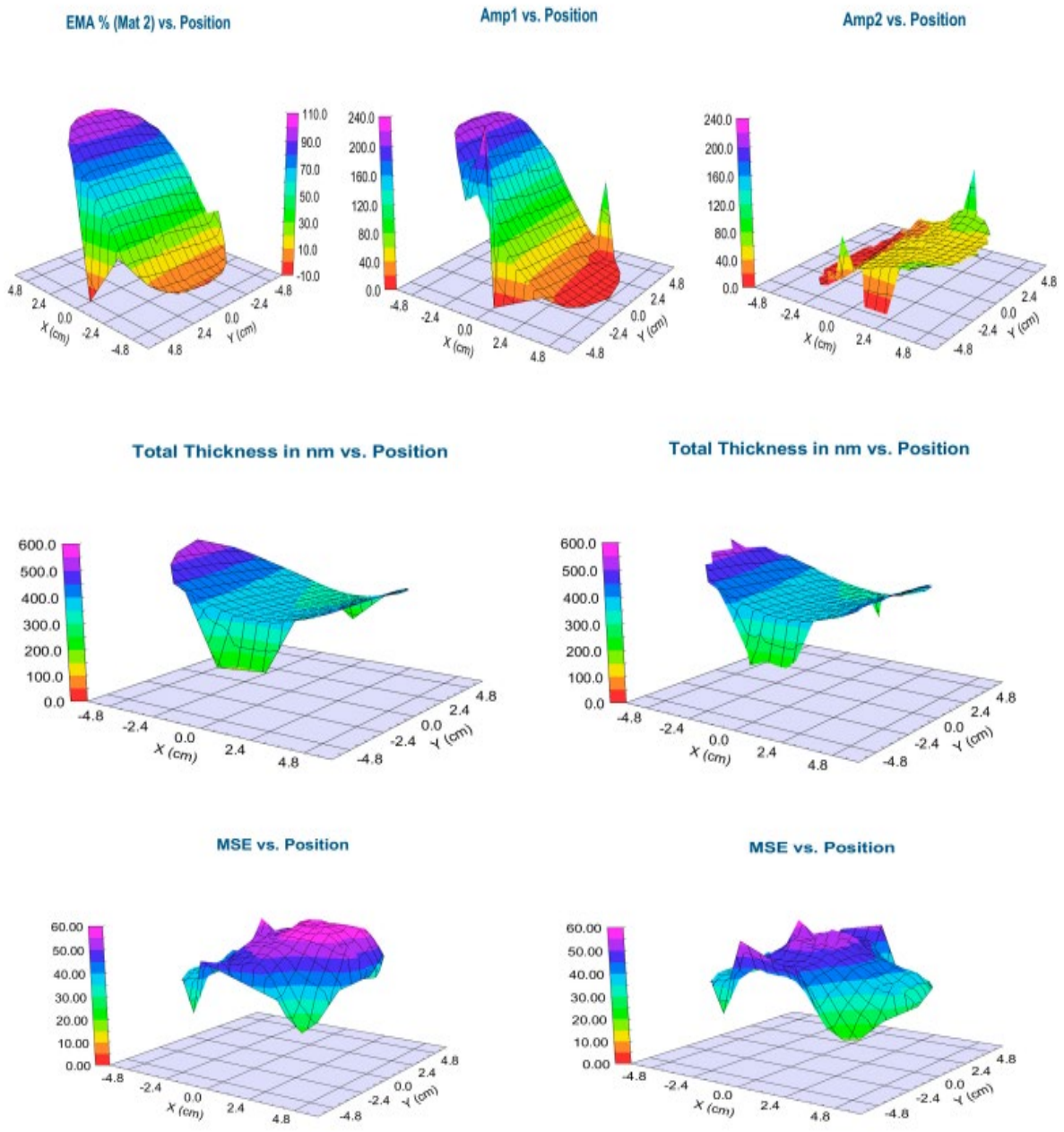

Figure 4-5 Shows TiO_2–SnO_2 maps from the 4 inch-wafer by BEMA modelling (left) 2T–L modelling (right), upper row: EMA% (left) and Tauc–Lorentz Amplitudes (right), middle row: total thickness maps, lower row: MSE maps (showing that the 2T–L model is better, the MSE values are lower). Pictures were made by the CompleteEASE v. 5.15 software.

I compared the EMA % values and the composition values calculated from the normalized amplitude values with the results of the SEM–EDS in Figure 4-6. The calculated thickness values are not significantly different, as demonstrated in the middle pictures in Figure 4-5.

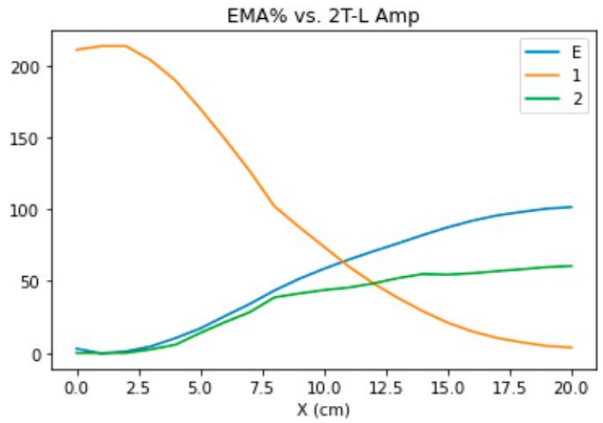

a

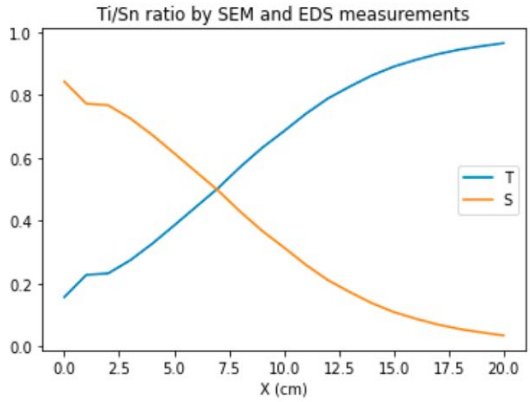

b

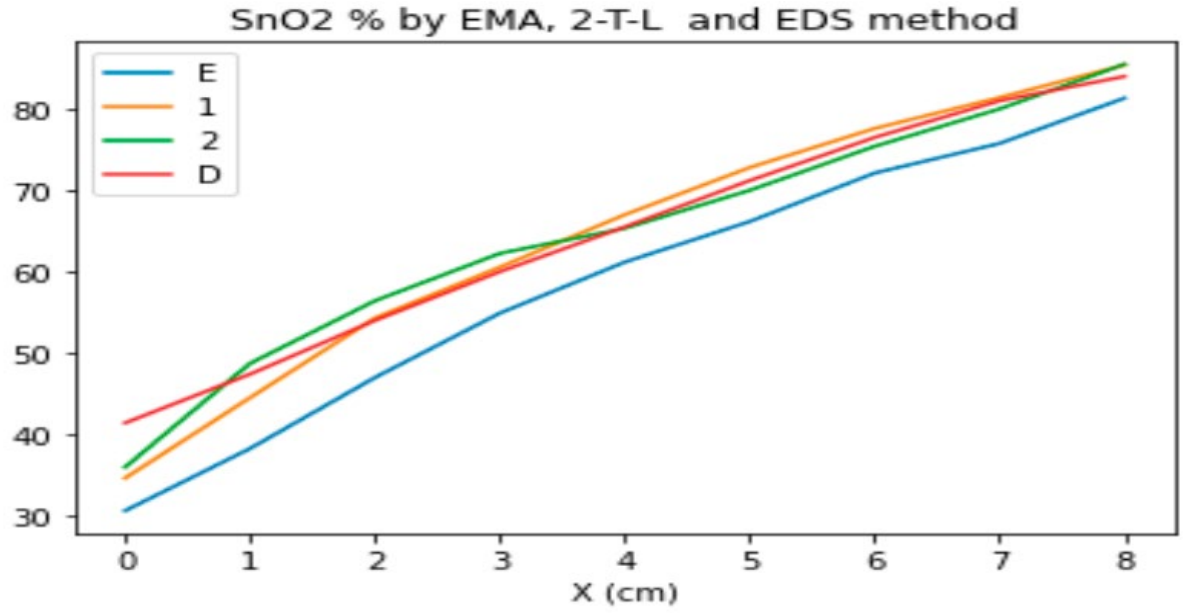

c

Figure 4-6 TiO_2–SnO_2 ratio curves from SE and SEM–EDS measurements at the center line of the 4-inch sample; (a) the blue curve for EMA% (E), the orange curve for Amp1 (TiO_2), the green curve for Amp2 (SnO_2); (b) Ti/Sn ratio from SEM–EDS measurements, (the blue curve for Ti ratio and the orange curve for Sn ratio); (c) SnO_2% derived from EMA% (the blue curve, E), 2T–L models (the orange curve for Amp1 and the green curve for Amp2), the red curve for EDS% measurements (by home-made software coded in Python language).

4.2.3 Discussion

I validated the results of the SE modeling with SEM–EDS measurements, as demonstrated in Figure 4-6b. Figure 4-6a shows the EMA% (MAT2-SnO_2%, blue line E) values from the BEMA model and the Amp1 (TiO_2 oscillator strength) and Amp2 (SnO_2 oscillator strength) from the 2-Tauc–Lorentz (2T–L) model. Figure 4-6c shows the results together, where I normalized the Amp1 and Amp2 to 100%. One can see the good agreement between the SEM–EDS and the 2T–L results.

4.2.3.1 Electrochromic Measurements

I performed an in situ electrochromic measurement by SE, shown in Figure 4-3. I could measure only at the central point of the highly conductive 3-inch Si-wafer. Figure 4-7 shows a typical example of one measured spectra pair with the model calculation based on the optical model shown on the right side. The low MSE value shows that the optical model is good. I could follow the process by calculating the change of the k parameter, as shown in Figure 4-8a and Table 4-2.

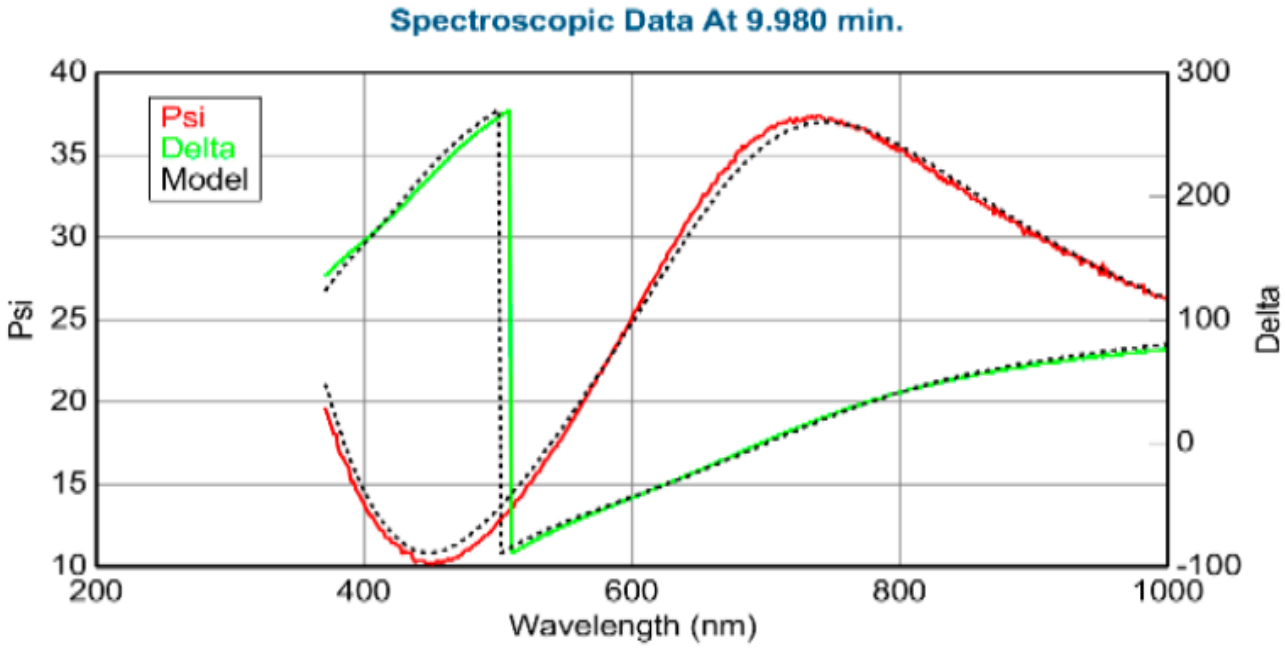

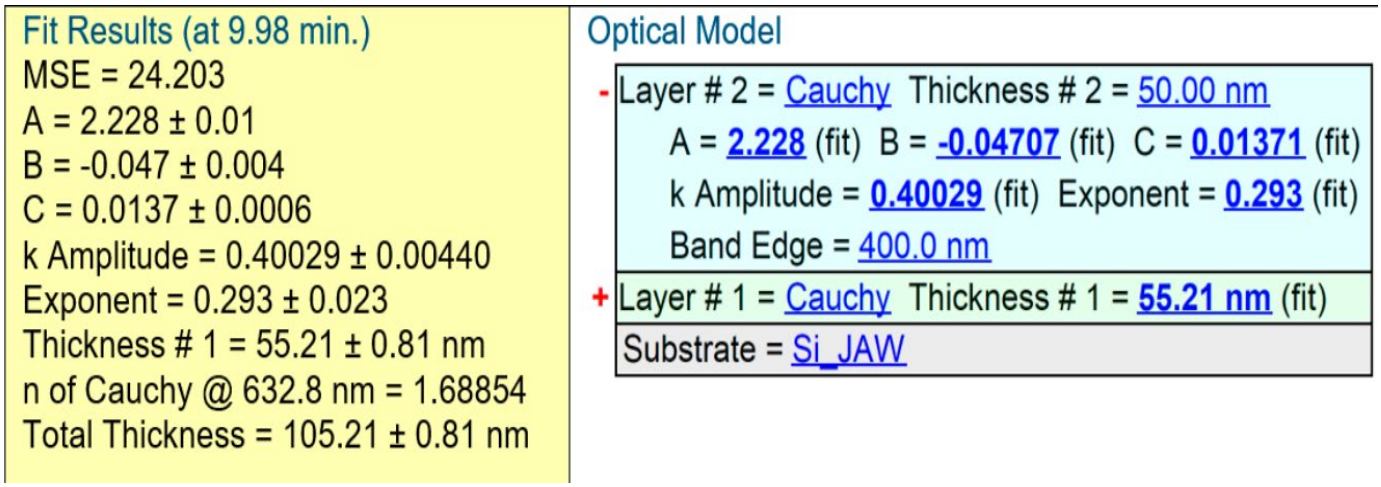

Figure 4-7 Typical example of a fitted SE spectrum for the details of the model structure; SE spectra were evaluated using a multi-layer, multi-parameter optical model applying two-layer Cauchydispersion. Pictures were made by the CompleteEASE v. 5.15 software.

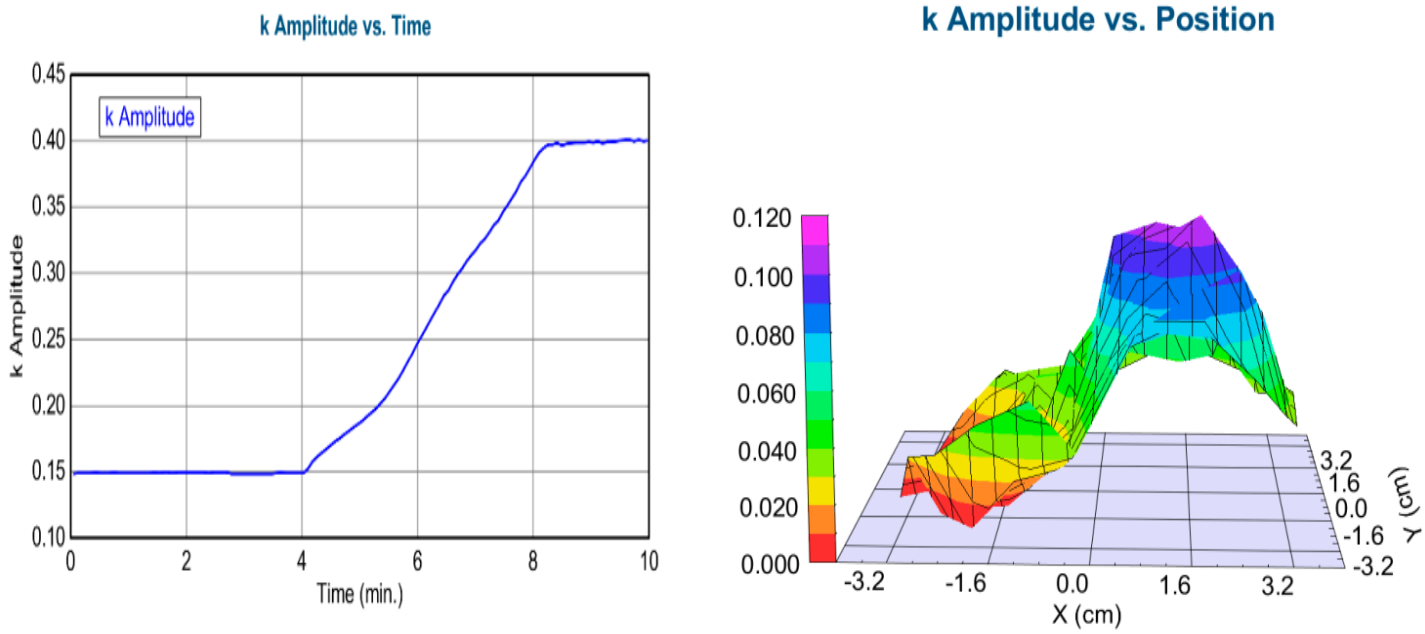

a *b*

Figure 4-8 (a) The imaginary part of the refractive index (k Amplitude) as a function of time for highly conductive Si in the liquid cell during coloration (time-scan, simple 2-layer Cauchy model). From 0–4 min, there is low absorption, however, from 4–8 min, there is a growing absorption; (b) Map of the k parameter after coloration (simple 1-layer Cauchy-model). Pictures were made by the CompleteEASE v. 5.15 software.

Table 4-2: Cauchy parameter k Amplitude vs. Time at the center point during the colorization process.

Time (s)	k Amplitude	k Amplitude Error
0	0.149	0.001
60	0.149	0.001
120	0.149	0.001
180	0.148	0.001
240	0.149	0.001
270	0.169	0.001
300	0.188	0.002
330	0.211	0.002
360	0.246	0.0025
390	0.288	0.003
420	0.317	0.003
450	0.346	0.0035
480	0.386	0.004
510	0.397	0.004
540	0.399	0.004
570	0.400	0.004
600	0.400	0.0045

After the coloration process, I could map the colorized layer using a simple one-layer Cauchy dispersion optical model. Note that this is not the same model as it was used in the in-situ measurement. I used the k Amplitude parameter of the Cauchy model as an indicator of electrochromic effectiveness (the change in the light absorption for the same electric charge), i.e., the higher the k, the more effective the light absorption at that composition for the same electric charge.

I see a maximum value (maximum light absorption) around 1 cm, as shown in Table 4-3. Comparing these results with Figure 4-6 shows that the optimal composition is at (30%)TiO_2–(70%)SnO_2.

Table 4-3: k Amplitude vs. Position at the center line after the colorization in the dry state.

X (cm)	k Amplitude (Error ± 0.005)
−3.5	0.0002
−3	0.0025
−2.5	0.044
−2	0.004
−1.5	0.015
−1	0.025
−0.5	0.056
0	0.041
0.5	0.092
1	0.105
1.5	0.075
2	0.054
2.5	0.079
3	0.041
3. 5	0.039

4.3 TiO_2- MoO_3

4.3.1 Materials and Methods

Ti and Mo targets were put separately from each other, and the ITO-covered glass and Si-probes on a glass substrate (30 × 30) cm were moved under the two separated targets (Ti and Mo) in a reactive Argon-Oxygen (Ar-O_2) gas mixture, same way in figure 3-2a.

Titanium-Molybdenum-Oxide layers were deposited onto Indium-Tin-Oxide (ITO) covered 100x25 mm size glass surfaces. Layer depositions were made by reactive sputtering in an (Ar + O_2) gas mixture at ~2 × 10^{-4} Pa base pressure and at ~10^{-1} Pa process pressure. The target - substrate working distance was 6 cm. 30 sccm/s Ar and 70 sccm/s O_2 volumetric flow rates were applied in the magnetron sputtering chamber. The plasma powers of the Ti and Mo metal targets were selected as (4200 and 1500) W respectively. Samples were moved back and forth at 25 cm/s of walking speed

between the Mo and Ti targets, and a mixed oxide film was deposited onto the ITO surface before-electrochromic-experiments, see Figure 4-9a. And figure 4-9b was after-electrochromic-experiments. 5 min cooling interruption was applied after every 50 walking cycles.

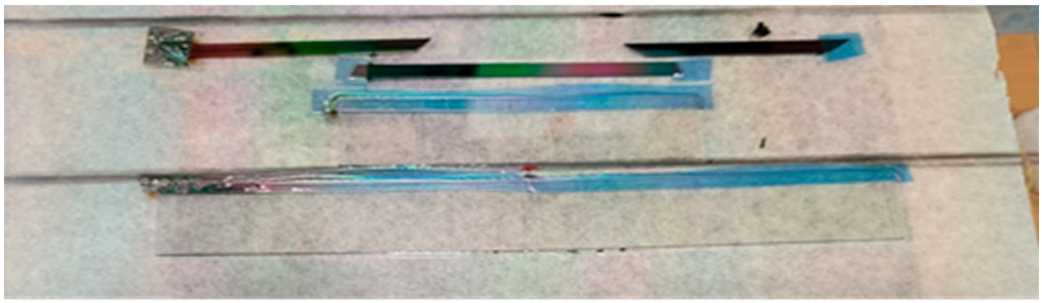

(a)

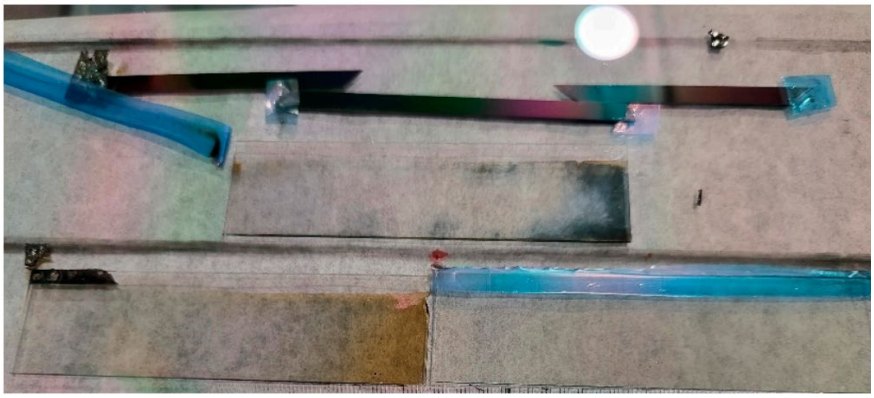

(b)

Figure 4-9 TiO_2-MoO_3 (a) ITO-covered glass and Si-probes on a glass substrate, before-electrochromic-experiments, the Ti in the left and the Mo in the right. (b) after-electrochromic-experiments.

Different optical models, such as EMA and 2T–L, have been used to achieve the composition map and thickness map of the sample layers. I used SE similar manner to determine the composition map and thickness map of our Ti-Mo combinatorial layers. The best determination of the optimal composition as a part of electrochromic (EC) properties, the layers were deposited onto ITO-covered glass. The composition map and thickness map were measured on the Si-probes, see Figure 4-9 a, b. I checked the resulted compositional map on the Si- probes Figure 4-9 b, c by using Scanning Electron Microscopy (SEM) with Energy-Dispersive X-ray Spectroscopy (EDS). Coloration Efficiency (CE) has been determined in a transmission electrochemical cell, see Figure 4-10. The

cell was filled with 1M lithium perchlorate ($LiClO_4$) / propylene carbonate electrolyte. A 5 mm width masked (Ti-Mo oxide-free) stripe of the slides remained above the liquid level allowing direct electric contact onto the ITO layer. A Pt wire counter electrode was placed into the electrolyte alongside with a reference electrode. This arrangement was a fully functional electrochromic cell. The applied current was controlled through the cell using a Farnell U2722 Source Measurement Unit (SMU). Constant current was registered through coloration and bleaching cycles of the electrochromic layer. Simultaneous spectral transmission measurements were performed by using the Woollam M2000 spectroscopic ellipsometer into transmission mode.

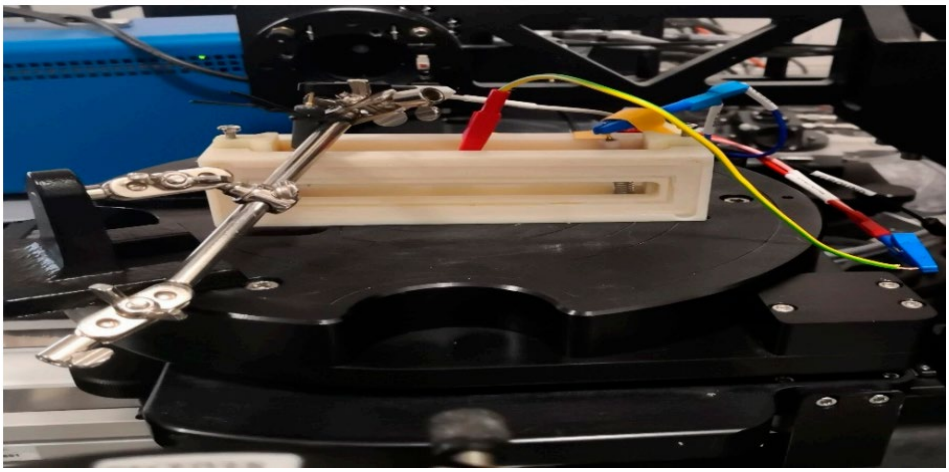

Figure 4-10 TiO_2-MoO_3 in a transmission electrochemical cell during-electrochromic-experiments by SE.

4.3.2 Results

The main criterion of the EC device performance is CE. Transmittance changes were directly measured during the coloration process, while the charge was calculated from the integral of the current vs. time data, and the electrolyte wet area of the sample. Figure 4-11 shows the calculated CE data as a function of MoO_3 fraction of the layer (individual color-coded curves represent different wavelengths), while Figure 4-12 is a 3D diagram of the data. Individual points were calculated from the average of three independent measurements. Error is estimated as 3 %, calculated based on the accuracy of sample positioning in the measuring cell and the spot size of the optical beam. The calculated data are given in Table 4-4 according to the equation (1).

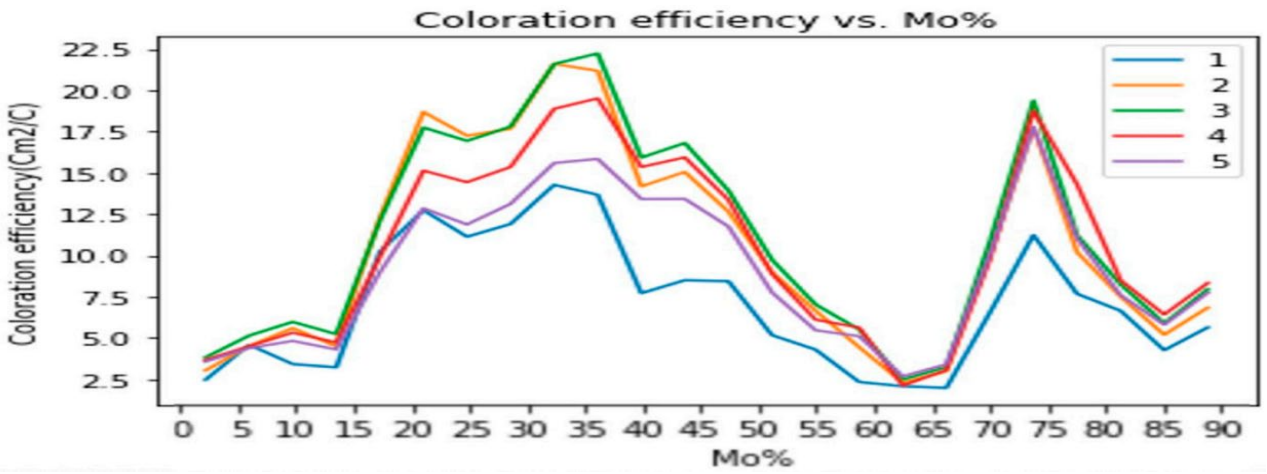

Figure 4-11 Coloration Efficiency of TiO_2-MoO_3. vs. Mo % for wavelengths from (400-800) nm by home-made software version 1.0 coded in Python version 3.11 language. (Individual color-coded curves represent different wavelengths: 1-400 nm, 2 -500 nm, 3-600 nm, 4-700 nm, 5-800 nm).

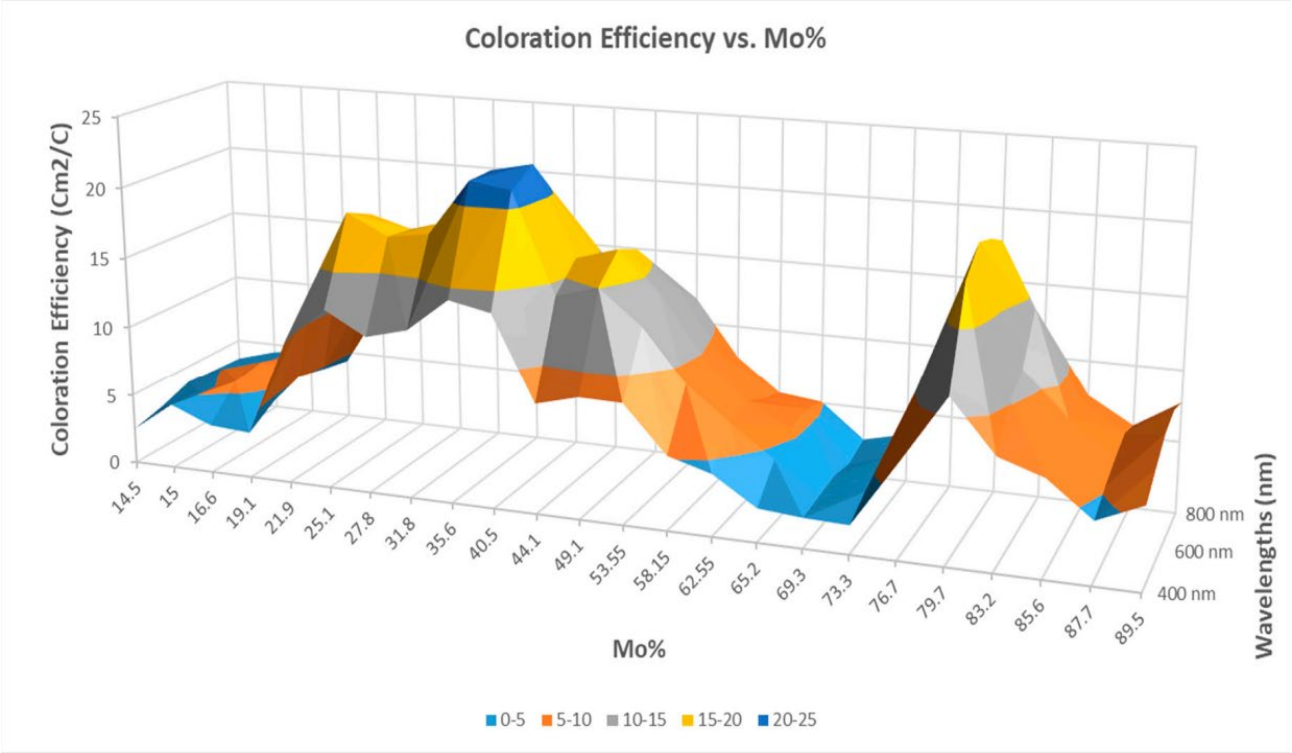

Figure 4-12 diagram of the Coloration Efficiency data of TiO_2-MoO_3. vs. Mo % for wavelengths from (400-800) nm visible spectral range.

Table 4-4: calculated data for the CE according to the wavelengths (400-800) nm.

X(cm)	Mo (%)	400 nm	500 nm	600 nm	700 nm	800 nm
2	14.5	2.4	3.04	3.8	3.6	3.5
2.5	15	4.5	4.5	5.1	4.5	4.3
3	16.6	3.4	5.6	5.9	5.3	4.8
3.5	19.1	3.2	4.4	5.2	4.7	4.3
4	21.9	10.2	12.2	12.1	9.8	8.9
4.5	25.1	12.7	18.6	17.7	15.1	12.8
5	27.8	11.1	17.2	16.9	14.4	11.8
5.5	31.8	11.9	17.6	17.7	15.3	13.1
6	35.6	14.2	21.5	21.5	18.8	15.5
6.5	40.5	13.6	21.1	22.2	19.5	15.8
6.9	44.1	7.7	14.1	15.9	15.3	13.4
7.4	49.1	8.5	15.05	16.8	15.9	13.4
7.9	53.55	8.4	12.6	13.9	13.3	11.7
8.4	58.15	5.1	9	9.7	8.8	7.7
8.9	62.55	4.3	6.6	7.03	6.1	5.4
9.3	65.2	2.3	4.4	5.5	5.6	5.1
9.8	69.3	2.08	2.2	2.4	2.1	2.6
10.3	73.3	1.9	2.9	3.2	3.05	3.4
10.8	76.7	6.5	9.9	10.8	9.7	10.04
11.3	79.7	11.3	17.7	19.3	18.7	17.7
11.8	83.2	7.6	10.2	11.2	14.3	11.01
12.3	85.6	6.6	7.5	8.2	8.4	7.5
12.8	87.7	4.2	5.2	5.9	6.4	5.8
13.3	89.5	5.6	6.8	7.9	8.3	7.7

Figures 4-13 and 4-14, showed SEM-photos from the Ti-rich side and Mo-rich side.

The precision of the Ti/Mo ratio is 2 %, while the precision of the position is 1 mm. see Figure 4-15.

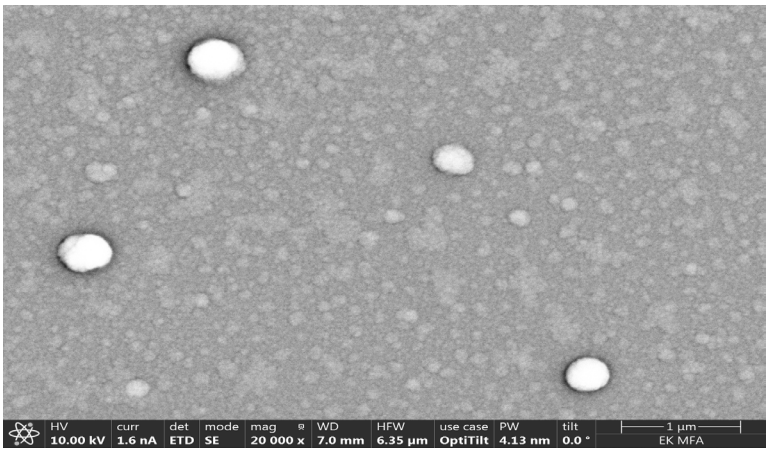

Figure 4-13 SEM micrograph from the TiO_2-MoO_3 surface Ti-rich side.

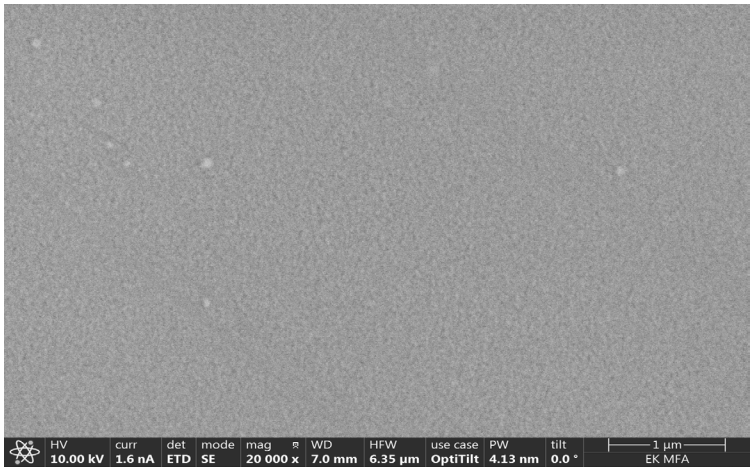

Figure 4-14 SEM micrograph from the TiO_2-MoO_3 surface Mo-rich side.

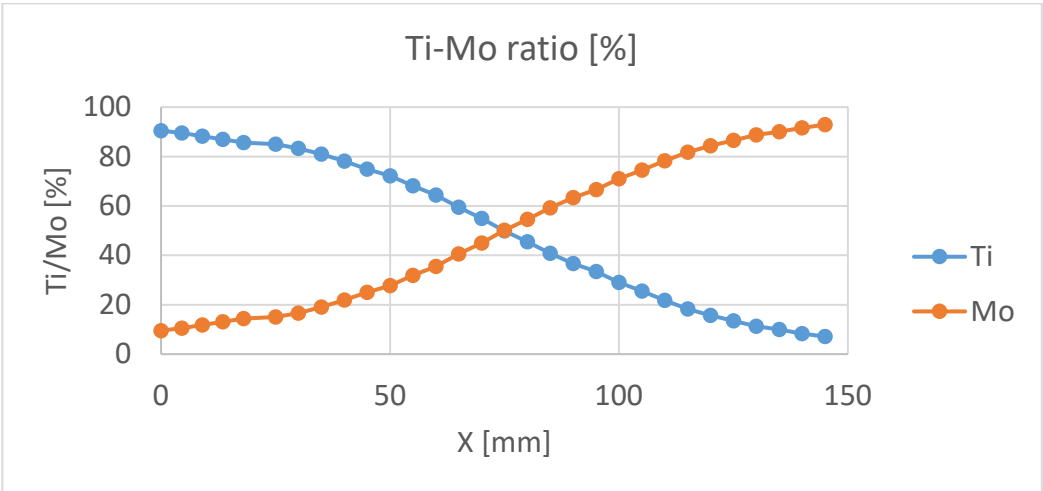

Figure 4-15 Ti/Mo ratio measured on the Si-probes by SEM-EDS.

4.3.3 Discussion

To check the position dependent composition, Scanning Electron Microscopy (SEM) with Energy-Dispersive X-ray Spectroscopy (EDS) has been used, see Figure 4-15. To explain the two maxima in CE (Figures 4-11 and 4-12) I show here SEM-images from the Ti-rich side and Mo-rich side, see Figures 4-13 and 4-14. These are the proof that the material at the Ti-side is polycrystalline (several hundred nm) and the Mo-side is amorphous or nanocrystalline. I think that the Ti-rich side was at significantly (several hundred C degree) higher temperature (plasma power 4.2 kW) during the deposition process, so the Ti-rich oxide is polycrystalline (several hundred nm grainsize) compared to the Mo-rich side where the oxide remains amorphous or nanocrystalline. This is the reason for microstructure difference between the two peaks in Figures 4-11 and 4-12 of the CE curves.

CE values were determined at every composition from the measured relative transmission vs. input charge curves. I used Eq. 1 to determine CE at 5 wavelengths (400-800 nm visible range) for every compositional position using the relative transmission curves and fitted exponential curves. The determined results, CE vs. composition vs. wavelength are shown in Figures 4-11 and 4-12.

4.4 SnO_2-ZnO

4.4.1 Materials and Methods

The optimal composition of reactive magnetron-sputtered combinatorial mixed layers of tin oxide and zinc oxide (Sn_x-Zn_{1-x}) was determined (where $0 < x < 1$) for electrochromic purposes. Metallic Sn and Zn targets were placed separately from each other, and indium-tin-oxide (ITO)-covered glass and Si-probes on a glass substrate (30 cm × 30 cm) were moved under the two separated targets (Sn and Zn) in a reactive argon–oxygen (Ar-O_2) gas mixture (see Figure 4-16a). The tin-zinc oxide layers were deposited onto ITO-covered 100 × 25 mm glass surfaces. Layer depositions were carried out by reactive sputtering in an (Ar + O_2) gas mixture at a ~2×10^{-4} Pa base pressure and at a ~10^{-1} Pa process pressure. The target substrate working distance was 6 cm. Volumetric flow rates of 30 sccm/s Ar and 70 sccm/s O_2 were applied in the magnetron sputtering chamber. The plasma powers of the Sn and Zn metal targets were set to 800 and 1000 W, respectively. The samples were moved back and forth at a 25 cm/s walking speed between the Sn and Zn targets, and a mixed oxide film was deposited onto the ITO surface (see Figure 4-16b). A 5 min cooling interruption was applied after every 50 walking cycles.

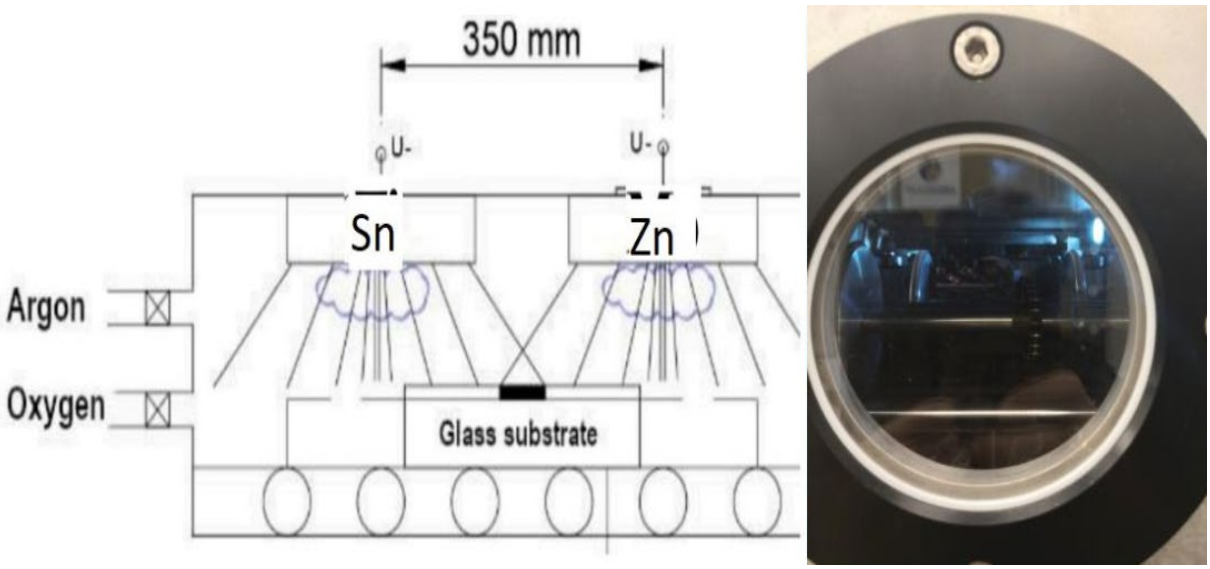

a

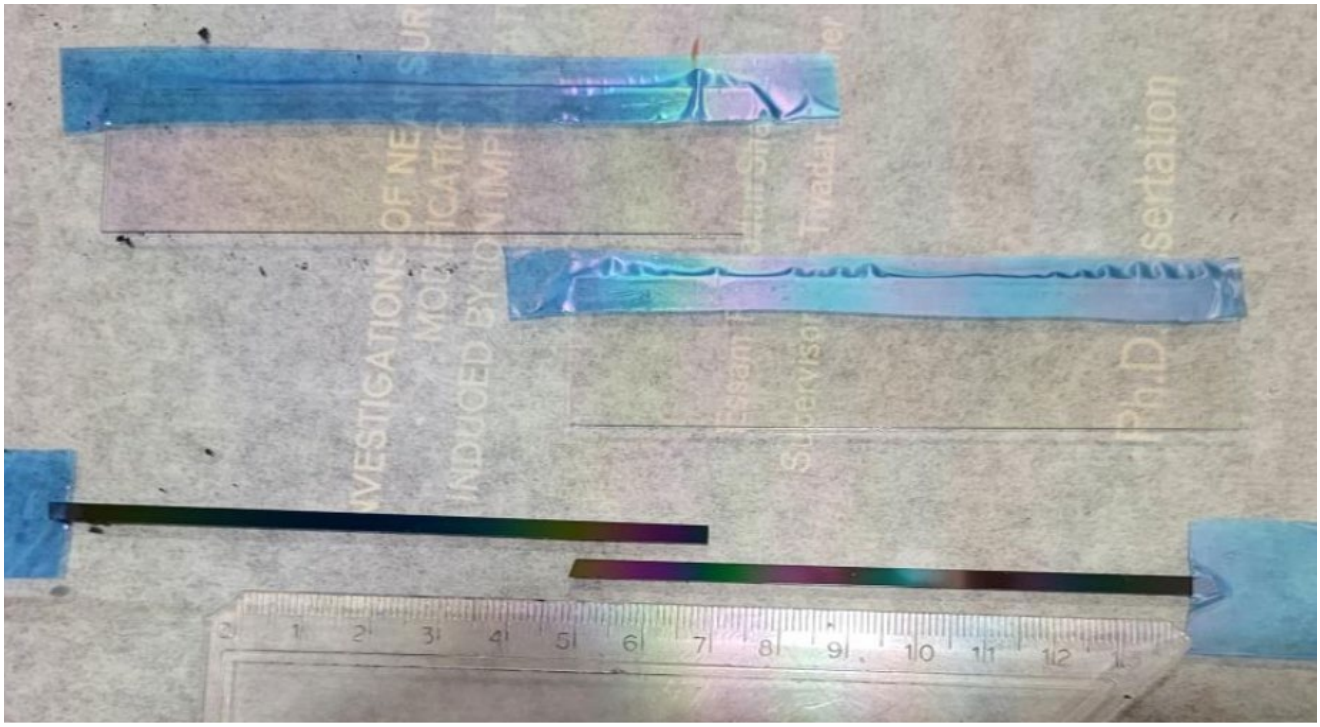

b

Figure 4-16 The SnO_2-ZnO (a) arrangements of the two targets (at a 35 cm distance from each other) and the chamber for the DC magnetron sputtering after being vacuumed; the blue light is from the Ar-O_2 plasma. (b) ITO-covered glass and Si-probes on a glass substrate before the electrochromic experiments; the Sn on the left and the Zn on the right.

X-ray Diffraction (XRD) measurements were performed, and we checked the resulting compositional map for the Si-probes using an SCIOS2 Scanning Electron Microscope (SEM) (Thermo Fisher Scientific, Waltham, MA, USA) with Energy-Dispersive X-ray Spectroscopy (EDS), X-ray Diffraction (XRD) measurements were performed on a Bruker AXS D8 Discover device (Billerica, MA, USA) to investigate the microstructure of the layers. to investigate the microstructure of the layers. We examined the Si-probes and show three characteristic diffractograms, one from the Sn-side, one from the "mixed-part" and one from the Zn-side and found that the Sn-side and the mixed-part layers are amorphous, but the Zn-side is a mixture of amorphous and nanocrystalline (with crystallites of less than 10 nm in size). Examples of the XRD measurements are shown in Figure 4-17.

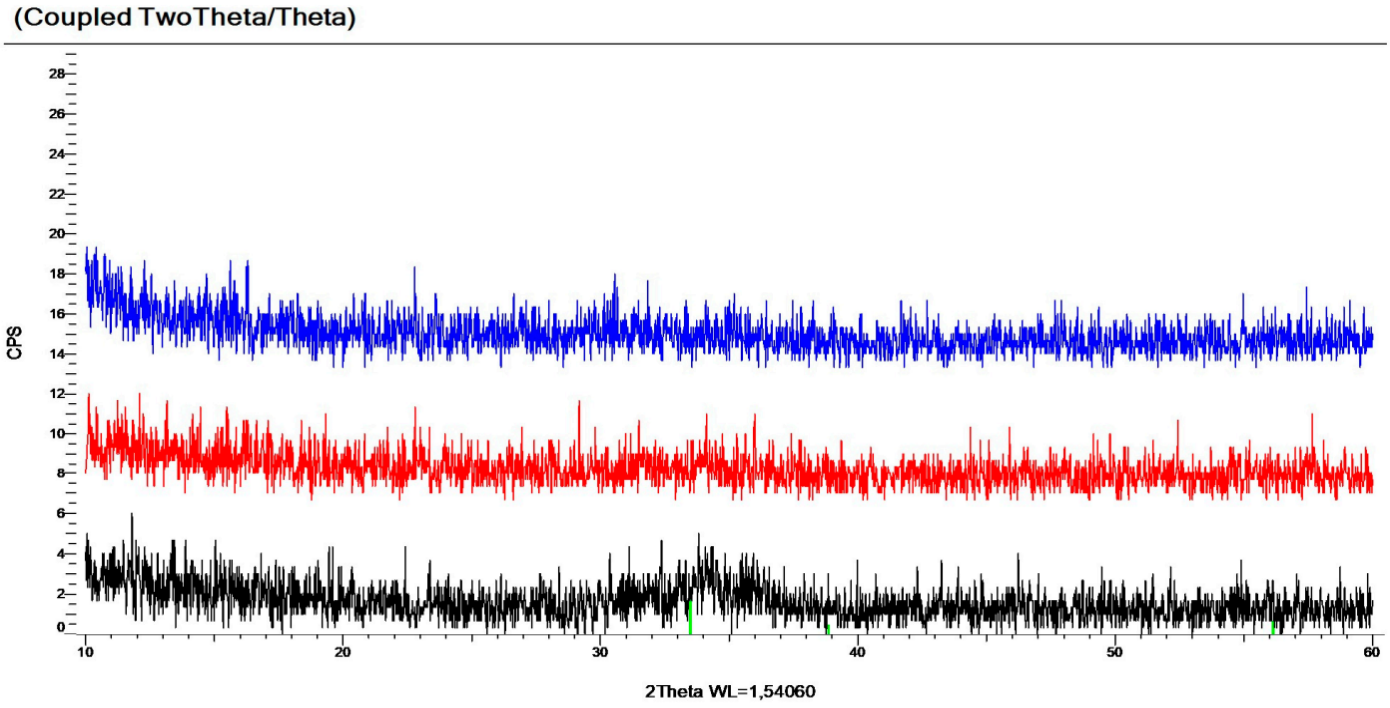

Figure 4-17 Examples of XRD measurements: one from the Sn-side (upper), one from the mixed part (middle) and one from the Zn-side (lower). One can see only small and wide peaks (between 33 and 37 deg) in the lower diffractogram showing a trace of small ZnO nanocrystallites (with a less than 10 nm diameter).

Different optical models, such as Effective Medium Approximation (EMA) and 2-Tauc-Lorentz Oscillator (2T–L), have been used to achieve a composition map and a thickness map of the sample layers. I used SE in a similar manner to produce a composition map and a thickness map of our Sn-Zn combinatorial layers. To determine the optimal composition for the best CE value, the layers were

deposited onto ITO-covered glass. The composition map and thickness map were measured for the Si-probes (see Figure 4-16b). I checked the SE result of compositional map for the Si-probes by using an SCIOS2 Scanning Electron Microscope (SEM) (Thermo Fisher Scientific, Waltham, MA, USA) with Energy-Dispersive X-ray Spectroscopy (EDS) (see Figure 4-18) Zn-rich side: upper part, app. 50–50% is in the middle, Sn-rich side is below.

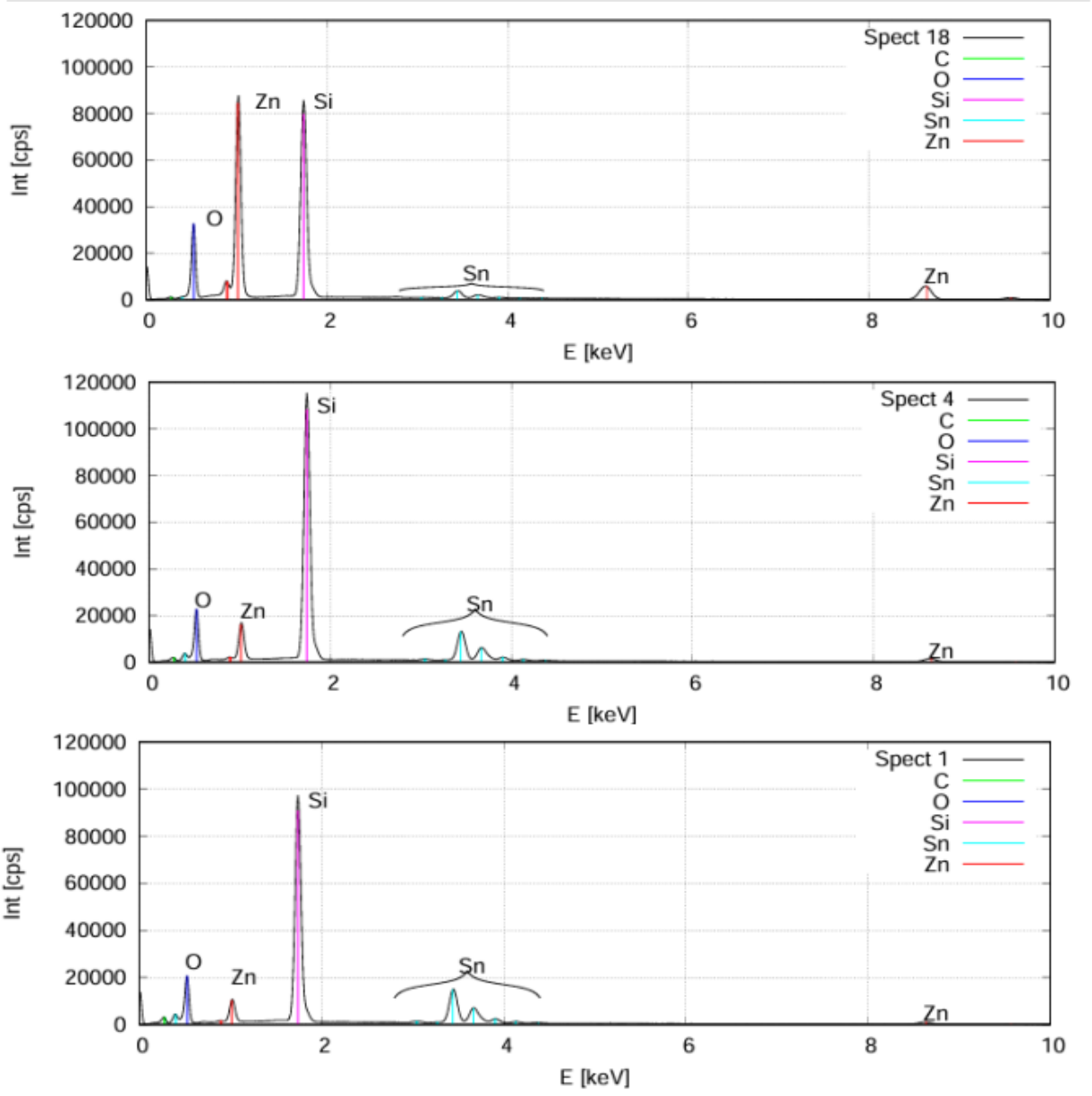

Figure 4-18 SEM-EDS spectra from the Si-probes: Zn-rich side (upper), app. 50–50% (middle), Sn-rich side (below).

Figure 4-19 presents the comparison of the SEM and EDS measurements and shows a good match between them; in this figure I measured only 10 cm from the sample in figure 4-16 b. The CE η is given by equation (1).

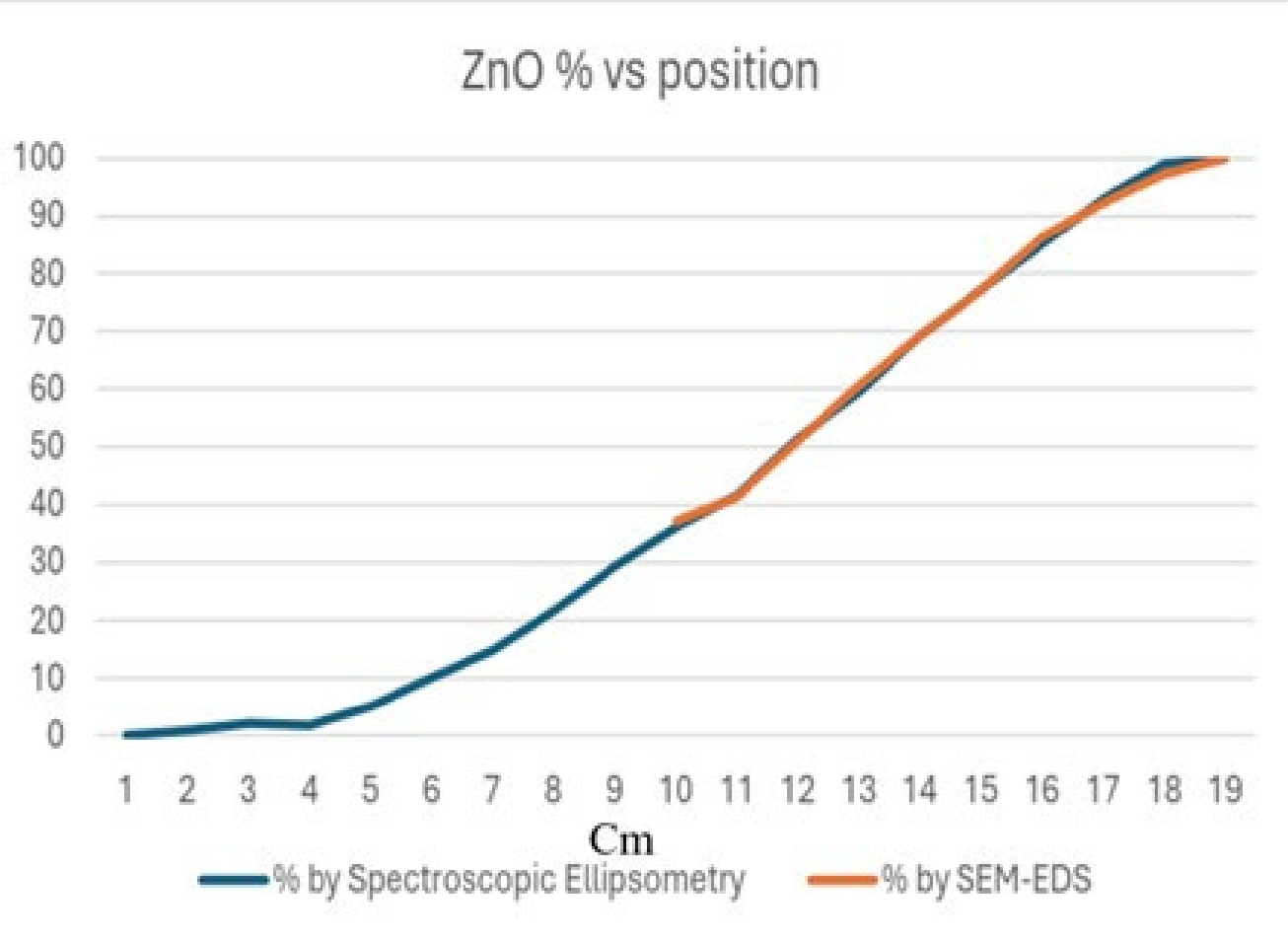

Figure 4-19 ZnO ratio measured on Si-probes and comparison of SE and SEM-EDS results.

The CE was determined in a transmission electrochemical cell (see Figure 4-10). The cell was filled with 1 M lithium perchlorate ($LiClO_4$)/propylene carbonate electrolyte. A 5 mm width masked (Sn-Zn oxide-free) ITO strip of the slides remained above the liquid level, allowing direct electric contact with the cell. A Pt wire counter electrode was placed into the electrolyte alongside a reference electrode. This arrangement was a fully functional electrochromic cell. The applied current was controlled through the cell using a Farnell U2722 Source Measurement Unit (SMU) (Leeds, UK). A constant current was applied through coloration and bleaching cycles of the electrochromic layer, and

simultaneous spectral transmission measurements were performed by using a Woollam M2000 spectroscopic ellipsometer (Tokyo, Japan) in transmission mode.

The precision of the Sn/Zn ratio was 2%, while the precision of the position was 1 mm. Electrochemical measurements were carried out in a three-electrode cell arrangement where the potential was measured against the Ag/AgCl-KCl (3M) reference electrode. Samples of SnO_2/ZnO mixed oxide films deposited onto ITO substrates were used as the working electrodes and were immersed into a solution of 0.1 M $LiClO_4$ in propylene carbonate solvent. A platinum coil electrode was used as a reference. Cyclic voltammetry (CV) characterization was carried out using a Bio-Logic SP-50e potentiostat (Bio Logic Systems Corp, Orlando, FL, USA) on a 1 × 1 cm sample with an oxide composition of $SnO_{2(0.3)}$ - $ZnO_{(0.7)}$ (i.e., at maximum coloration efficiency).

4.4.2 Results

The main criterion for assessing EC device performance is the CE. Transmittance changes were measured in the straight-through direction during the coloration process, while the charge was calculated from the integral of the current vs. time data and the electrolyte-wetted area of the sample. Figure 4-20a shows an example normalized-intensity spectrum in the bleached state (the measured intensity divided by the intensity without the sample) of one sample point. One can see that below 400 nm (in the UV region), the layer is not fully transparent (the band gap energy of SnO_2 is 3.6 eV (344 nm) and of ZnO is 3.3 eV (375 nm)). The behavior of electrochromic materials is interesting in the visible region. Figure 4-20b shows curves of intensity versus time at five different wavelengths.

Figure 4-21a shows the calculated CE data as a function of the ZnO fraction of the film (different colors represent different wavelengths), while Figure 4-21b is a 3D representation of the same data. Individual points were calculated from the average of three independent measurements. The error is estimated to be 3%, calculated based on the accuracy of sample positioning in the measuring cell and the spot size of the optical beam. The calculated CE data in Figure 4-21a and data values are given in Table 4-5 according to Equation (1).

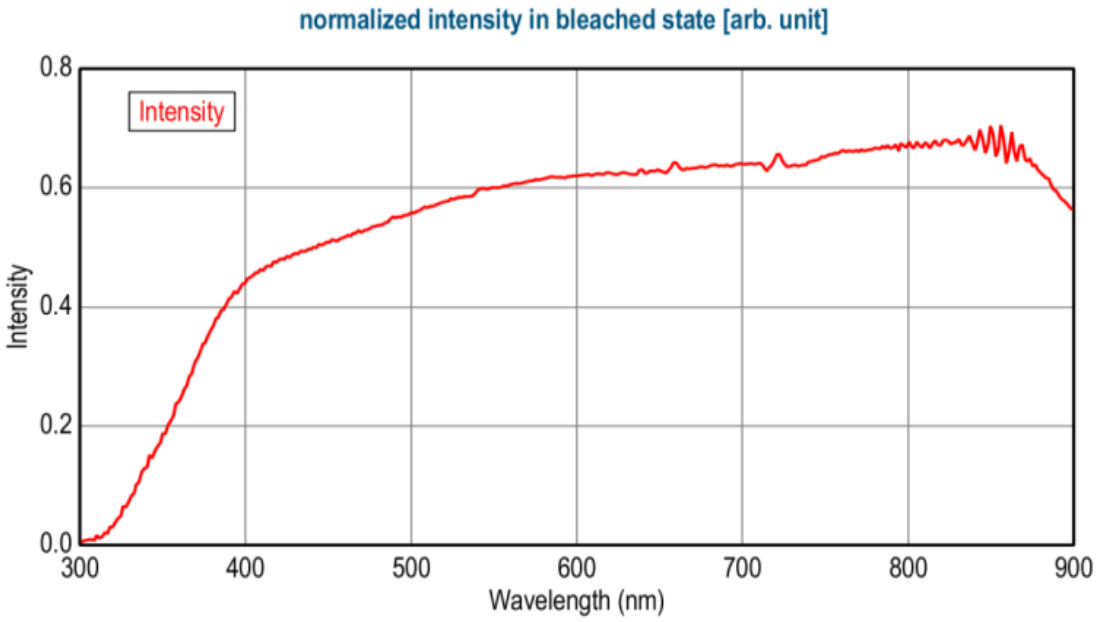

a

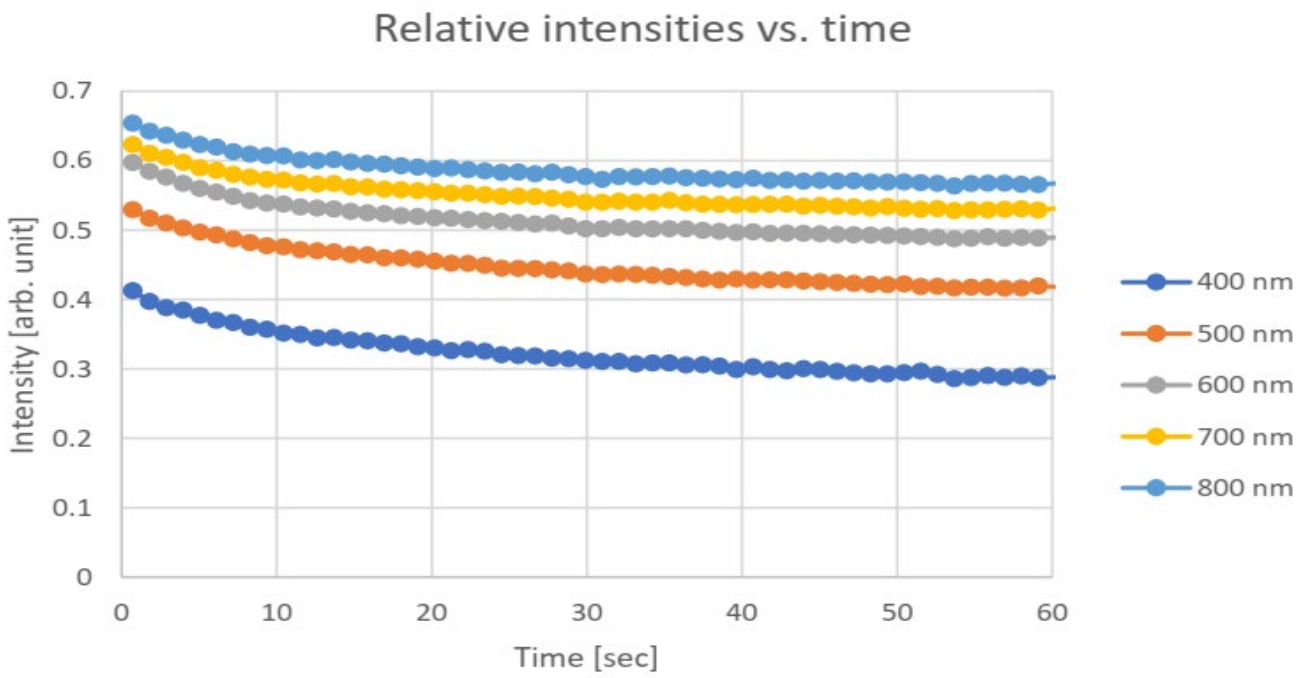

b

Figure 4-20 (a) Example normalized-intensity spectrum in bleached state (measured intensity divided by intensity without sample) of one sample point. (b) Curves of intensity versus time at five different wavelengths.

Table 4-5: Calculated data for CE according to wavelengths of 400–800 nm. The unit of CE is cm^2/C (square centimeters per Coulomb).

ZnO (%)	350 nm	400 nm	500 nm	600 nm	700 nm	800 nm
2	19.4	17.2	7.9	5.1	2.9	1.8
5	14.1	15.7	4.4	2.7	1.9	1.3
10	7.3	10.5	5.0	3.5	3.0	3.1
15	11.2	6.4	3.7	1.3	0.4	0.5
21.6	33.6	22.0	13.8	9.3	6.4	5.8
29.3	52.8	46.1	32.5	30.0	23.7	21.5
36.2	39.2	28.3	19.5	14.6	12.5	10.1
41.6	35.4	18.9	11.6	7.7	5.2	3.9
51.4	48.2	27.3	14.6	10.3	7.8	6.0
59.5	47.7	25.9	11.9	9.2	6.9	5.6
69	42.5	16.4	9.7	7.3	6.6	4.6
77	29.4	15.7	11.5	9.1	7.6	5.5
85	26.3	10.0	5.7	4.8	5.1	3.1
93	33.7	4.1	0.6	1.3	1.2	1.2
99	25.9	6.8	4.0	2.8	3.2	1.4
100	21.4	6.5	3.3	1.0	2.6	1.6

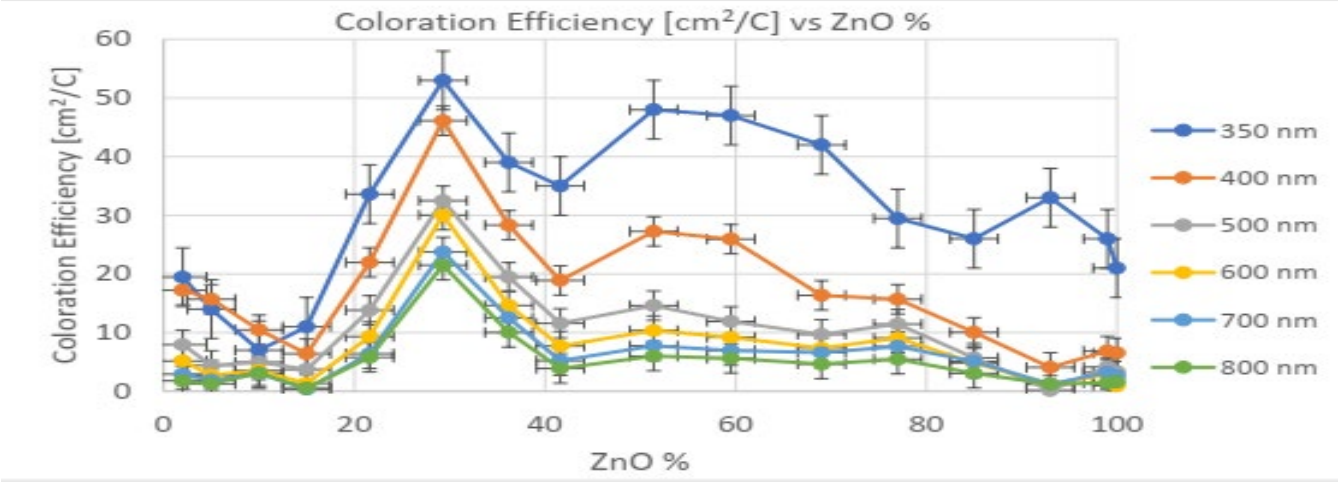

a

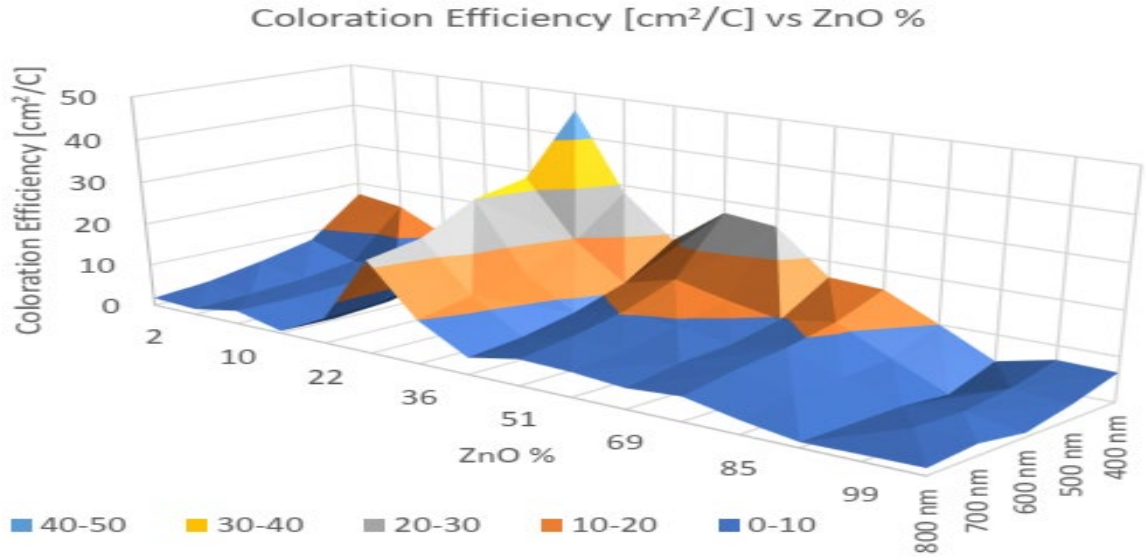

b

Figure 4-21 (a) CE of SnO_2-ZnO vs. Zn % for wavelengths from 350 to 800 nm (individual color-coded curves represent different wavelengths: 1–350 nm, 2–400 nm, 3–500 nm, 4–600 nm, 5–700 nm 6–800 nm. (b) Three-dimensional diagram of CE data of SnO_2-ZnO vs. Zn % for wavelengths from 400 to 800 nm in visible spectral range.

A selection of the typical patterns of stable Cyclic Voltammetry (CV) (after several scans) is shown in Figure 4-22 using five different scanning rates (5, 10, 25, 50 and 100 mV/sec). The CV patterns show run-to-run stability after 2–3 scans and remain reproducible up to10 scans.

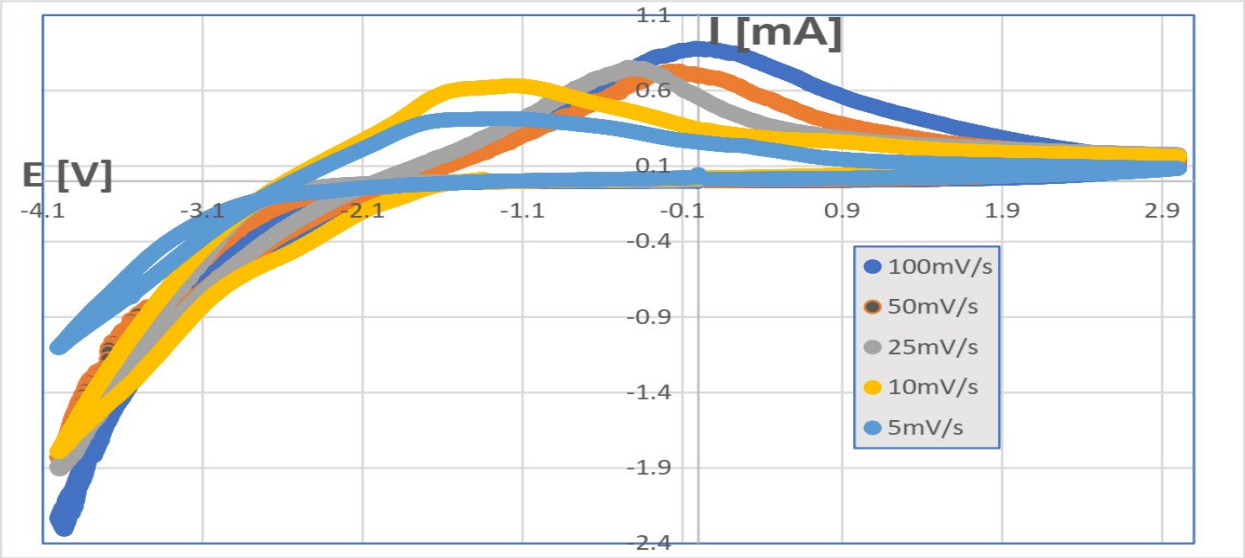

Figure 4-22 Cyclic voltammograms as a function of scanning rate taken on $SnO_{2(0.3)}ZnO_{(0.7)}$ oxide film in 1M $LiClO_4$ propylene carbonate electrolyte.

The cathodic current follows a rising pattern, and a clear anodic peak is observable in all cases. It is important to note that an increased scan rate causes a twofold effect:

(a) the observed anodic peak shifts towards negative values as the scan rate is decreased.

(b) the anodic peak becomes more pronounced as the scan rate increases. Lower-scan-rate CV curves tend to form a symmetrical CV shape.

4.4.3 Discussion

The CE maximum was found to be 29% Zn for each wavelength between 20 and 50 cm^2/C. This 29% is very close to the optimum value of 30% in the case of the TiO_2-SnO_2 mixture which was investigated in our earlier paper [58]. We expected that mixing metal atoms with different diameters in the layers can enhance the CE. This (70–30) % mixture of different metal oxides seems to be the optimum for Li-diffusion in these sputtered materials. Since our $SnO_{2(0.3)}$-$ZnO_{(0.7)}$ film exhibits an analogous pattern, the anodic peaks in Figure 4-22 can be interpreted as a result of the series resistance effect. The influence of mixing metal atoms with different diameters in the layers on EC behavior can be attributed to several factors. Mixing can create new pathways for charging carriers, enhancing the overall electrical conductivity. This increased conductivity can support faster ion intercalation and deintercalation processes, causing quicker color changes. Mixing can alter the electronic structure of the layer, affecting the way it absorbs and transmits light. These factors can explain the enhanced CE values.

5 Summary and Conclusions

Application of mixed metal oxides in electrochromic devices is a promising technology for energy saving and economic sustainability and it is considered environment friendly and scalable for industrial production. It can contribute to the reduction of the extra heat absorption of buildings by applying smart windows. These material are considered non-toxic so we can use them safely and easily in our daily life without any side effect. The mixed oxide materials reported in this work represent a room for development (and even commercialization) in the segment of oxide-based EC device market. Provided that the proper optimized composition is determined by preliminary studies, the further scale-up does not need fundamental changes in technology. For example, a reactive sputtering deposition process of WO_3 layers can be adapted into an amorphous WO_3 (40%)-MoO_3 (60%) mixed oxide deposition by applying a proper alloy target. Better comprehension and enhanced preparation of mixed-metal oxides would provide better opportunities for economically feasible mass-production. The potential economic impact of developing thin films of selected properties depends on the capabilities of the preparation of highly accurate test samples to locate compositions of optimal properties. The ideal compositions determined by combinatorial samples can in turn be used in industrial applications. The transition of production of these materials to the industrial scale can enhance productivity and efficiency.

We could optimize the electrochromic properties of mixed titanium oxide and tin oxide layer deposited by reactive sputtering. I prepared combinatorial samples by magnetron sputtering. These samples were mapped (composition and thickness maps) via spectroscopic ellipsometry, which is a rapid, cost-effective, and contactless (non-destructive) method. The selection between the suitable optical models [the Bruggeman Effective Medium Approximation (BEMA) vs. the 2-Tauc–Lorentz multiple oscillator model (2T–L)] was conducted according to the process parameters. I have shown that in the case of molecular-level mixed layers, 2T–L is better than the BEMA optical models. I have shown that the optimal composition is at (30%) TiO_2– (70%) SnO_2.

We could enhance the coloration efficiency of mixed Titanium oxide and Molybdenum oxide (TiO_2-MoO_3) layer deposited by reactive magnetron sputtering. I prepared combinatorial samples by moving the samples under the Ti and Mo sputtering targets in a reactive Argon-Oxygen (Ar-O_2) gas mixture. Since the Ti-rich side was at significantly higher temperature during the deposition process, so the Ti- rich oxide is polycrystalline compared to the Mo-rich side where the oxide remains

amorphous or nanocrystalline. Coloration Efficiency has been considered an important parameter in this study. The maximum value of the CE is 22.2 cm^2 C^{-1} at the wavelength 600 nm at ~ 60% - 40 % Ti-Mo ratio on the Ti-rich polycrystalline material, while CE is 19.8 cm^2 C^{-1} at the wavelength 600 nm at ~ 20% - 80 % Ti-Mo ratio on the Mo-rich amorphous (or nanocrystalline) material.

I optimized the CE of a mixed tin oxide and Zn oxide (SnO_2-ZnO) film deposited by reactive magnetron sputtering. I applied, for the first time, a combinatorial approach for composition graded layer deposition to allow the study samples to be chosen from a full and continuous $SnO_{2(x)}$ - $ZnO_{(1-x)}$ composition range. The maximum value of the CE was between 46 and 21 cm^2/C between wavelengths of 400 and 800 nm at a ~71–29% Sn-Zn ratio. In the future, we need to optimize the optical modulation, the reversibility and the cycling stability with minimal performance degradation.

The mixed metal oxides showed at least 3 times better EC properties than the pure oxides, due to possible electron transitions between two sets of electrons the EC effect can be more obvious in mixed oxides because of the electrochromic Effectiveness, can be higher in mixed metal-oxide layers and mixing metal atoms with different diameters in the layers can enhance the CE.

Better understanding and enhanced preparation methods of mixed-metal oxides design would provide better marketing and increase business potential for this field of study. The potential economic impact of developing more selective thin films depends on how we could present high accuracy samples. Then it will have a long-lasting work effect on electrochromic materials with a high chance of being desirable for marketing, because of the variety of its applications.

6 Thesises and supporting publications

1. I developed a new method for preparing combinatorial binary oxide samples in the full composition range. The mixed oxides are deposited by reactive magnetron sputtering, and every binary composition is present on the same sample. The composition-graded layer is prepared by moving the samples under sputtering targets in a reactive Argon-Oxygen (Ar-O_2) gas mixture. The deposition method allows the determination of the optimal compositions for electrochromic application [T2, T3]

2. Using the method described in (1) in the (TiO_2–SnO_2) binary system I proved that [T1]:
a., the optimal composition for CE is (30%) TiO_2 - (70%) SnO_2 (with ±2,5% error).

b., using an electrochemical cell combined with Spectroscopic Ellipsometry, I mapped the thickness and composition of TiO_2-SnO_2 mixed oxide samples, and I compared the application of two optical models [Bruggeman Effective Medium Approximation (BEMA) vs. 2-Tauc–Lorentz multiple oscillator model (2T–L)]. I proved that the 2T–L in the case of molecular-level mixed layers, 2T–L model is better than the BEMA since I found that the Mean Square Error (MSE) values are significantly lower in the (TiO_2-SnO_2) binary system.

3. Using the method described in (1) in the (TiO_2-MoO_3) binary system I proved that [T2, T3]

a., since the Ti-rich side was at significantly higher temperature during the deposition the Ti- rich oxide was polycrystalline while on the Mo-rich side the oxide remained amorphous or nanocrystalline. Due to the morphology difference two distinct optimal values of CE exists in this binary system:

b., the first optimal composition for CE in the (TiO_2-MoO_3) binary system exists is at ~ 60% - 40 % Ti-Mo ratio (CE value is 22.2 cm^2 C^{-1} at 600 nm) (with ±2,5% error). This optimum is in the polycrystalline domain

c., the second optimal composition for CE in the (TiO_2-MoO_3) binary system is at ~ 20% - 80 % Ti-Mo ratio (CE value is 19.8 cm^2 C^{-1} at 600 nm) (with ±2,5% error). This optimum is in the amorphous domain.

4. Using the method described in (1) in the (SnO_2-ZnO) binary system I proved that [T4] the maximum value of the CE is between 46 and 21 cm^2 C^{-1} between wavelengths of 400 and 800 nm at ~ (71–29) % Sn-Zn ratio. (with ±2,5% error)

5. I have proved that the examined mixed metal oxides have the potential to exhibit at least 3 times better CE values than the corresponding pure materials. [T2]

[T1] Noor, Taha Ismaeel ; Lábadi, Zoltán ; Petrik, Peter ; Fried, Miklós, Investigation of Electrochromic, Combinatorial TiO2-SnO2 Mixed Layers by Spectroscopic Ellipsometry Using Different Optical Models, MATERIALS 16 : 12 Paper: 4204 , 12 p. (2023), IF: 3.1, Q2. https://doi.org/10.3390/ijms26083547

[T2] Lábadi, Zoltán ; Taha Ismaeel, Noor ; Petrik, Péter ; Fried, Miklós, Electrochromic Efficiency in AxB(1−x)Oy-Type Mixed Metal Oxide Alloys, INTERNATIONAL JOURNAL OF MOLECULAR SCIENCES v.26 Paper: 3547 (2025), Impact factor: 4.9, D1, https://doi.org/10.3390/ijms26083547,

[T3] Lábadi, Zoltán ; Taha Ismaeel, Noor ; Petrik, Péter ; Fried, Miklós, (2024). Perspective Chapter: Electrochromic Efficiency in Ti x Me (1-x) O y Type Mixed Metal-Oxide Alloys. In Titanium Dioxide-Uses, Applications, and Advances.
IntechOpen,.https://www.intechopen.com/chapters/1199439

[T4] Lábadi, Zoltán ; Ismaeel, Noor T. ; Petrik, Péter ; Fried, Miklós, Compositional Optimization of Sputtered SnO2/ZnO Films for High Coloration Efficiency, INTERNATIONAL JOURNAL OF MOLECULAR SCIENCES 25 : 19 Paper: 10801 , 11 p. (2024) , Impact factor: 4.9, D1, https://doi.org/10.3390/ijms251910801

7 List of Publications

No	*Title*	*Name of journal or conference*	*IF, Q*
1-	https://ellipsometry.hu/Anyagtudomany-Symp-Matrahaza-2022-10-5-7-ISBN-978-963-449-320-4-2023.pdf ISBN: 9789634493204 Combinatorial Preparation and Characterization Methods for High Throughput Study of WO_3-MoO_3 Mixtures https://real.mtak.hu/163841/	Symposium on Materials Science Conference Journal **2022**	
2-	https://konf2022.kvk.uni-obuda.hu/program Combinatorial Preparation and Characterization Methods for High Throughput Study of Advanced Functional Materials ISBN 978-963-449-299-3 https://m2.mtmt.hu/gui2/?mode=browse&params=publication;33299496	XXXVIII. Kandó Conference **2022**	
3-	https://www.iasj.net/iasj/download/bd56f1e825a3bfa5 Study the Effect of Nano Aluminum Oxide Coating on PMMA as Thermal Insulator https://m2.mtmt.hu/gui2/?mode=browse&params=publication;33991701	Iraqi Journal of Laser **2022**	
4-	https://oda.uniobuda.hu/handle/20.500.14044/25779 Investigation of Combinatorial TiO_2-MoO_3 Mixed Layers to Optimize the Electrochromic Properties. https://m2.mtmt.hu/gui2/?mode=browse&params=publication;35435902 Óbuda University (2024) 420 p. pp. 394-406. , 13 p.	XXXIX. Kandó Conference **2023**	
5-	https://www.transfernow.net/dl/20240527e9HdX4Ik/Guhpemi8 ISBN 978-963-449-353-2 Combinatorial Preparation and Electrochromic Investigation of Metal Oxide Mixtures https://real.mtak.hu/195797/	Symposium on Materials Science Conference Journal **2023**	
6-	https://www.mdpi.com/1996-1944/16/12/4204 Investigation of Electrochromic, Combinatorial TiO_2-SnO_2 Mixed Layers by Spectroscopic Ellipsometry Using Different Optical Models https://real.mtak.hu/166660/	MATERIALS **2023**	**I.F. 3.4** **Q2** **Scopus**

7-	https://doi.org/10.3390/ijms251910801 Compositional Optimization of Sputtered SnO_2/ZnO Films for High Coloration Efficiency https://real.mtak.hu/207106/	International Journal of Molecular Sciences **2024**	**I.F. 4.9** **Q1** **Scopus** **D1**
8-	https://konf2024.kvk.uni-obuda.hu/program Investigation of Combinatorial TiO_2-MoO_3 Mixed Layers to Enhance the Coloration Efficiency https://m2.mtmt.hu/gui2/?mode=browse&params=publication;35637333	XL. Kandó Conference, 7-8 November **2024**	
9-	https://doi.org/10.5772/intechopen.1008197 Perspective Chapter: Electrochromic Efficiency in $Ti_xMe_{(1-x)}O_y$ Type Mixed Metal-Oxide Alloys. https://real.mtak.hu/id/eprint/210556	IntechOpen Journals Perspective chapter review from Book Section International: IntechOpen (**2025**) , 17 p.	
10-	Electrochromic efficiency in $A_xB_{(1-x)}O_y$ type mixed metal-oxide alloys. https://www.mdpi.com/1422-0067/26/8/3547 DOI: 10.3390/ijms26083547. https://m2.mtmt.hu/gui2/?mode=browse&params=publication;36084336	International Journal of Molecular Sciences **2025**	**I.F. 4.9** **Q1** **Scopus** **D1**
11-	Optimization of SnO_2/ZnO Films for Electrochromic Coloration Efficiency. ISBN: 978963449376. https://real.mtak.hu/id/eprint/216807	Symposium on Materials Science 2024. Óbudai Egyetem (**2025**) 39 p. pp. 7-10. , 4 p.	

6.1Unrelated publications in other scientific fields

No	*Title*	*Name of journal or conference*	*IF, Q*
1-	https://doi.org/10.32802/asmscj.2022.1263 The Effectiveness of a 980-nm Diode Laser to Treat Face Haemangioma: A Randomised within-Patient Trial https://m2.mtmt.hu/gui2/?mode=browse&params=publication;33991503	ASM Science Journal **2022**	**Scopus** **Q4**
2-	https://doi.org/10.32802/asmscj.2022.1215 The Combination Effect of Co_2 Laser and Topical Growth Factor Solution for Treatment of Atrophic Post-Burn Scar https://m2.mtmt.hu/gui2/?mode=browse&params=publication;33991556	ASM Science Journal **2022**	**Scopus** **Q4**

8 Future studies

In the future, we need to optimize the optical measurements like optical contrast, switching time, cycling stability are part of the planned future work on the subject, however, this needs to cut at least 20 small parts the 100 mm long sample. Each part (composition) must be measured multiple times individually, for example to determine cyclic durability or stability. This means a much longer measurement than the current ones. Further investigation of stoichiometric and sub-stoichiometric oxides for gas sensorics purposes see Fig 7-1. The physical, chemical, and structural properties of cutting-edge materials are strongly dependent on their composition. The common procedure to reveal the properties of concentration dependent phases is the preparation of numerous two (or more)-component samples, one for each $C_{(a)}/C_{(b=1-a)}$ composition, and the investigation of these individuals. This is a low efficiency procedure that costs enormous man and machine power. Contrarily, using the combinatorial material synthesis approach, materials libraries can be produced in one experiment that contain up to several hundreds or thousands of samples on a single substrate. To identify optimized material structures in an efficient way, adequate automated micro-spot material characterization tools must be applied. These methods can help us to search for more efficient advanced functional materials for micro, nano and optoelectronics, energy converters (solar cells) or different (optical or gas) sensor systems, architectural glazing, high-contrast displays, sunroofs, sunglasses and smart windows, etc.

Figure 7-1 Photographs (from different view-angles) of WoO_3/MoO_3 (lower) or WoO_{3-x}/MoO_{3-x} (upper) combinatorial sets on heat-able sensor chips. Left hand side is W-rich, and the right one is Mo-rich. No. 6 (middle one) is expected to be 50-50% in both cases. The upper rows show sub-oxides (semi-transparent layers, No. 2 was broken during tweezer handling) the bottom rows show oxides (transparent layers). The inserted photograph shows Pt contacted sample.

9 Teaching activity during semesters

1- Published review article in International Journal of Molecular Sciences journal (Electrochromic efficiency in $A_xB_{(1-x)}O_y$ type mixed metal-oxide alloys) in 10 of April 2025, (I.F. 4.9 and Q1 and D1). DOI: 10.3390/ijms26083547. https://www.mdpi.com/1422-0067/26/8/3547

2- I present my research in Symposium on Materials Science October 9-11-2024, Mátraháza, Hungary: Óbudai Egyetem (2025) 39. pp. 7-10, 4 p. ISBN: 978963449376. https://real.mtak.hu/id/eprint/216807

3- Published a perspective chapter review from Book Section in IntechOpen Journals: Electrochromic Efficiency in $Ti_xMe_{(1-x)}O_y$ Type Mixed Metal-Oxide Alloys. (2025) https://doi.org/10.5772/intechopen.1008197

4- Published an article in International Journal of Molecular Sciences journal: Compositional Optimization of Sputtered SnO_2/ZnO Films for High Coloration Efficiency. (I.F. 4.9 and Q1and D1). (2024). https://doi.org/10.3390/ijms251910801 .

5- I presented my research in XL. Kandó Conference, 7-8 November 2024 which held at Obuda University (Investigation of Combinatorial TiO_2-MoO_3 Mixed Layers to Enhance the Coloration Efficiency) Noor Taha Ismaeel, Lábadi Zoltán, Fried Miklós https://konf2024.kvk.uni-obuda.hu/program

6- I have a new publication, Authors: Noor Taha Ismaeel, Zoltan Labadi, Petrik Peter and Miklos Fried. Title: (Combinatorial Preparation and Electrochromic Investigation of Metal Oxide Mixtures), Symposium on Materials Science 2023 Bp, Hungary : Obuda University (2024) pp. 15-19. , 5 p., ISBN:9789634493532 https://real.mtak.hu/195797

7- I attend the 3rd edition of Surface Science Discussions - a free online seminar featuring lectures from well-renowned scientists in the field that takes place on 09-10.01.2024.

8- I presented my research in the XXXIX. Kandó Konferencia 2023, 9-10 of November in ÓbudaI Egyetem 1084 Budapest, Tavaszmező u. 17.

9- I participate and take a certificate from the Budapest School on Modern X-ray Science 2023, 3-6 of October in Research Centre for Natural Sciences (ttk), Budapest.

10- I responded to the invitation conference (How to increase the visibility of your research?) that held on the 8th of February 2023 at 14.00 –16.00, Rektori Tanácsterem, Óbuda University, Bécsi út 96/B, 1034.

11- I presented my research in the XXXVIII, 3-4 November 2022),1084 Budapest, Tavaszmező u. 17, which held at Obuda University. ISBN 978-963-449-299-3 (https://konf2022.kvk.uni-obuda.hu/program) Noor Taha, Lábadi Zoltán, Fried Miklós: {Combinatorial Preparation and Characterization Methods for High Throughput Study of Advanced Functional Materials}.

12- I attend the public defense of Mr. Hassanen Jaber's PhD dissertation in 6th of December 2022 in ÓE 1081.

13- I attended the autumn's doctoral ball, which took place on 07.10.2022. Evening of socializing, in Óbuda University.

14- I responded to the invitation of rector Prof. Dr. Levente Kovács. The Mini Symposium that held on the 6th of September 2022.

15- I attended the academic year opening ceremony on 5th of September 2022. in Budapest, Várkert Bazár, 1013.

16- I was being in the teaching course of Prof. DR. George Kaptay (Miskolc University) about "Art-of-doing-science" in English languages. The course is considered as "Seminar" 2021 in First semester.

17- I attended the lecture of Prof. Dr. Laszlo S. Toth presented on December 13, 2021, at 11 am. "Severe plastic deformation processes of metals and insight in deformation mechanisms by polycrystal simulations".

18- I attended home defense of the PhD work of Larbi Eddaif, titled: “Development of Functionalized Calix [4] resorcinarene-Based Sensor Platforms for Heavy Metals Ions Detection in Aqueous Solutions” nheled in the Research Centre for Natural Science on Tuesday, November 2nd, 2021, at 14.00.

19- I attended the welcome event in Obuda University in 94-96, building. Date: 2021.10.08. at 14:00.

List of figures

Figure 1-1: Relative transmission vs. input charge curves at five wavelengths for a pure WO_3 sample (a), for a WO_3-MO_3 (Mo-60.3%) mixed sample (b)and for a pure MoO_3 sample(c), CE values were determined from the fitted exponential curves [20] 5
Figure 2-1: Bleached and colored transmittance spectra of (a) TiO_2, (b) (WO_3/TiO_2) deposited, (c) (WO_3/TiO_2) annealed films [91] ……..... 10
Figure 2-2: Diffusion coefficient contrast of [(TiO_2-WO_3) and (TiO_2, WO_3)] films [92] ……... 11
Figure 2-3: (a) Cyclic voltammograms of the oxide nanotube (ONT) layers on Ti, Ti-0.2W, and Ti-9W performed between −0.7 and 1.0 V with a scan rate of 50 mV in 0.1 Mol $HClO_4$ electrolyte; (b) current density−time curves acquired by pulse potential measurement applied between −0.7 and 1.0 V with 30 s duration; (c) in situ reflectance curves of Ti, Ti-0.2W, and Ti-9W ONTs obtained during potential pulsing applied between 1.0 and -0.7 V; and (d) optical images of the electrochromic effect of the different nanotube surfaces during polarization cycling between 1 and −0.7 V. The inset of (b) show integrated charge density (Qd) for the samples. Reprinted (adapted) with permission [93] ……. 12
Figure 2-4: Transmittance variation curves at 633 nm when the a-WO_3 (a) and a-WO_3/SnO_2 NF (b) electrochromic windows were switched from bleached to colored state. Response times were indicated. Durability tests of the a-WO_3 (c) and a-WO_3/SnO_2 NF (d) electrochromic windows were cycled 500 times at 633 nm [96] ……...13
Figure 2-5: Spectral coloration efficiency for W–Ni oxide films with the compositions shown [98] ...……...14
Figure 2-6: ECD performances of the NiO/WO_3 ECD (ITO) show stability at different voltages [99] ……15
Figure 2-7: Transmittance switching response of (a) $WO_{3-\delta}$, (b) $W_{0.97}Ag_{0.03}O_{3-\delta}$, and (c) $W_{0.91}Ag_{0.09}O_{3-\delta}$ thin films grown at room temperature on ITO-coated glass substrates [101] ……. 16
Figure 2-8: Variation of the change in optical density (ΔOD) vs. charge density for WO_3, V_2O_5, and W-V thin films (a), In situ optical responses of WO_3 (b), V_2O_5 (c), and W-V (d) between the colored (−1 V) and bleached (+1 V) states at 700 nm for 1000s, performed in 1.0 M $LiClO_4$/PC [102] ……...18
Figure 2-9 Cross-sectional schematic view of the sputtering chamber and the target arrangement [20] ……...… 20
Figure 2-10: One example from the several XRD measurements showing one significant broad peak in the 20–30° region showing only amorhous microstructure in the electrochromic layer (left) 4x4 micron SEM micrograph from the center part of the combinatorial layer (right) [20] ……..…. 21
Figure 2-11: shows a significant CE maximum at 60% Mo content. This maximum increases towards the red end of the spectrum in the visible spectral range of 400-800 nm [20] ……... 22
Figure 3-1: DC magnetron sputtering systems ...……..…….……28
Figure 3-2: (a) the chamber for DC magnetron sputtering device after air vacuumed. Blue light is

from the Ar-O_2 plasma, (b) DC magnetron sputtering device parameters ……..…… 29
Figure 3-3: Schematic layout of the integrated vacuum system [142] ……..… 34
Figure 3-4: Spectroscopic Ellipsometry devices, Woollam M-2000DI …..……...…….. 36
Figure 3-5: a sample for data analysis parameters for Spectroscopic Ellipsometry device ……... 37
Figure 3-6: the principles of Spectroscopic Ellipsometry device [142] …..……...…….. 37
Figure 3-7: Mechanism of SE measurements and evaluation [148] …….…….…….. 39
Figure 3-8: Schematic for SE measurements [147] …….…… 40
Figure 3-9: a) All SEM components; b) Schematic of scanning electron microscope (SEM) [154] ..41
Figure 3-10: schematic view of the experimental setup of EDS [155] …..…….…….…… 42
Figure 3-11: SEM equipped with EDS [154] …….…….. 43
Figure 3-12: XRD Bruker AXS D8 instrument [158] …….. 44
Figure 3-13: The sample area of a reflectometry setup for XRD Bruker AXS D8 instrument [158]..44
Figure 4-1: (a) arrangements of the two targets in a closer position (35 cm from each other); (b) the chamber for the DC magnetron sputtering device after air vacuumed. Blue light is from the Ar-O_2 plasma ……. 48
Figure 4-2: (a) Graded TiO_2–SnO_2 layer on 3-inch Si (circular sample, upper) and the Si-stripe samples, lower; (b) Combinatorial TiO_2-SnO_2 layer on a 4-inch Si-wafer in the SEM-chamber (Dual-beam SEM+ FIB Thermo Scientific Scios2) …… 48
Figure 4-3: Combinatorial TiO_2–SnO_2 layer on highly conductive 3-inch Si-wafer in an electrochemical fluid cell during in situ, real-time SE measurements …….. 49
Figure 4-4: Comparison of (a) EMA; (b) 2T–L modelling (TiO_2-SnO_2); (c) MSE for EMA (the blue curve) vs. 2T–L (the orange curve), (d) is the thickness (EMA (the blue curve) vs. 2T–L (the orange curve) by home-made software version 1.0 coded in Python version 3.11 language …… 51
Figure 4-5: Shows TiO_2–SnO_2 maps from the 4 inch-wafer by BEMA modelling (left) 2T–L modelling (right), upper row: EMA% (left) and Tauc–Lorentz Amplitudes (right), middle row: total thickness maps, lower row: MSE maps (showing that the 2T–L model is better, the MSE values are lower). Pictures were made by the CompleteEASE v. 5.15 software.. 52
Figure 4-6: TiO_2–SnO_2 ratio curves from SE and SEM–EDS measurements at the center line of the 4-inch sample; (a) the blue curve for EMA% (E), the orange curve for Amp1 (TiO_2), the green curve for Amp2 (SnO_2); (b) Ti/Sn ratio from SEM–EDS measurements, (the blue curve for Ti ratio and the orange curve for Sn ratio); (c) SnO_2% derived from EMA (the blue curve, E), 2T–L models (the orange curve for Amp1 and the green curve for Amp2), the red curve for EDS% measurements (by home-made software coded in Python language) …… 53
Figure 4-7: Typical example of a fitted SE spectrum for the details of the model structure; SE spectra were evaluated using a multi-layer, multi-parameter optical model applying two-layer

Cauchydispersion. Pictures were made by the CompleteEASE v. 5.15 software ……. 55
Figure 4-8: (a) The imaginary part of the refractive index (k Amplitude) as a function of time for highly conductive Si in the liquid cell during coloration (time-scan, simple 2-layer Cauchy model). From 0–4 min, there is low absorption, however, from 4–8 min, there is a growing absorption; (b) Map of the k parameter after coloration (simple 1-layer Cauchy-model). Pictures were made by the CompleteEASE v. 5.15 software ……..… 55
Figure 4-9: TiO_2-MoO_3 (a) ITO-covered glass and Si-probes on a glass substrate, before-electrochromic experiments, the Ti in the left and the Mo in the right. (b) after-electrochromic- experiments ……..……...…… 58
Figure 4-10: TiO_2-MoO_3 in a transmission electrochemical cell during-electrochromic-experiment by SE …… 59
Figure 4-11: Coloration Efficiency of TiO_2-MoO_3. vs. Mo % for wavelengths from (400-800) nm by home-made software version 1.0 coded in Python version 3.11 language. (Individual color-coded curves represent different wavelengths: 1-400 nm, 2 -500 nm, 3-600 nm, 700 nm, 5-800 nm) ……..……...…… 60
Figure 4-12: diagram of the Coloration Efficiency data of TiO_2-MoO_3. vs. Mo % for wavelengths from (400-800) nm visible spectral range …… 60
Figure 4-13: SEM micrograph from the TiO_2-MoO_3 surface Ti-rich side ……... 62
Figure 4-14: SEM micrograph from the TiO_2-MoO_3 surface Mo-rich side ……. 62
Figure 4-15: Ti/Mo ratio measured on the Si-probes by SEM-EDS …… 62
Figure 4-16: The SnO_2-ZnO (a) arrangements of the two targets (at a 35 cm distance from each other) and the chamber for the DC magnetron sputtering after being vacuumed; the blue light is from the Ar-O_2 plasma. (b) ITO-covered glass and Si-probes on a glass substrate before the electrochromic experiments; the Sn on the left and the Zn on the right …… 64
Figure 4-17: Examples of XRD measurements: one from the Sn-side (upper), one from the mixed part (middle) and one from the Zn-side (lower). One can see only small and wide peaks (between 33 and 37 deg) in the lower diffractogram showing a trace of small ZnO nano crystallites (with a less than 10 nm diameter) ……...…… 65

Figure 4-18: SEM-EDS spectra from the Si-probes: Zn-rich side (upper), app. 50–50% (middle), Sn-rich side (below) ……...… 66
Figure 4-19: ZnO ratio measured on Si-probes and comparison of SE and SEM-EDS results …… 67
Figure 4-20: (a) Example normalized-intensity spectrum in bleached state (measured intensity divided by intensity without sample) of one sample point. (b) Curves of intensity versus time at five different wavelengths ……..……..…… 69

Figure 4-21: (a) CE of SnO_2-ZnO vs. Zn % for wavelengths from 350 to 800 nm (individual color-coded curves represent different wavelengths: 1–350 nm, 2–400 nm, 3–500 nm, 4–600 nm, 5–700 nm 6–800 nm. (b) Three-dimensional diagram of CE data of SnO_2-ZnO vs. Zn % for wavelengths from 400 to 800 nm in visible spectral range …… 71
Figure 4-22: Cyclic voltammograms as a function of scanning rate taken on $SnO_{2(0.3)}ZnO_{(0.7)}$ oxide film in 1M $LiClO_4$ propylene carbonate electrolyte ……..……. 72
Figure 7-1: Photographs (from different view-angles) of WoO_3/MoO_3 (lower) or WoO_{3-x}/MoO_{3-x} (upper) combinatorial sets on heat-able sensor chips. Left hand side is Wrich, and the right one is Mo-rich. No. 6 (middle one) is expected to be 50-50% in both cases. The upper rows show sub-oxides (semi-transparent layers, No. 2 was broken during tweezer handling) the bottom rows show oxides (transparent layers). The inserted photograph shows Pt contacted sample …….. 77

List of tables

Table 2-1: Electrochromic properties of WAg-0 and WAg-75 thin film in 0.5 M solution $LiClO_4$-PC at 632.8 nm [100] 16

Table 3-1: Deposition parameters and specific resistances [143] ……..…… 35

Table 3-2: Description of SEM specifications …….. 41

Table 4-1: Mean Squared Error (MSE) and Thickness values from EMA and 2T–L modelling …. 51

Table 4-2: Cauchy parameter k Amplitude vs. Time at the center point during the colorization process 56

Table 4-3: k Amplitude vs. Position at the center line after the colorization in the dry state …..…. 57

Table 4-4: calculated data for the CE according to the wavelengths (400-800) nm ……. 61

Table 4-5: Calculated data for CE according to wavelengths of 400–800 nm. The unit of CE is cm^2/C (square centimeters per Coulomb) 70

References

1. Lee JW, Jung HJ, Park JY, Lee JB, Yoon Y. Optimization of building window system in Asian regions by analyzing solar heat gain and daylighting elements. Renewable Energy. **2013**; 50; P.P. 522-531. DOI: 10.1016/j.renene.2012.07.029.
2. Granqvist CG. Oxide electrochromics: An introduction to devices and materials. Solar Energy Materials & Solar Cells. **2012**; 99; P.P. 1-13. DOI: 10.1016/j.solmat.2011.08.021.
3. Granqvist CG. Electrochromic materials: Out of a niche. Nature Materials. **2006**; 5; P.P. 89-90. DOI: 10.1038/nmat1577.
4. Llordé SA, Garcia G, Gazquez J, Milliron DJ. Tunable near-infrared and visible-light transmittance in nanocrystal-in glass composites. Nature. **2013**; 500; P.P. 323-326. DOI: 10.1038/nature12398.
5. Barile CJ, Slotcavage DJ, Hou J, Strand MT, Hernandez TS, McGehee MD. Dynamic windows with neutral color, high contrast, and excellent durability using reversible metal electrodeposition. Joule. **2017**; 1; P.P. 133-145. DOI: 10.1016/j.joule.2017.06.001.
6. DeForest N, Shehabi A, O'Donnell J, Garcia G, Greenblatt J, Lee ES, et al. United States energy and CO_2 savings potential from deployment of nearinfrared electrochromic window glazing's. Building and Environment. **2015**; 89; P.P. 107-117. DOI: 10.1016/j.buildenv.2015.02.021.
7. Wei Cheng; Jingfu He; Kevan E. Dettelbach; Noah J.J. Johnson; Rebecca S. Sherbo and Curtis P. Berlinguette, Photodeposited Amorphous Oxide Films for Electrochromic Windows, Chem **2018**, 4, pp. 821–832. https://doi.org/10.1016/j.chempr.2017.12.030
8. Gillaspie DT, Tenent RC, Dillon AC. Metal-oxide films for electrochromic applications: Present technology and future directions. Journal of Materials Chemistry. **2010**; 20; P.P.9585-9592. DOI: 10.1039/C0JM00604A.
9. Runnerstrom EL, Llordé SA, Lounis SD, Milliron DJ. Nanostructured electrochromic smart windows: Traditional materials and NIR-selective plasmonic nanocrystals. Chemical Communications. **2014**; 50; P.P. 10555-10572. DOI: 10.1039/C4CC03109A.
10. Granqvist CG. Electrochromics for smart windows: Oxide-based thin films and devices. Thin Solid Films. **2014**; 564; P.P.1-38. DOI: 10.1016/j.tsf.2014.02.002.
11. Cannavale A, Cossari P, Eperon GE, Colella S, Fiorito F, Gigli G, et al. Forthcoming perspectives of photoelectrochromic devices: A critical review. Energy & Environmental Science. **2016**; 9; P.P. 2682-2719. DOI: 10.1039/C6EE01514J.
12. Granqvist CG. Handbook of Inorganic Electrochromic Materials. Amsterdam, Netherlands: Elsevier; **1995**. ISBN: 9780080532905.
13. González-Borrero PP, Sato F, Medina AN, Baesso ML, Bento AC,Baldissera G, et al. Optical band-gapdetermination of nanostructured WO_3 film. Applied Physics Letters. **2010**; 96; P.P. 061909. DOI: 10.1063/1.3313945.

14. Novinrooz A, Sharbatdaran M, Noorkojouri H. Structural and optical properties of WO_3 electrochromic layers prepared by the sol-gel method. Central European Journal of Physics. **2005**; 3; P.P. 456-466. DOI: 10.2478/BF02475650.
15. Hsu C-S, Chan C-C, Huang H-T, Peng C-H, Hsu W-C. Electrochromic properties of nanocrystalline MoO_3 thinfilms. Thin Solid Films. **2008**; 516; P.P. 4839-4844. DOI: 10.1016/j.tsf.2007.09.019.
16. S. Chaichana; L. Sikong; K. Kooptarnond and K. Chetpattananondh. The electrochromic property of MoO_3/WO_3 nanocomposite films. IOP Conf. Ser. Mater. Sci. Eng. **2018**, 378, p.012002. https://doi.org/10.1088/1757-899X/378/1/012002
17. Colton RJ, Guzman AM, Rabalais JW. Photochromism and electrochromism in amorphous transition metal oxide films. Accounts of Chemical Research. **1978**; 11; P.P. 170-176. DOI: 10.1021/ar50124a008.
18. Wen RT, Granqvist CG, Niklasson GA. Eliminating degradation and uncovering ion-trapping dynamics in electrochromic WO_3 thin films. Nature Materials. **2015**; 14; P.P. 996-1001. DOI: 10.1038/nmat4368.
19. Llordes A, Wang Y, FernandezMartinez A, Xiao P, Lee T, Poulain A, et al. Linear topology in amorphous metal oxide electrochromic networks obtained via low-temperature solution processing. Nature Materials. **2016**; 15; Pp.p. 1267-1273. DOI: 10.1038/nmat4734.
20. Zoltán Lábad; Dániel Takács; Zsolt Zolnai; Péter Petrik and Miklós Fried. Compositional optimization of sputtered WO_3/MoO_3 films for high coloration efficiency. Materials **2024**, 17(5), p.1000. https://doi.org/10.3390/ma17051000
21. E. Zelakowska; E. Rysiakiewicz-Pasek. Thin TiO_2 films for an electrochromic system, Opt. Mater. **2009**, 31, p. 1802-1804. https://doi.org/10.1016/j.optmat.2008.12.037
22. P.S. Shinde; H.P. Deshmukh; S.H. Mujawar; A.I. Inamdar and P.S. Patil. Spray deposited titanium oxide thin films as passive counter electrodes. Electrochim. Acta **2007**, 52, p. 3114-3120. https://doi.org/10.1016/j.electacta.2006.09.053
23. S. Berger; A. Ghicov; Y.-C. Nah; P. Schmuki. Transparent TiO_2 Nanotube Electrodes via Thin Layer Anodization: Fabrication and Use in Electrochromic Devices. Langmuir **2009**, 25, p. 4841. https://doi.org/10.1021/la9004399
24. I. Paramasivam; J.M. Macak; A. Ghikov; P. Schmuki. Enhance photochromism of Ag loaded self-organized TiO_2 nanotube layers. Chem. Phys. Lett. **2007**, 445, p. 233. https://doi.org/10.1016/j.cplett.2007.07.107
25. R. Hahn; A. Ghikov; H. Tsuchiya; J.M. Macak; A.G. Muñoz and P. Schmuki. Lithium-ion insertion in anodic TiO_2 nanotubes resulting in high electrochromic contrast, Phys. Stat. Sol. A **2007**, 204, p. 1281-1285. https://doi.org/10.1002/pssa.200674310
26. S. Khalifa, H. Lin; S. Ismat Shah. Structural and electrochromic properties of TiO_2 thin films prepared by metallorganic chemical vapor deposition. Thin Solid Films **2010**, 518, p. 5457. https://doi.org/10.1016/j.tsf.2010.04.013

27. C.-M. Wang; S.-Y. Lin; Y.-C. Chen. Electrochromic properties of TiO_2 thin films prepared by chemical solution deposition method. J. Phys. Chem. Solids **2008**, 69, p. 451-455. https://doi.org/10.1016/j.jpcs.2007.07.113
28. S.-Y. Lin; Y.-C. Chen; C.-M. Wang; C.-C. Liu. Effect of heat treatment on electrochromic properties of TiO_2 thin films. J. Solid State Electrochem **2008**, 12, p. 1481-1486. https://link.springer.com/article/10.1007/s10008-007-0502-2
29. I. Sorar; E. Pehlivan; Niklasson, G.A. ; Granqvist, C.G. Electrochromism of DC magnetron sputtered TiO_2 thin films Role of deposition parameters. Sol. Energy Mater. Sol. Cells **2013**, 115, p. 172-180. https://doi.org/10.1016/j.solmat.2013.03.035
30. Cantao, M.P.; Cisneros, J.I.; Torresi, R.M. Electrochromic behavior of sputtered titanium oxide thin films. Thin Solid Film **1995**, 259, p. 70–74. https://doi.org/10.1016/0040-6090(94)06401-6
31. R. Sivakumar; C.S. Gopinath; M. Jayachandran; C. Sanjeeviraja. An electrochromic device (ECD) cell characterization on electron beam evaporated MoO_3 films by intercalating/deintercalating the H^+ ions. Curr. Appl. Phys. **2007**, 7, p. 76-86. https://doi.org/10.1016/j.cap.2005.12.001
32. A. Rougier; K. Sauvet; L. Sauques. Electrochromic materials from the visible to the infrared region: An example WO_3, Ionics **2008**, 14, p. 99-105. DOI:10.1007/s11581-007-0191-y.
33. K. Sauvet; A. Rougier; L. Sauques. Electrochromic WO_3 thin films active in the IR region. Sol. Energy Mater. Sol. Cells **2008**, 92, p. 209-215. https://doi.org/10.1016/j.solmat.2007.01.025
34. R. Sato; N. Kawamura; H. Tokumaru. Relaxation mechanism of electrochromism of tungsten-oxide film for ultra-multilayer optical recording depending on sputtering conditions. Jpn. J. Appl. Phys. **2007**, 46, p. 3958. DOI 10.1143/JJAP.46.3958.
35. K. Sauvet; L. Sauques; A. Rougier. IR electrochromic WO_3 thin films: From optimization to devices. Sol. Energy Mater. Sol. Cells **2009**, 93, p. 2045-2049. https://doi.org/10.1016/j.solmat.2009.05.003
36. C.-C. Liao; F.-R. Chen; J.-J. Kai. Annealing effect on electrochromic properties of tungsten oxide nanowires. Sol. Energy Mater. Sol. Cells **2007**, 91, p. 1258. https://doi.org/10.1016/j.solmat.2007.04.014
37. K. Hari Krishna; O.M. Hussain; C.M. Julien. Electrochromic properties of nanocrystalline WO_3 thin films grown on flexible substrates by plasma-assisted evaporation technique. Appl. Phys. A **2010**, 99, p. 921-929. DOI:10.1007/s00339-010-5681-5.
38. G. Beydaghyan; J.-L. Renaud; G. Bader; P.V. Ashrit. Enhanced electrochromic properties of heat-treated nanostructured tungsten trioxide thin films. J. Mater. Res. **2008**, 23, p. 274-280. DOI: https://doi.org/10.1557/JMR.2008.0037
39. P.C. Barbosa; M.M. Silva; M.J. Smith; A. Gonçalves; E. Fortunato. Optical Devices Performance with Poly (trim ethylene carbonate) based Electrolytes. Thin Solid Films **2008**, 516, p. 1480. DOI 10.1149/MA2009-01/45/1486.

40. A.A. Joraid. Comparison of electrochromic amorphous and crystalline electron beam deposited WO_3 thin films. Curr. Appl. Phys. **2009**, 9, p. 73-79. https://doi.org/10.1016/j.cap.2007.11.012
41. V.K. Laurinavichute; S.Yu. Vassiliev; L.M. Plyasova; I.Yu. Molina; A.A. Khokhlov; L.V. Pugolovkin; M.I. Borzenko and G.A. Tsirlina. Cathodic electrocrystallization and electrochromic properties of doped rechargeable oxotungstates. Electrochim. Acta **2009**, 54, p. 5439-5448. https://doi.org/10.1016/j.electacta.2009.04.035
42. C.-S. Hsu; C.-C. Chan; H.-T. Huang; C.-H. Peng; W.-C. Hsu. Electrochromic properties of nanocrystalline MoO_3 thin films, Thin Solid Films **2008**, 516, p. 4839-4844. https://doi.org/10.1016/j.tsf.2007.09.019
43. M. Dhanasankar; K.K. Purushothaman; G. Muralidharan. Effect of tungsten on the electrochromic behavior of sol–gel dip coated molybdenum oxide thin films. Mater. Res. Bull. **2010**, 45, p. 542-545. https://doi.org/10.1016/j.materresbull.2010.02.003
44. R.S. Patil; M.D. Uplane; P.S. Patil. Electrosynthesis of Electrochromic Molybdenum Oxide Thin Films with Rod-Like Features. Int. J. Electrochem. Soc. **2008**, 3, p. 259-265. https://doi.org/10.1016/S1452-3981(23)15451-4
45. K.A. Gesheva; A. Cziraki; T. Ivanova; A. Szekeres. Crystallization of chemically vapor deposited molybdenum and mixed tungsten/molybdenum oxide films for electrochromic application. Thin Solid Films **2007**, 515, p. 4609-4613. https://doi.org/10.1016/j.tsf.2006.11.042
46. C.E. Patil; N.L. Tarwal; P.R. Jadhav; P.S. Shinde; H.P. Deshmukh; M.M. Karanjkar; A.V. Moholkar; M.G. Gang; J.H. Kim and P.S. Patil. Electrochromic performance of the mixed V_2O_5–WO_3 thin films synthesized by pulsed spray pyrolysis technique. Current Applied Physics **2014**, 14(3), p. 389-395. https://doi.org/10.1016/j.cap.2013.12.014
47. J Scarminio; PR Catarini; A Urbano; RV Gelamo. Li diffusion and electrochromism in amorphous and crystalline vanadium oxide thin film electrodes. Journal of the Brazilian Chemical Society **2008**, 19 (4), P. 788-794. https://doi.org/10.1590/S0103-50532008000400025
48. C. Costa; C. Pinheiro; I. Henriques; C.A.T. Laia. Electrochromic Properties of Inkjet Printed Vanadium Oxide Gel on Flexible Polyethylene Terephthalate/Indium Tin Oxide Electrodes. ACS Appl. Mater. Interfaces **2012**, 8, p. 5266-5275. https://doi.org/10.1021/am301213b
49. S. Lee; J. Eom and H. Kwon. Electrochemical properties of amorphous $LixV_2O_{5-y}$ thin film deposited by r.f.-sputtering. J. Appl. Electrochem **2009**, 39, p.241-245. https://link.springer.com/article/10.1007/s10800-008-9662-8
50. M.R. Scherer; L. Li, P.M.S. Cunha; O.A. Scherman; U. Steiner. Enhanced Electrochromism in Gyroid-Structured Vanadium Pentoxide. Adv. Mater. **2012**, 24, p. 1217. https://doi.org/10.1002/adma.201104272
51. L. Li, U. Steiner; S. Mahajan. Improved electrochromic performance in inverse opal vanadium oxide films. J. Mater. Chem. **2010**, 20, p. 7131. https://doi.org/10.1039/C0JM00558D

52. C. Xiong; A.E. Aliev; B. Gnade; K.J. Balkus Jr. Fabrication of Silver Vanadium Oxide and V_2O_5 Nanowires for Electrochromics. ACS Nano **2008**, 2, p. 293. https://doi.org/10.1021/nn700261c
53. C.O. Avellaneda. Electrochromic performance of sol–gel deposited V_2O_5:Ta films. Materials Science and Engineering: B **2007**, 138, Issue 2, p.118-122. https://doi.org/10.1016/j.mseb.2006.06.007
54. M. Benmoussa; A. Outzourhit; A. Bennouna; A. Ihlad: Li+ ions diffusion into sol-gel V_2O_5 thin films: electrochromic properties. Eur. Phys. Journal Appl. Phys. **2009**, 48, p. 10502. https://doi.org/10.1051/epjap/2009118
55. D.S. Yakovleva; V.P. Malinenko; A.L. Pergament; G.B. Stefanovich. Electrical and optical properties of thin films of hydrated vanadium pentoxide featuring electrochromic effect. Tech. Phys. Lett. **2007**, 33, p.1022-1024. https://doi.org/10.1134/S1063785007120115
56. E. Avendaño; H. Rensmo; A. Azens; A. Sandell; G. de M. Azevedo; H. Siegbahn; G. A. Niklasson; C. G. Granqvist. Coloration Mechanism in Proton-Intercalated Electrochromic Hydrated NiO_y and $Ni_{1-x}V_xO_y$ Thin Films. J. Electrochem. Soc. **2009**, 56, P. 132. DOI: 10.1149/1.3148327.
57. E. Avendaño; A. Azens; G. A. Niklasson; C. G. Granqvist. Proton Diffusion and Electrochromism in Hydrated NiO_y and $Ni_{1-x}V_xO_y$ Thin Films, J. Electrochem. Soc. **2005**, 152 F203. DOI 10.1149/1.2077308
58. Noor Taha Ismaeel; Lábadi, Z.; Petrik, P.; Fried, M. Investigation of Electrochromic, Combinatorial TiO_2-SnO_2 Mixed Layers by Spectroscopic Ellipsometry Using Different Optical Models. Materials **2023**, 16(12), p. 4204. https://www.mdpi.com/1996-1944/16/12/4204
59. Noor Taha Ismaeel; Lábadi Z and Fried M. Investigation of Electrochromic Behavior of Combinatorial TiO_2-MoO_3 Mixed Layers. **2024**, Available from: https://www.preprints.org/manuscript/202407.0422/v1, DOI:10.20944/preprints202407.0422.v1; Zoltán Lábadi, Noor Taha Ismaeel, Peter Petrik and Miklós Fried. chapter review from Book Section in IntechOpen Journals: Electrochromic Efficiency in $Ti_xMe_{(1-x)}O_y$ Type Mixed Metal-Oxide Alloys (Chapter), in "Titanium Dioxide - Uses, Applications, and Advances, Eds.: Dr. Carlos Montalvo, Dr. Claudia Alejandra Aguilar and Dr. Edgar Moctezuma, DOI: 10.5772/intechopen.1008197. https://doi.org/10.5772/intechopen.1008197
60. Lábadi Z; Noor Taha Ismaeel; Petrik P and Fried M. Compositional Optimization of Sputtered SnO_2/ZnO Films for High Coloration Efficiency. International Journal of Molecular Sciences. **2024**; 25(19):10801. https://doi.org/10.3390/ijms251910801
61. Zoltán Lábadi; Noor Taha Ismaeel, Peter Petrik and Miklós Fried. Electrochromic Efficiency in $Ti_xMe_{(1-x)}O_y$ Type Mixed Metal-Oxide Alloys (Chapter), in "Titanium Dioxide - Uses, Applications, and Advances, Eds.: Dr. Carlos Montalvo, Dr. Claudia Alejandra Aguilar and Dr. Edgar Moctezuma, DOI: 10.5772/intechopen.1008197.

chapter review from Book Section in IntechOpen Journals **2024**. https://doi.org/10.5772/intechopen.1008197

62. Zoltán Lábadi; Noor Taha Ismaeel; Peter Petrik and Miklós Fried. Electrochromic efficiency in $A_xB_{(1-x)}O_y$ type mixed metal-oxide alloys. International Journal of Molecular Sciences. **2025**. DOI: 10.3390/ijms26083547. https://www.mdpi.com/1422-0067/26/8/3547
63. A. Šurca Vuk; V. Jovanovski; A. Pollet-Villard; I. Jerman and B. Orel. Imidazolium-based ionic liquid derivatives for application in electrochromic devices. Sol. Energy Mater. Sol. Cells **2008**, 92, p. 126-135. https://doi.org/10.1016/j.solmat.2007.01.023
64. S. Balaji; Y. Djaoued; A.-S. Albert; R.Z. Ferguson and R. Brüning. Hexagonal Tungsten Oxide Based Electrochromic Devices: Spectroscopic Evidence for the Li Ion Occupancy of Four-Coordinated Square Windows. Chem. Mater. **2009**, 21, p. 1381. DOI:10.1021/cm8034455.
65. S. Balaji; Y. Djaoued; A.-S. Albert; R.Z. Ferguson; R. Brüning; B.-L. Su. Construction and characterization of tunable me-so-/macroporous tungsten oxide-based transmissive electrochromic devices. J. Mater. Sci. **2009**, 44, pp. 6608-6616. doi:10.1007/s10853-009-3575-8.
66. R. Deshpande; S.-H. Lee; A.H. Mahan; P.A. Parilla; K.M. Jones; A.G. Norman; B. To, J.L. Blackburn. S. Mitra, A.C. Dillon. Optimization of crystalline tungsten oxide nanoparticles for improved electrochromic applications. Solid State Ionics **2007**, 178, p. 895-900. doi:10.1016/j.ssi.2007.03.010.
67. S. Gubbala; J. Thangala; M.K. Sunkara. Nanowire-based electrochromic devices. Sol. Energy Mater. Sol. Cells **2007**, 91, pp. 813-820. DOI:10.1016/j.solmat.2007.01.016.
68. C.M. White; D.T. Gillaspie; E. Whitney; S.-H. Lee; A.C. Dillon. Flexible electrochromic devices based on crystalline WO_3 nanostructures produced with hot-wire chemical vapor deposition. Thin Solid Films **2009**, 517, p. 3596-3599. https://doi.org/10.1016/j.tsf.2009.01.033.
69. L.M. Bertus; A. Enesca; A. Duta. Influence of spray pyrolysis deposition parameters on the optoelectronic properties of WO_3 thin films Thin Solid Films **2012**, 520, p. 4282-4290. https://doi.org/10.1016/j.tsf.2012.02.052
70. S.R. Bathe; P.S. Patil. Titanium doping effects in electrochromic pulsed spray pyrolysed WO_3 thin films. Solid State Ionics **2008**, 179, p. 314-323. https://doi.org/10.1016/j.ssi.2008.02.052
71. S.R. Bathe; P.S. Patil. Electrochromic characteristics of fibrous reticulated WO_3 thin films prepared by pulsed spray pyrolysis technique Sol. Energy Mater. Sol. Cells **2007**, 91, p. 1097-1101. https://doi.org/10.1016/j.solmat.2007.03.005
72. Chang-Yeoul Kim; Seong-Geun Choa; Seok Park and J.ceram.: Tungsten oxide film synthesis by spray pyrolysis of peroxotungstic acid and its electrochromic characterization. Journal of Ceramic Processing Research **2009**, 10 (6), p. 851-854. http://dx.doi.org/10.36410/jcpr.2009.10.6.851

73. P.M. Kadam; N.L. Tarwal; P.S. Shinde; R.S. Patil; H.P. Deshmukh; P.S. Patil. From beads-to-wires-to-fibers of tungsten oxide: electrochromic response Appl. Phys. A **2009**, 97, p. 323-330. https://doi.org/10.1007/s00339-009-5334-8
74. J.-H. Kang; S.-M. Paek; S.-J. Hwang; J.-H. Choy. Optical iris application of electrochromic thin films. Electrochem. Commun. **2008**, 10, pp. 1785-1787. https://doi.org/10.1016/j.elecom.2008.09.013
75. L.V. Kondrachova, R.A. May, C.W. Cone, D.A. Vanden Bout, K.J. Stevenson, Langmuir. Evaluation of Lithium-Ion Insertion Reactivity via Electrochromic Diffraction-Based Imaging. Mesoporous Electrodes **2009**, 25, p. 2508-2518. https://doi.org/10.1021/la803245a
76. E. Khoo; P.S. Lee; J. Ma. Electrophoretic deposition (EPD) of WO_3 nanorods for electrochromic application. J. Eur. Ceram. Soc. **2010**, 30, p. 1139-1144. https://doi.org/10.1016/j.jeurceramsoc.2009.05.014
77. J. Zhang; X.L. Wang; X.H. Xia; C.D. Gu; Z.J. Zhao; J.P. Tu. Enhanced electrochromic performance of macroporous WO_3 films formed by anodic oxidation of DC-sputtered tungsten layers. Electrochim. Acta **2010**, 55, p. 6953-6958. https://doi.org/10.1016/j.electacta.2010.06.082
78. Y.-C. Nah; A. Ghicov; D. Kim; P. Schmuki. Self-organized nano-tubes of TiO_2MoO_3 with enhanced electrochromic properties. Electrochem. Commun. **2008**, 10, p. 1777. DOI:10.1039/b820953g.
79. J.Z. Ou; S. Balendhran; M.R. Field; D.G. McCulloch; A.S. Zoolfakar; R.A. Rani; S. Zhuiykov; A.P. O'Mullane; K. Kalantar-zadeh. The anodized crystalline WO_3 nanoporous network with enhanced electrochromic properties. Nanoscale **2012**, 4, p. 5980-5988. https://doi.org/10.1039/C2NR31203D
80. T. Ivanova; A. Harizanova; T. Koutzarova; N. Krins; B. Vertruyen. Electrochromic TiO_2, ZrO_2 and TiO_2–ZrO_2 thin films by dip-coating method Mater. Sci. Eng. B **2009**, 165, p. 212-216. https://doi.org/10.1016/j.mseb.2009.07.013
81. I. Sorar; E. Pehlivan; G.A. Niklasson; C.G. Granqvist. Electrochromism of DC magnetron sputtered TiO_2 thin films: Role of deposition parameters Sol. Energy Mater. Sol. Cells **2013**, 115 p. 172-180. https://doi.org/10.1016/j.solmat.2013.03.035
82. P.R. Bueno; C. Gabrielli and H. Perrot. Coloring ionic trapping states in WO_3 and Nb_2O_5 electrochromic materials. Electrochim. Acta **2008**, 53, p. 5533-5539. https://doi.org/10.1016/j.electacta.2008.03.004
83. G. Agarwal; G.B. Reddy. Study of Mg^{2+}-Intercalated Nb_2O_5 Thin Films for Electrochromic Applications J. Electrochem. Soc. **2007**, 154, p. A417. DOI 10.1149/1.2710196.
84. S.H. Mujawar; A.I. Inamdar; C.A. Betty; V. Ganesan and P.S. Patil. Effect of post annealing treatment on electrochromic properties of spray deposited niobium oxide thin films. Electrochim. Acta **2007**, 52, p. 4899-4906. https://doi.org/10.1016/j.electacta.2007.01.054

85. R. Romero; E.A. Dalchiele; F. Martín; D. Leinen and J.R. Ramos-Barrado. Electrochromic behavior of Nb_2O_5 thin films with different morphologies obtained by spray pyrolysis Sol. Energy Mater. Sol. Cells **2009**, 93, p. 222-229. https://doi.org/10.1016/j.solmat.2008.10.012
86. R.S. Devan; S.-Y. Gao; W.-D. Ho; J.-H. Lin; Y.-R. Ma; P.S. Patil and Y. Liou. Electrochromic properties of large-area and high-density arrays of transparent one-dimensional β-Ta_2O_5 nanorods on indium-tin-oxide thin-films. Appl. Phys. Lett. **2011**, 98, p. 133117. https://doi.org/10.1063/1.3568896
87. Şilik, E.; Pat, S.; Özen, S.; Mohammadigharehbagh, R.; Yudar, H.H.; Musaoğlu, C.; Korkmaz, Ş. Electrochromic properties of TiO_2 thin films grown by thermionic vacuum arc method. Thin Solid Film. **2017**, 640, PP. 27–32. https://doi.org/10.1016/j.tsf.2017.07.073
88. Dawood Obied Altiafy; Hussien Ali Jawad and Noor Taha Ismaeel. Study the Effect of Nano Aluminum Oxide Coating on PMMA as Thermal Insulator. Iraqi J. Laser **2022**, 21(2), p. 9-15. https://doi.org/10.31900/ijl.v21i2.329
89. G.F. Cai; D. Zhou; Q.Q. Xiong; J.H. Zhang; X.L. Wang; C.D. Gu and J.P. Tu. Efficient electrochromic materials based on TiO_2- WO_3 core/shell nanorod arrays. Solar Energy Materials and Solar Cells **2013**, 117, p.231-238. https://doi.org/10.1016/j.solmat.2013.05.049
90. P.S. Patil; S.H. Mujawar; A.I. Inamdar and S.B. Sadale. Electrochromic properties of spray deposited TiO_2-doped WO_3 thin films. Applied Surface Science **2005**, 250, p 117-123. https://doi.org/10.1016/j.apsusc.2004.12.042
91. T. Dhandayuthapani; R. Sivakumar; D. Zheng, H. Xu; R. Ilangovan; C. Sanjeeviraja and J. Lin. WO_3/TiO_2 hierarchical nanostructures for electrochromic applications. Materials Science in Semiconductor Processing, **2021**, 123, p.105515. https://doi.org/10.1016/j.mssp.2020.105515
92. Ashok Reddy G V; Habibuddin Shaik; K.Naveen Kumar; V. Madhavi; Hitha D. Shetty; Sheik Abdul Sattar; Merum Dhananjaya; B. Daruka Prasad; G.Ranjith Kumar and B.H. Doreswamy. Structural and electrochemical studies of WO_3 coated TiO_2 nanorod hybrid thin films for electrochromic applications, Optik, **2023**, 277, p. 170694. https://doi.org/10.1016/j.ijleo.2023.170694
93. Yoon-Chae Nah, Andrei Ghicov, Doohun Kim, Steffen Berger, and Patrik Schmuki, TiO_2−WO_3 Composite Nanotubes by Alloy Anodization: Growth and Enhanced Electrochromic Properties, J. Am. Chem. Soc. **2008**, 130, 48, 16154–16155. https://doi.org/10.1021/ja807106y
94. Ronn Goei; Amanda Jiamin Ong; Tan Jun Hao; Loke Jie Yi; Lua Shun Kuang; Daniel Mandler; Shlomo Magdassi; Alfred Iing Yoong Tok. Novel Nd–Mo co-doped SnO_2/α-WO_3 electrochromic materials (ECs) for enhanced smart window performance. Ceramics International, **2021**, 47, pp.18433-18442. https://doi.org/10.1016/j.ceramint.2021.03.167

95. Kue-Ho Kim; Bon-Ryul Kooan and Hyo-Jin Ahn. Effects of Sb-doped SnO_2-WO_3 nanocomposite on electrochromic performance. Ceramics International **2019**, 45, P 15990-15995. https://doi.org/10.1016/j.ceramint.2019.05.109
96. Wei, Zeyang Li; Zhipeng Guo; Yihang Li; Fengming Hou; Wei Guo and Ang Wei. An electrochromic window based on hi-erarchical amorphous WO_3/SnO_2 nanoflake arrays with boosted NIR modulation, Applied Surface Science, **2022**, 571, p. 151277. https://doi.org/10.1016/j.apsusc.2021.151277
97. S.V. Green. Electrochromic Nickel–Tungsten Oxides: Optical, Electrochemical and Structural Characterization of Sputter-deposited Thin Films in the Whole Composition Range, Digital Comprehensive Summaries of Uppsala Dissertations from the Faculty of Science and Technology, **2012**, 963, ISBN 978-91-554-8444-6.
98. S.V. Green; E. Pehlivan; C.G. Granqvist and G.A. Niklasson. Sol. Energy Mater. Sol. Cells, **2012**, 99, pp. 339-344. https://doi.org/10.1016/j.solmat.2011.12.025
99. Md Rakibuddin; Mahesh A. Shinde and Haekyoung Kim. Sol-gel fabrication of NiO and NiO/WO_3 based electrochromic device on ITO and flexible substrate. Ceramics International, **2020**, 46, Pp. 8631-8639. https://doi.org/10.1016/j.ceramint.2019.12.096
100. Hamed Najafi Ashtian; Ali Bahari and Samira Gholipour. Investigation of coloration efficiency for tungsten oxide–silver nano-composite thin films with different surface morphologies. Journal of Materials Science: Materials in Electronics **2018**, 29, p 5820–5829. https://doi.org/10.1007/s10854-018-8554-x
101. Yong Jun Park; Deokyeon Lee; Kwang-Mo Kang; Sumin Choi; Minkyung Shin; Seung Ho Han; Il Heo; Ho Seong Jang; Yoon-Chae Nah and Dong Hun Kim. Enhanced electrochromic properties of Ag-incorporated WO_3 nanocomposite thin films. Ceramics In-ternational, **2023**, 49, Issue 11, Part A, pp. 17969-17976. https://doi.org/10.1016/j.ceramint.2023.02.166
102. Aryal Krishna Prasad; Jong-Young Park; Soon-Hyung Kang and Kwang-Soon Ahn. Electrochemically co-deposited WO_3-V_2O_5 composites for electrochromic energy storage applications. Electrochimica Acta **2022**, 422, p.140340, https://doi.org/10.1016/j.electacta.2022.140340
103. M.S. Burdis; J.R. Siddle; R.A. Batchelor and J.M. Gallego. $V_{0.50}Ti_{0.50}O_x$ thin films as counter electrodes for electrochromic devices. Solar Energy Materials and Solar Cells **1998**, 54, pp. 93-98. https://doi.org/10.1016/S0927-0248(98)00059-2
104. C. Marcel; C. Brigouleix; A. Vincent; D. Plessis; G. Nouhaud; Y. Hamon; F. Sabary and G. Campet. Electrochromic properties of lithium flexible devices based on tungsten and vanadium-titanium oxide thin films. in: A. Rougier; D. Rauh and G.A. Nazri (Eds.). Electrochromic Materials and Applications. The Electrochemical Society, Pennington, NJ, U.S.A., **2003**, p. 218.
105. C. Prameela; K. Srinivasarao. Characterization of $(MoO_3)_x$-$(Wo_3)_{1-x}$ composites. International Journal of Applied Engineering Research **2015**, 10, p. 9865–9875. https://www.researchgate.net/publication/281759164_Characterization_of_MoO3x_-_Wo31-x_composites

106. B. W. Faughnan; R. S. Crandall. Optical properties of mixed-oxide WO_3/MoO_3 electrochromic films. Appl. Phys. Lett. **1977**, *31*, pp. 834–836. https://doi.org/10.1063/1.89566
107. B. W. Faughnan; R. S. Crandall and P. M. Heyman. Electrochromism in WO_3 Amorphous Films. RCA REVIEW. **1975**, 36, pp.177-197. https://www.scirp.org/reference/referencespapers?referenceid=1909264
108. F. Hamelmann; K. Gesheva; T. Ivanova; A. Szekeres; M. Abrashev and U. Heinzmann. Optical and electrochromic characteri-zation of multilayered mixed metal oxide thin films. Journal of Optoelectronics and Advanced Materials **2005**, 7, pp. 393 – 396. https://pub.uni-bielefeld.de/record/1604360
109. M A Arvizu; C G Granqvist and G A Niklasson. Electrochromism in sputter deposited W_{1-y} Mo_yO_3 thin films. Journal of Physics: Conference Series, **2016**, 682, p.012005. DOI:10.1088/1742-6596/682/1/012005.
110. N.K. Shrestha; Y.-C. Nah; H. Tsuchiya; P. Schmuki. Self-organized nano-tubes of TiO_2–MoO_3 with enhanced electrochromic properties. Chem. Commun **2009**, Issu 15, https://doi.org/10.1039/B820953G
111. B. Ezhilmaran and S.V. Bhat: Enhanced charge transfer in TiO_2 nanoparticles/ MoO_3 nanostructures bilayer heterojunction electrode for efficient electrochromism, Materials Today Communications, **2022**, 31, P. 103497, https://doi.org/10.1016/j.mtcomm.2022.103497
112. Saman Habashyani, Soheil Mobtakeri, Hasan Feyzi Budak, Ahmet Emre Kasapoğlu, Ömer Çoban, Emre Gür, Electrochromic properties of undoped and Ti-doped MoO_3 converted from nano-wall MoS_2 thin films, Electrochimica Acta, **2024**, 498, P. 144638, https://doi.org/10.1016/j.electacta.2024.144638
113. Susumu Sato and Yosuke Seino. Electrochromism in evaporated WO_3-MoO_3-V_2O_5 films. Electronics and Communications in Japan (Part I: Communications) **1982**, 65(8), p. 104-111. https://doi.org/10.1002/ecja.4410650814
114. Seong Uk Yun; Sung Jong Yoo; Ju Wan Lim; Sun Ha Park; In Young Cha and Yung-Eun Sung. Enhanced Electrochromic Properties of Ir–Ta Oxide Grown Using a Co sputtering System. J. Electrochem. Soc. **2010**, 157, p.256. DOI: 10.1149/1.3425616.
115. Hyun Mok Cho, Yong Jin Hwang, Hyo Seok Oh, Hyeon Seong Hwang, Kitae Kim, Se-Um Kim, Jun-Hee Na: Recent Advances in Electrochromic Devices: From Multicolor to Flexible Applications, Advanced Photonics Research, 18 August **2024**, https://doi.org/10.1002/adpr.202400103
116. Dinghui Chen, Ming Hui Chua, Qiang He, Qiang Zhu, Xizu Wang, Hong Meng, Jianwei Xu, Wei Huang: Multifunctional electro-chromic materials and devices recent advances and future potential, Chemical Engineering Journal, **2025**, 503, P. 157820, https://doi.org/10.1016/j.cej.2024.157820
117. Livage, J.; Ganguli, D. Sol-gel electrochromic coatings and devices: A review. Sol. Energy Mater. Sol. Cells **2001**, 68, p. 365–381. https://doi.org/10.1016/S0927- 0248(00)00369-X

118. Ahmed, M.I.; Jahin, H.S.; Dessouki, H.A.; Nassar, M.Y. Synthesis and characterization of γ-Al_2O_3 and α-Al_2O_3 nanoparticles using a facile, inexpensive auto-combustion approach. Egypt. J. Chem. **2021**, 64, p. 2509–2515. doi:10.21608/ejchem.2021.61793.3330.
119. Basavaraj, M.K.; Kulkarni, S.N.; Elangovan, K.; Shankar, S. Effect of Concentration of Al_2O_3 Nano Particles in Base Fluid on Thermal and Flow Properties to Enhance the Heat Transfer Rate. Int. J. Eng. Res. Technol. (IJERT) **2021**, 10. DOI :10.17577/IJERTV10IS020028.
120. Zimmer, A.; Gilliot, M.; Broch, L.; Boulanger, C.; Stein, N.; Horwat, D. Morphological and chemical dynamics upon electrochemical cyclic sodiation of electrochromic tungsten oxide coatings extracted by in situ ellipsometry. Appl. Opt. **2020**, 59, p. 3766–3772. https://doi.org/10.1364/AO.389063
121. Hale, J.S.; DeVries, M.; Dworak, B.; Woollam, J.A. Visible and infrared optical constants of electrochromic materials for emissivity modulation applications. Thin Solid Film. **1998**, 313, p. 205–209. https://doi.org/10.1016/S0040-6090(97)00818-3
122. Shan, A.; Fried, M.; Juhasz, G.; Major, C.; Polgár, O.; Németh, Á.; Petrik, P.; Dahal, L.R.; Chen, J.; Huang, Z. High-speed imaging/mapping spectroscopic ellipsometry for in-line analysis of roll-to-roll thin-film photovoltaics. IEEE J. Photovolt. **2014**, 4, p. 355–361. DOI:10.1109/JPHOTOV.2013.2284380.
123. Koirala, P.; Tan, X.; Li, J.; Podraza, N.J.; Marsillac, S.; Rockett, A.; Collins, R.W. Mapping spectroscopic ellipsometry of CdTe solar cells for property-performance correlations. In Proceedings of the 2014 IEEE 40th Photovoltaic Specialist Conference (PVSC), Denver, CO, USA, 8–13 June **2014**; p. 674–679.
124. Dahal, L.R.; Li, J.; Stoke, J.A.; Huang, Z.; Shan, A.; Ferlauto, A.S.; Wronski, C.R.; Collins, R.W.; Podraza, N.J. Applications of real-time and mapping spectroscopic ellipsometry for process development and optimization in hydrogenated silicon thin-film photovoltaics technology. Sol. Energy Mater. Sol. Cells **2014**, 129, p. 32–56. https://doi.org/10.1016/j.solmat.2014.01.028
125. Aryal, P.; Pradhan, P.; Attygalle, D.; Ibdah, A.-R.; Aryal, K.; Ranjan, V.; Marsillac, S.; Podraza, N.J.; Collins, R.W. Real-time, in-line, and mapping spectroscopic ellipsometry for applications in Cu (in Ga) Se metrology. IEEE J. Photovolt. **2014**, 4, p. 33–339. DOI:10.1109/JPHOTOV.2013.2282745.
126. Fried, M.; Bogar, R.; Takacs, D.; Labadi, Z.; Horvath, Z.E.; Zolnai, Z. Investigation of Combinatorial WO_3-MoO_3 Mixed Layers by Spectroscopic Ellipsometry Using Different Optical Models. Nanomaterials **2022**, 12, p. 2421. https://doi.org/10.3390/nano12142421
127. Sharma, S.; Kumar, N.; Makgwane, P.R.; Chauhan, N.S.; Kumari, K.; Rani, M.; Maken, S. TiO_2/SnO_2 nano-composite: New insights in synthetic, structural, optical and photocatalytic aspects. Inorg. Chim. Acta **2022**, 529, p. 120640. https://doi.org/10.1016/j.ica.2021.120640

128. Rajput, R.B.; Jamble, S.N.; Kale, R.B. A review on TiO_2/SnO_2 heterostructures as a photocatalyst for the degradation of dyes and organic pollutants. J. Environ. Manag. **2022**, 307, p. 114533. https://doi.org/10.1016/j.jenvman.2022.114533
129. Jellison, G.E., Jr.; Modine, F.A. Parameterization of the optical functions of amorphous materials in the inter band region. Appl.Phys. Lett. **1996**, 69, p. 371–373. https://doi.org/10.1063/1.118064
130. S.S. Mahajan; S.H. Mujawar; P.S. Shinde; A.I. Inamdar; P.S. Patil. Structural, morphological, optical and electrochromic properties of Ti-doped MoO_3 thin films, Sol. Energy Mater. Sol. Cells **2009**, 93, p. 183-187. https://doi.org/10.1016/j.solmat.2008.09.025
131. Haiyan Yu; Yajun Li; Lei Zhao; Guangmin Li; Junwei Li; Hui Rong; Zhifeng Liu. Novel MoO_3-TiO_2 composite nanorods films with improved electrochromic performance. Materials Letters **2016**, 169, P. 65-68. DOI:10.1016/j.matlet.2016.01.097
132. Miccoli, I.; Spampinato, R.; Marzo, F.; Prete, P.; Lovergine, N. DC-magnetron sputtering of ZnO:Al films on (00.1)Al_2O_3 substrates from slip-casting sintered ceramic targets. Appl. Surface Sci. **2014**, 313, P. 418–423. https://doi.org/10.1016/j.apsusc.2014.05.225
133. Semong, O.; Batlokwa, B.S. Rapid colorimetric detection of Hg (II) based on Hg (II)-Induced suppressed enzyme-like reduction of 4-nitrophenol by Au@ZnO/Fe_3O_4 in a cosmetic skin product. Nanomater. Nanotechnol. **2023**, 14, 3603680. https://doi.org/10.1155/2023/3603680
134. Prete, P.; Lovergine, N.; Tapfer, L. Nanostructure size evolution during Au-catalysed growth by carbo-thermal evaporation of well-aligned ZnO nanowires on (100) Si. Appl. Phys. A **2007**, 88, p. 21–26. https://doi.org/10.1007/s00339-007-3946-4
135. Xu, L.; Shi, L.; Li, X. Effect of TiO_2 buffer layer on the structural and optical properties of ZnO thin films deposited by E-beam evaporation and sol–gel method. Appl. Surf. Sci. **2008**, 255, p. 3230–3234. https://doi.org/10.1016/j.apsusc.2008.09.026
136. Garratt, E.; Prete, P.; Lovergine, N.; Nikoobakht, B. Observation and Impact of a Surface Skin Effect on Lateral Growth of Nanocrystals. J. Phys. Chem. C **2017**, 121, p. 14845–14853. https://pubs.acs.org/doi/10.1021/acs.jpcc.7b02299
137. Wang, F.; Jia, J.; Zhao, W.; Zhang, L.; Ma, H.; Li, N.; Chen, Y. Preparation and electrochromic properties of NiO and ZnO-doped NiO thin films. Mater. Sci. Semiconduct. Process. **2022**, 151, 106986. https://doi.org/10.1016/j.mssp.2022.106986
138. García-Cañadas, J.; Mora-Seró, I.; Fabregat-Santiago, F.; Bisquert, J.; Garcia-Belmonte, G. Analysis of cyclic voltammograms of electrochromic a-WO_3 films from voltage-dependent equilibrium capacitance measurements. J. Electroanal. Chem. **2004**, 565, p. 329–334. https://doi.org/10.1016/j.jelechem.2003.10.027
139. Safi I. Recent aspects concerning DC reactive magnetron sputtering of thin films: a review. Surface and Coatings Technology, **2000**;127, P.19-203. https://doi.org/10.1016/S0257-8972(00)00566-1

140. Efim Oks; André Anders. A self-sputtering ion source: A new approach to quiescent metal ion beams. Rev. Sci. Instrum, **2010**, 81. https://doi.org/10.1063/1.3272797
141. J. L. Vossen, W. Kern. General textbook about sputtering and magnetron principle. Thin Film Processes (Academic Press, **1978**)
142. A. Németh, Z. Labadi, V. Rakovics, I. Bársony, I. Krafcsik: Solar Cell Technology Innovation Center at MTA MFA, Hiradástechnika, **2008**, 63. P. 34-38.
143. C. Major, A. Nemeth, G. Radnoczi, Zs. Czigany, M. Fried, Z. Labadi, I. Barsony. Optical and electrical characterization of aluminium doped ZnO layers. Applied Surface Science **2009**, 255. P. 8907-8912. doi:10.1016/j.apsusc.2009.06.088.
144. A´. Ne´meth, Z. La´badi, L. To´th, I. Ba´rsony. Oscillations and power-dependent hysteresis in reactive ZnO plasma. Elsevier **2010**, 84, p. 218–220. doi:10.1016/j.vacuum.2009.05.011.
145. D Abou-Ras, R Caballero, C-H Fischer, C A Kaufmann, I Lauermann, R Mainz, H Mönig, A Schöpke, C Stephan, C Streeck, S Schorr, A Eicke, M Döbeli, B Gade, J Hinrichs, T Nunney, H Dijkstra, V Hoffmann, D Klemm, V Efimova, A Bergmaier, G Dollinger, T Wirth, W Unger, A A Rockett, A Perez-Rodriguez, J Alvarez-Garcia, V Izquierdo-Roca, T Schmid, P-P Choi, M Müller, F Bertram, J Christen, H Khatri, R W Collins, S Marsillac, I Kötschau. Comprehensive comparison of various techniques for the analysis of elemental distributions in thin films. Microscopy Microanal, **2011**, 17, p. 728. doi: 10.1017/S1431927611000523.
146. Benjamin Kalas, Emil Agocs, Alekszej Romanenko, Peter Petrik. In Situ Characterization of Biomaterials at Solid-Liquid Interfaces Using Ellipsometry in the UV-Visible-NIR Wavelength Range. Phys. Status Solidi (a) **2019**, 216, 1800762. https://doi.org/10.1002/pssa.201800762
147. Fujiwara, H. Spectroscopic Ellipsometry Principles and Applications; John Wiley & Sons: Hoboken, NJ, USA, **2007**; Print ISBN9780470016084; Online ISBN 9780470060193. DOI:10.1002/9780470060193.
148. Available online: https://www.jawoollam.com/products/m-2000-ellipsometer (accessed on 12 July 2022).
149. Petrik, P.; Fried, M. Mapping and Imaging of Thin Films on Large Surfaces: A review. Phys. Status Solidi **2022**, 219, p. 2100800. https://doi.org/10.1002/pssa.202100800
150. Bruggeman, D.A.G. Dielectric constant and conductivity of mixtures of isotropic materials. Ann. Phys. 1935, 24, p. 636–664. https://doi.org/10.1002/andp.19354160705
151. L.D.S. Yadav. Organic Spectroscopy. Springer Science+Business Media Dordrecht Originally published by Kluwer Academic Publishers in **2005**. ISBN 978-94-017-2508-8, ISBN 978-1-4020-2575-4 (eBook). DOI 10.1007/978-1-4020-2575-4.
152. Kalsoom Akhtar, Shahid Ali Khan, Sher Bahadar Khan and Abdullah M. Asiri. Scanning Electron Microscopy: Principle and Applications in Nanomaterials

Characterization. In: Sharma, S. (eds) Handbook of Materials Characterization. Springer, Cham. **2018**, p. 113-145. https://doi.org/10.1007/978-3-319-92955-2_4

153. L Reimer. Scanning Electron Microscopy: Physics of Image Formation and Microanalysis, Second Edition Book Review. Measurement Science and Technology **2000**. DOI 10.1088/0957-0233/11/12/703.
154. Azad Mohammed, Avin Abdullah. SCANNING ELECTRON MICROSCOPY (SEM): A REVIEW. Proceedings of **2018** International Conference on Hydraulics and Pneumatics –HERVEX. Romania, ISSN 1454 – 8003.
155. Rudolf M. Tromp. Energy-dispersive X-ray spectroscopy in a low energy electron Microscope. Ultramicroscopy, **2024**, 259. https://doi.org/10.1016/j.ultramic.2024.113935
156. David B. Williams; C. Barry Carter. Transmission Electron Microscopy, A Textbook For Materials Science. Springer Science **2009**, USA. ISBN 978-0-387-76500-6. e-ISBN 978-0-387-76501-3.
157. X-ray diffraction (XRD) basics and application is shared under a CC BY-NC-SA 4.0 license and was authored, remixed, and/or curated by LibreTexts.
158. D8 ADVANCE Introductory User Manual (Preinstallation, Safety, Specifications), DOC-M88-ZXX153 V3 – 11.**2010**. Bruker AXS GmbH, Karlsruhe, Germany. https://xraysrv.wustl.edu/web/xrd/bruker/man/D8_user_v1.pdf